



University  
of Glasgow

McMaster, Steven (2010) *Monolithically integrated mode-locked ring lasers and Mach-Zehnder interferometers in AlGaInAs*. PhD thesis.

<http://theses.gla.ac.uk/1831/>

Copyright and moral rights for this thesis are retained by the Author

A copy can be downloaded for personal non-commercial research or study, without prior permission or charge

This thesis cannot be reproduced or quoted extensively from without first obtaining permission in writing from the Author

The content must not be changed in any way or sold commercially in any format or medium without the formal permission of the Author

When referring to this work, full bibliographic details including the author, title, awarding institution and date of the thesis must be given



University of Glasgow | Faculty of Engineering

# Monolithically Integrated Mode-Locked Ring Lasers and Mach-Zehnder Interferometers in AlGaInAs

by

Steven McMaster

May 2010

A thesis submitted for the  
degree of Doctor of Philosophy (Ph.D.)

in the

Faculty of Engineering

Department of Electronics and Electrical Engineering

UNIVERSITY OF GLASGOW

©Steven McMaster 2010

# *Abstract*

by [Steven McMaster](#)

In this thesis, monolithically integrated photonic devices for next generation optical telecommunications networks were investigated, namely semiconductor mode-locked ring lasers and Mach-Zehnder interferometers operating at 1550 nm. Fabricated on the aluminium quaternary, the 2.3 mm long passively mode-locked ring devices produced 1 ps pulses at a repetition rate of around 36 GHz. It was found that the symmetrically placed dual saturable absorber configuration lead to the largest area of stable mode-locking, agreeing well with theoretical predictions in the literature. Optical harmonic injection mode-locking was found to improve the pulse timing stability, with a reduction in the radio frequency 3 dB linewidth from 1.4 MHz down to 108 kHz, indicating a vast improvement in timing jitter. The sputtered SiO<sub>2</sub> quantum-well intermixing technique allowed for the realisation of both symmetric and asymmetric arm length Mach-Zehnder interferometers, which were demonstrated as an electro-optic switch, tunable wavelength filter and optical code division multiple access encoder/decoder. The work concluded with the monolithic integration of a mode-locked ring laser and asymmetric Mach-Zehnder interferometer to demonstrate a simple, yet effective, photonic integrated circuit.

# Publications

## Journal and Conference Papers

**S.McMaster**, P. Stolarz, G. Mezosi, J. Javaloyes and M. Sorel, “Experimental Comparison between Single and Dual Absorbers in 36 GHz Passively Mode-Locked Semiconductor Ring Lasers,” in preparation for submission to *Photonics Technology Letters, IEEE*, May 2010.

**S.McMaster**, J. Javaloyes and M. Sorel, “Picosecond pulse generation from a 36 GHz passively mode-locked MQW semiconductor ring laser in AlGaInAs,” *European Semiconductor Laser Workshop (ESLW)*, 25–26 September 2009, Vienna, Austria.

J. J. Bregenzer, **S.McMaster**, M. Sorel, B. M. Holmes and D. C. Hutchings, “Compact Polarization Mode Converter Monolithically Integrated Within a Semiconductor Laser,” *Lightwave Technology, Journal of*, vol. 27, no. 14, pp. 2732–2736, 15 July 2009.

**S.McMaster**, J. J. Bregenzer, M. Sorel, B. M. Holmes and D. C. Hutchings, “Monolithic integration of a compact passive polarisation converter within a laser diode,” *European Conference on Integrated Optics (ECIO)*, 11–13 June 2008, Eindhoven, The Netherlands.

**S.McMaster** and M. Sorel, “Monolithic Integration of Semiconductor Mode-Locked Ring Lasers and Mach-Zehnder Interferometers for OCDMA (poster),” *ePIXnet Spring School*, 11–17 May 2008, Portoferraio, Elba Island, Italy.

**S.McMaster** and M. Sorel, “Monolithic integration of Mach-Zehnder interferometer based optical devices,” *Engineering Postgraduate Conference*, University of Glasgow, April 2007, Glasgow, UK.

**S.McMaster** and M. Sorel, “Realisation of OCDMA encoding/decoding using InGaAs/InAlGaAs monolithically integrated Mach-Zehnder interferometer devices (poster),” *ePIXnet Winter School*, 13–17 March 2006, Pontresina, Switzerland.

# *Acknowledgements*

Firstly, I offer my profound thanks to my project supervisor, Dr. Marc Sorel, for giving me the opportunity to join his exciting and ever expanding team of Ph.D. students and post-doctoral researchers. His enthusiastic support and never ending encouragement throughout these past few years have been invaluable to the completion of this work, and are truly appreciated. I would also like to thank my second supervisor, Prof. Catrina Bryce, for some helpful discussions and guidance. In addition, I would like to express my immense gratitude to Dr. Olek Kowalski, my mentor and good friend whilst working at Intense Ltd., not least for introducing and recommending me to my supervisor, but for numerous educational discussions and assistance throughout the years. I must also acknowledge all of the technical staff in the James Watt Nanofabrication Centre, as well as in the Rankine building, they do a great job.

On returning to university from industry to undertake this Ph.D., I have been fortunate enough to make many new colleagues and friends, both in the Opto-electronics Research Group and the department as a whole. At the beginning of my project, Sandor really took me under his wing and introduced me to life as a Ph.D. student and the workings of the fabulous new nanofabrication centre. Soon we formed a good partnership and began to fabricate some really nice chips, as well as enjoying a pint or two. Not long after, I also met Michael, Jenny, Barry, Corrie, Francesca, Cheng, Thomas, Josef and Marco Gnan, who were always willing to offer some advice and encouragement, as well as generally just being nice people to be around. Around one year into my Ph.D., Antonio arrived as a new office mate and showed me some photos of his father's beautiful yacht, "Very nice," I thought, "we will get on well!". I would like thank him for making me laugh with his attempts to learn Glaswegian and letting me into The Shed on numerous occasions. Throughout the years more Italian friends arrived, Guiseppe, Oberdan, Carla, Marco Zanola and Vincenzo. Between all of them, they really got me into some nice Italian ways, such as drinking espresso, enjoying red wine and appreciating fine Italian cuisine. I must also give a mention to my office mate, Leo, who although not a member of the opto group, was adopted by us to great effect. Other guys I would like to acknowledge are Chidi, Jason, Balazs, Masoud, Bruno, Usman, Kamil, Salah, Lianping, Rafal and also Moss, who collaborated on some of this work with me, I wish you guys all the best in your careers. Some French influence was also to be had in the shape of Pierre, Phillippe and Julien, it was

a pleasure meeting you guys. And thanks Julien for your helpful discussions on the theory and analysis of mode-locked lasers. A special acknowledgement goes to another office mate, colleague and friend who's help and support since joining the group was pivotal in the completion of my research, Gabor, cheers pal! To Piotr also, many thanks and appreciation for all of your great help in measuring mode-locked lasers and just being a good mate. We have made the Friday afternoon pizza an institution!!

I would like to express my deep appreciation for all of my excellent family, so many wonderful aunties, uncles and cousins who form such a supporting, loving and close knit unit. Also, to all of my mates, cheers for just being there and allowing me to take my mind off this work when I needed it most. A very special mention must be afforded to my sister, Karen, for her endless love and support, not only throughout this work but from as far back as I can remember. She really is the best sister you could ask for! Finally, from the bottom of my heart, I thank my mum, Anne, for absolutely everything. She has selflessly supported me in so many ways on this amazing journey in life. Quite literally, I could not have done any of it without her.

# Contents

<b>Abstract</b>	<b>i</b>
<b>Publications</b>	<b>iii</b>
<b>Acknowledgements</b>	<b>iv</b>
<b>Acronyms</b>	<b>xi</b>
<b>1 Introduction</b>	<b>1</b>
1.1 Optical Telecommunications	1
1.1.1 The Beginnings	1
1.1.2 Rise of the Internet	2
1.1.3 The Role of Fibre Optics	2
1.1.4 Optical Networks	3
1.1.5 Multiple Access Communication: Increasing the Bandwidth	3
1.1.5.1 Optical Time Division Multiplexing	4
1.1.5.2 Wavelength Division Multiplexing	4
1.1.5.3 Optical Code Division Multiple Access	5
1.2 Optical Network Components	5
1.2.1 Light Sources	6
1.2.2 Waveguides and Couplers	8
1.2.3 Photonic Integrated Circuits	8
1.3 Motivation and Aims of This Research	9
<b>2 Material and Device Design Considerations</b>	<b>10</b>
2.1 Introduction	10
2.2 AlGaInAs Multiple Quantum-Well Material System	11
2.3 Electro-Optic Properties	14
2.3.1 Quantum Confined Stark Effect	15
2.3.2 Carrier Induced Electro-Optic Effects	15
2.3.2.1 Band Filling	15
2.3.2.2 Band-Gap Shrinkage	16
2.3.2.3 Free Carrier Absorption	16

2.3.2.4	Collective Carrier Induced Effects . . . . .	16
2.3.3	Comparison of Quantum Confined Stark Effect and Carrier Induced Electro-Optic Effects . . . . .	17
2.3.4	Chirp Parameter . . . . .	17
2.4	Constitutional Component Design . . . . .	19
2.4.1	Waveguide Design . . . . .	19
2.4.2	Curved Waveguide Design: Assessment of Bending Losses . . . . .	22
2.4.3	Multi-Mode Interference Coupler Design . . . . .	22
2.5	Mach-Zehnder Interferometer Design . . . . .	30
2.5.1	OTDM: MZI Operation Principle as an OTDM demultiplexer . . . . .	37
2.6	Asymmetric Mach-Zehnder Interferometer Design . . . . .	39
2.6.1	DWDM: AMZI Operation Principle as a Wavelength Demultiplexer . . . . .	39
2.6.2	OCDMA: AMZI Operation Principle as an OCDMA encoder/decoder . . . . .	42
2.7	Semiconductor Mode-Locked Lasers . . . . .	46
2.7.1	Mode-Locking Theory . . . . .	46
2.7.2	Mode-Locking Methods . . . . .	48
2.7.2.1	Active Mode-Locking . . . . .	48
2.7.2.2	Passive Mode-Locking . . . . .	49
2.7.2.3	Hybrid Mode-Locking . . . . .	52
2.7.3	Pulse Duration and Spectral Width . . . . .	52
2.7.4	Semiconductor Ring Lasers . . . . .	54
2.7.4.1	Evanescent Field Couplers . . . . .	55
2.7.4.2	Mode-Locking in Semiconductor Ring Lasers . . . . .	58
2.8	Integrated Devices . . . . .	60
2.8.1	Monolithically Integrated OCDMA Transmitter . . . . .	60
2.9	Chapter Summary . . . . .	61
<b>3</b>	<b>Fabrication Technology and Material Characterisation</b> . . . . .	<b>63</b>
3.1	Introduction . . . . .	63
3.2	Active/Passive Integration . . . . .	64
3.2.1	Quantum-Well Intermixing . . . . .	65
3.2.1.1	Impurity Induced Vacancy Disordering . . . . .	65
3.2.1.2	Photo Absorption Induced Disordering . . . . .	66
3.2.1.3	Sputtering Induced Vacancy Disordering . . . . .	66
3.2.1.4	Selected Intermixing in Selected Areas . . . . .	69
3.3	Patterning using Electron Beam Lithography . . . . .	71
3.3.1	Electron Beam Lithography Resists . . . . .	72
3.4	Reactive Ion Etching . . . . .	73
3.4.1	The Effects of RIE Lag . . . . .	75
3.5	Ohmic Contacts . . . . .	77
3.5.1	Metallisation . . . . .	78

3.5.2	p-type Ohmic Contact Performance Analysis Using the Transfer Length Method . . . . .	79
3.6	Waveguide Loss Measurements . . . . .	80
3.7	Broad Area Laser Results . . . . .	83
3.8	Ridge Waveguide Laser Results . . . . .	85
3.9	Intermixed Ridge Waveguide Laser Results . . . . .	86
3.10	Experimental Characterisation of Electro-Optic Effects . . . . .	89
3.10.1	Impact of SISA on Electro-Optic Effects . . . . .	94
3.11	Relaxation Oscillation Frequency Measurements . . . . .	98
3.12	Antireflection Coatings . . . . .	100
3.12.1	Single-layer Coatings . . . . .	100
3.12.2	Multi-layer Coatings . . . . .	101
3.12.3	TiO <sub>2</sub> and SiO <sub>2</sub> Double-layer Coating Design . . . . .	102
3.12.4	Thin Film Deposition Methods and Process Development . . . . .	103
3.12.4.1	Basics of Sputter Deposition . . . . .	103
3.12.4.2	Sputter Deposition Process Development . . . . .	104
3.12.5	Coating Performance . . . . .	106
3.13	Chapter Summary . . . . .	108
<b>4</b>	<b>Mode-Locked Ring Laser Results</b>	<b>110</b>
4.1	Introduction . . . . .	110
4.2	Evanescent Field Coupler Measurements . . . . .	110
4.3	Ring Laser Results . . . . .	111
4.3.1	Optical Power . . . . .	112
4.3.2	RF Spectra . . . . .	114
4.3.3	Optical Spectra . . . . .	119
4.3.4	Autocorrelation . . . . .	121
4.3.5	Optical Harmonic Injection Mode-locking . . . . .	124
4.4	Chapter Summary . . . . .	127
<b>5</b>	<b>Mach-Zehnder Interferometer Results</b>	<b>129</b>
5.1	Introduction . . . . .	129
5.2	Multi-Mode Interference Coupler . . . . .	129
5.3	Symmetric Mach-Zehnder Interferometer . . . . .	130
5.3.1	Switching Measurements . . . . .	131
5.4	Asymmetric Mach-Zehnder Interferometer . . . . .	132
5.4.1	AMZI:DWDM . . . . .	133
5.4.2	AMZI:OCDMA . . . . .	134
5.5	Device Integration . . . . .	136
5.5.1	Integrated Mode-Locked SRL and AMZI . . . . .	136
5.6	Chapter Summary . . . . .	138
<b>6</b>	<b>Conclusions and Future Work</b>	<b>140</b>
6.1	Conclusions . . . . .	140
6.1.1	Chapter 1: Introduction . . . . .	140

---

6.1.2	Chapter 2: Material and Device Design Considerations . . .	141
6.1.3	Chapter 3: Fabrication Technology and Material Character- isation . . . . .	141
6.1.4	Chapter 4: Mode-Locked Ring Laser Results . . . . .	142
6.1.5	Chapter 5: Mach-Zehnder Interferometer Results . . . . .	142
6.2	Future Work . . . . .	143

**Bibliography****145**

*To my family.*

# Acronyms

<b>AlGaInAs</b> Aluminium Gallium Indium Arsenide	<b>EM</b> electromagnetic
<b>AMZI</b> asymmetric Mach-Zehnder interferometer	<b>ER</b> extinction ratio
<b>AR</b> antireflection	<b>FP</b> Fabry-Perot
<b>BAL</b> broad area laser	<b>FSR</b> free spectral range
<b>BPM</b> beam propagation method	<b>FWHM</b> full width half maximum
<b>CS-RZ</b> carrier suppressed return to zero	<b>GaAs</b> Gallium Arsenide
<b>CPM</b> colliding pulse mode-locking	<b>GaInAsP</b> Gallium Indium Arsenic Phosphide
<b>CW</b> clockwise	<b>GRINSCH</b> graded index separate confinement heterostructure
<b>CCW</b> counter clockwise	<b>GVD</b> group velocity dispersion
<b>DBR</b> distributed Bragg reflector	<b>hh</b> heavy-hole
<b>DC</b> direct current	<b>HSQ</b> Hydrogen silsesquioxane
<b>DFB</b> distributed feedback	<b>ICP</b> inductively coupled plasma
<b>DWDM</b> dense wavelength division multiplexing	<b>InP</b> Indium Phosphide
<b>e-beam</b> electron-beam	<b>ITU</b> International Telecommunication Union
<b>EBL</b> electron-beam lithography	<b>IPA</b> isopropyl alcohol
<b>EDFA</b> Erbium doped fibre amplifier	<b>lh</b> light-hole
	<b>MFC</b> mass flow controller

<b>MIBK</b> methyl isobutyl ketone	<b>RTA</b> rapid thermal annealer
<b>MMI</b> Multi-mode interference	<b>RWGL</b> Ridge waveguide laser
<b>MOCVD</b> metal organic chemical vapour deposition	<b>SA</b> saturable absorber
<b>MQW</b> multiple quantum-well	<b>SAG</b> selective area growth
<b>MZI</b> Mach-Zehnder interferometer	<b>SDH</b> synchronous digital hierarchy
<b>NOLM</b> non-linear optical loop mirror	<b>SEM</b> scanning electron microscope
<b>NRZ</b> non-return to zero	<b>SESAM</b> semiconductor saturable absorber mirror
<b>OCDMA</b> optical code division multiple access	<b>SHG</b> second harmonic generation
<b>OEO</b> optical-electrical-optical	<b>SISA</b> selected intermixing in selected areas
<b>OSA</b> optical spectrum analyser	<b>SMSR</b> side mode suppression ratio
<b>OTDM</b> optical time division multiplexing	<b>SOA</b> semiconductor optical amplifier
<b>PAID</b> photo absorption induced disordering	<b>SONET</b> synchronous optical network
<b>PECVD</b> plasma enhanced chemical vapor deposition	<b>SPM</b> self phase modulation
<b>PIC</b> photonic integrated circuit	<b>SRL</b> semiconductor ring laser
<b>PMMA</b> polymethyl methacrylate	<b>TBP</b> time bandwidth product
<b>PL</b> photoluminescence spectroscopy	<b>TE</b> transverse electric
<b>PVD</b> physical vapour deposition	<b>TEC</b> thermoelectric controller
<b>QCSE</b> quantum confined stark effect	<b>TLM</b> transfer length method
<b>QW</b> quantum-well	<b>TM</b> transverse magnetic
<b>QWI</b> quantum-well intermixing	<b>TOAD</b> terahertz optical asymmetric demultiplexer
<b>RF</b> radio frequency	<b>TPC</b> temporal phase coded
<b>RIE</b> reactive ion etching	<b>WDM</b> wavelength division multiplexing
	<b>XPM</b> cross phase modulation

# Chapter 1

## Introduction

### 1.1 Optical Telecommunications

#### 1.1.1 The Beginnings

Telecommunication can generally be regarded as the study and application of transmitting information from one point to another through some data carrying medium. The actual literal origins of the word date back to the French expression *télécommunication*, which is a compound of the Greek prefix *tele* meaning “distant” and the Latin phrase *communicare* denoting “to share”.

The techniques and media used to convey such exchanges of knowledge have evolved throughout the years from the use of mere smoke signals and drums, to telegrams and analogue radio signals. However, in modern communications systems, the data is transmitted in the digital form, meaning that even if the source of the message produces analogue signals, for example from a microphone, the information has to be converted into the digital domain prior to transfer. The main reason for this is basically to reduce any unwanted noise in the system [1]. Various types of digital communication channels currently exist including copper wires, free space, coaxial cable, and of course, optical fibre. These media are essentially the carriers of electromagnetic (EM) waves that have had the useful information superimposed onto them prior to transmission [2, 3].

### 1.1.2 Rise of the Internet

Recently we have witnessed the exploding rise of the Internet that has allowed individuals across the world to access and contribute masses of information at the mere touch of a button. One of the main enabling technologies, pivotal in the staggering success of the so called *world wide web*, has been the deployment of practical optical telecommunications links. Such links, as represented schematically in their simplest form in Fig. 1.1, consist of a transmitter, a receiver and a data carrying optical fibre. The transmitter is used to encode the useful data onto some form of optical carrier signal that will traverse the channel with minimal distortion. At the receiving end, the signal is then detected with the required information being extracted for purposeful use.

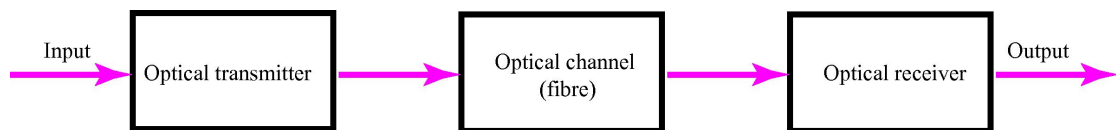


FIGURE 1.1: A generic optical fibre communications system.

### 1.1.3 The Role of Fibre Optics

Early attempts at instituting useful optical transmission systems were suppressed due to the lack of suitable coherent light sources and of a useable guiding medium. However, the discovery of the semiconductor light emitting [4] and laser diodes [5, 6], coupled with the further development of optical fibre [7], reinforced previous experimentation that fibre optic technology was a serious contender for transmitting large amounts of data effectively.

In addition to a remarkably greater information carrying capacity (potentially up to several Tbit/s), modern optical fibre offers many other advantages over its contemporaries, such as a low power attenuation factor, an immunity to electrical interference, decreased bit error rates and a reduction in crosstalk. These benefits have lead to the propulsion of the technology to its present position in fulfilling, or at least attempting to fulfil, the relentless requirement for increasing network bandwidth in core and metro networks, fuelled mainly by the aforementioned growth of the modern telecommunications age.

### 1.1.4 Optical Networks

When discussing optical networks, we tend to focus on several generations of network architectures. The first generation of systems used optical fibres merely as the communications channel with electronics still performing all of the switching and system functions, i.e. the fibres were effectively grafted onto the existing infrastructure. For example, the synchronous optical network (SONET) and synchronous digital hierarchy (SDH) protocols use optical fibre purely as their underlying transmission mechanisms. Nearly all of the value added service functionality is implemented using electronic integrated circuits and system software [8]. These networks are currently used today: SONET in North America and SDH in the rest of the world [9]. However, as the state of the art in fibre communications components and systems advanced, it became clear that second generation networks might benefit in ways that transcended the initial role of optics in data transport. For example, by using optics rather than electronics to perform some of the intelligent system functions such as switching, amplification and routing, bottlenecks inherent from the data rate limitations, and the high costs due to the incurred optical-electrical-optical (OEO) conversions of non-optical components could be eliminated or drastically reduced. In addition to providing enormous capacities in the network, an optical architecture also provides a common infrastructure over which a variety of services may be delivered. Such optical networks are also increasingly becoming capable of delivering bandwidth where and when needed. These factors and others have lead to the vision of a future digital all optical transport network capable of some 40 Gbit/s bit data rates and beyond [8].

### 1.1.5 Multiple Access Communication: Increasing the Bandwidth

Various techniques have been, and are currently being, developed to further exploit the available transmission capacity of current optical links. This is beneficial as it is generally regarded to be more economically viable relaying data at higher bit rates over single fibres than at lower rates over several fibres [2, 3]. These methodologies have proved valuable in electronic data networks and are collectively known as multiple access techniques.

### 1.1.5.1 Optical Time Division Multiplexing

One such approach interleaves several data streams at the same wavelength in the time domain such that each bit is assigned a discrete time slot, therefore a higher bit rate optical signal is possible, as shown in Fig. 1.2. This scheme is known as optical time division multiplexing (OTDM) [10]. The latest data rates achievable in laboratory demonstrated OTDM systems are of the order of 640 Gbit/s, based on four wave mixing in a polarisation maintaining fibre loop [11], although full commercial implementation of OTDM is still several years away.

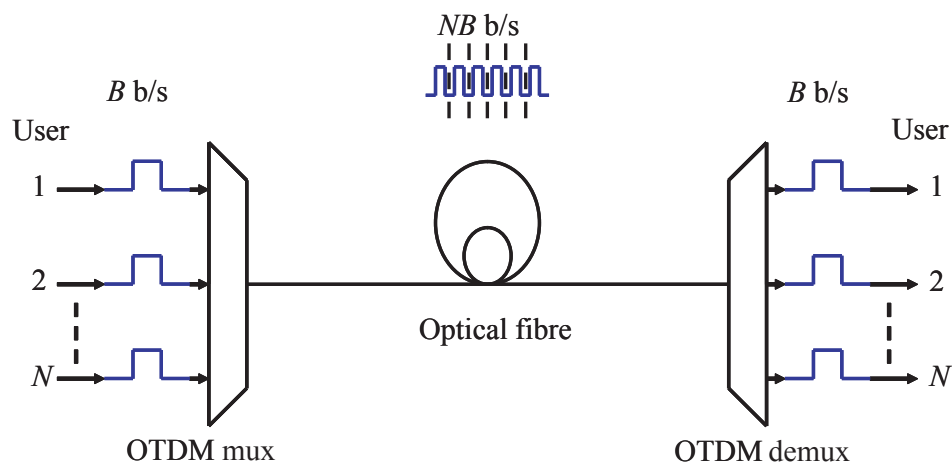


FIGURE 1.2: A simple OTDM network where all signals are in the same wavelength band, but assigned their own discrete time slots.

### 1.1.5.2 Wavelength Division Multiplexing

Another method is based on the idea of simultaneously transmitting signals at different wavelengths (or optical frequencies) of light such that they do not interfere with one and other, hence higher data rates are achievable. Fig. 1.3 shows such a system, known as wavelength division multiplexing (WDM), which was first proposed in 1970 by DeLange [12]. Flexible optical networking for wide area networks, metropolitan area networks, and in some cases, local area and access networks are predominantly based on WDM or dense wavelength division multiplexing (DWDM) systems [1, 13]. Recent advances include the new field trial record of 3040 km reach with sixty eight 10 Gbit/s channels and two 40 Gbit/s channels transmitted using a wide reach DWDM platform [14].

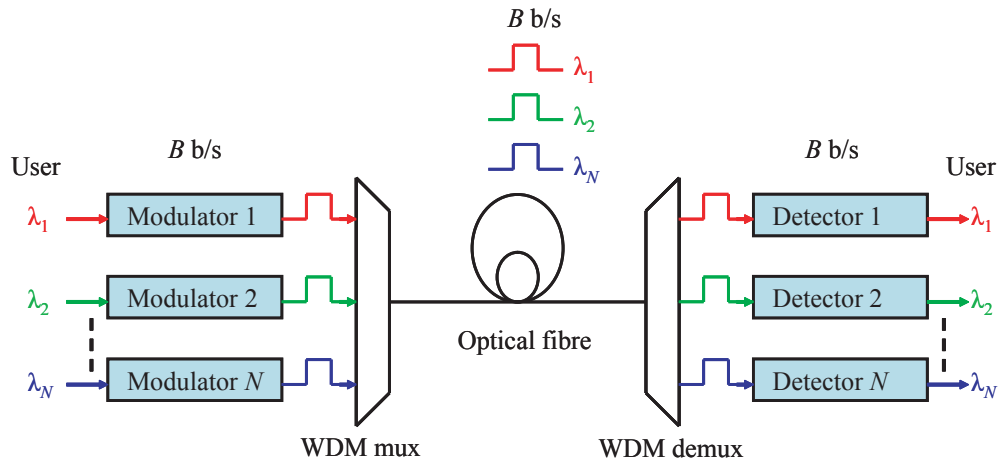


FIGURE 1.3: A simple WDM network where several wavelengths are transmitted down the fibre simultaneously in order to increase the capacity.

### 1.1.5.3 Optical Code Division Multiple Access

An alternative to both of the above schemes is based on the successful spread spectrum techniques, as used in satellite and radio communications, and is realised by the use of unique coding to permit multiple users access in the same time and wavelength domain [15, 16]. This method is termed optical code division multiple access (OCDMA) and has been the focus of great interest recently [17, 18]. It offers various advantages over OTDM and DWDM such as more efficient use of the channel by virtue of asynchronous access, and an increased resistance to jamming and detection. It is envisaged that the benefits of OCDMA coupled with the current network infrastructures could pave the way to the aforementioned digital all optical network [19]. Fig. 1.4 shows such a scheme where each channel is optically encoded with a specific code word in the same wavelength and time domain, transmitted and then subsequently decoded using matched filtering.

## 1.2 Optical Network Components

The vision of an all optical telecommunications network has placed stringent demands on next generation elements, such as wavelength tunable lasers, reconfigurable add/drop multiplexers, high port count (de)multiplexer devices, broadband amplifiers, gain/dispersion equalisers and components for network management [13]. More and more effort is being applied to the research of planar light wave

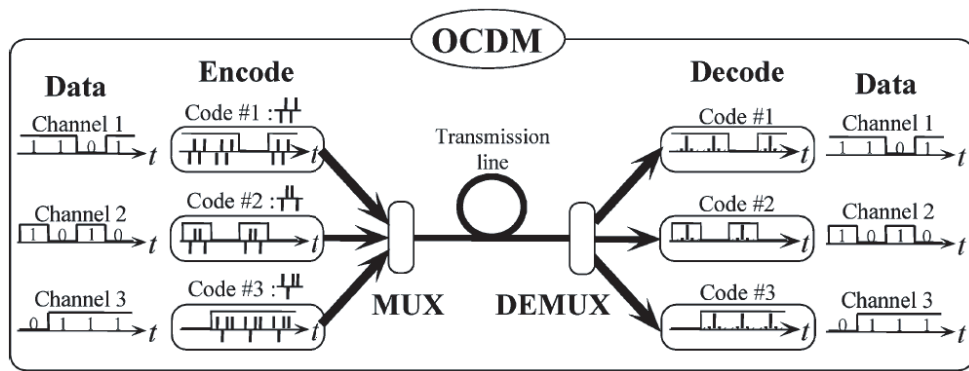


FIGURE 1.4: Optical code division multiple access system [20].

circuits in which semiconductor based components are monolithically integrated on a single chip to fulfil such functions. In the following sections such semiconductor based componentry pertinent to this body of work are briefly discussed, with a more detailed analysis being left to subsequent chapters.

### 1.2.1 Light Sources

Most modern light sources used for high speed optical telecommunication tend to be semiconductor laser diodes due to their unique properties such as small size, low cost, high efficiency, direct pumping ability and wavelength stability [21]. Semiconductor lasers may emit light over a large range of wavelengths from near ultraviolet to the far infra-red ( $0.5\text{-}10\ \mu\text{m}$ ) by engineering the band-gap structure of the compound semiconductor material used, as shown in the growth chart in Fig. 1.5, which details the wavelength versus lattice constant for some common III-V binary compounds used in photonics. The first laser diodes were crude p-n junctions based on Gallium Arsenide (**GaAs**), emitting at a wavelength of around 850 nm (corresponding to the low loss transmission window of early silica multi-mode fibres). These devices allowed for data rates of up to 45 Mbit/s with a repeater spacing of 10 km [2]. However, they were not very efficient and it was also found that fibres actually exhibited lower attenuation and dispersion characteristics at around 1300 nm, and later, 1550 nm. For these reasons, and the fact that excellent amplifiers (Erbium doped fibre amplifier (**EDFA**)) were also developed at 1550 nm, meant that new lasers were engineered at these wavelengths using improved carrier and photon confining geometries called heterostructures, and later double heterostructures, in Gallium Indium Arsenic Phosphide (**GaInAsP**) [22].

This material system was used as it can be grown lattice matched to an Indium Phosphide (InP) substrate with the epitaxial layers being able to emit light at 1300 nm and 1550 nm. Subsequent developments lead to the creation of quantum-well (QW) lasers where carriers are further confined by virtue of a thin layer or layers of narrow band-gap material (high refractive index) in the dimension perpendicular to the layer surface. QW lasers allow for a vast reduction (from 100s of mA down to 10s of mA) in the current required to achieve lasing, and shall be discussed in more detail in the following chapter.

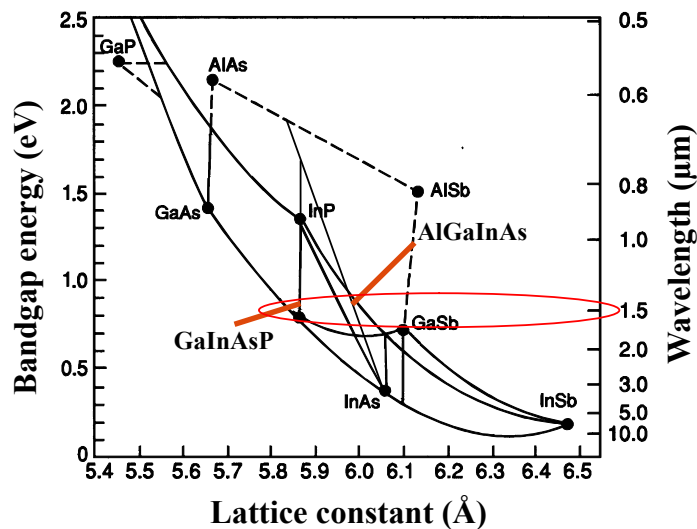


FIGURE 1.5: Band-gap energy versus lattice constant for various III-V semiconductors. Shown in red are the points where two common compounds used in photonics for telecomms, GaInAsP and AlGaInAs, coincide with an emission wavelength of 1550 nm.

Various types of laser diode exist including distributed feedback (DFB) [23], distributed Bragg reflector (DBR) [24] and tunable lasers [25]. In this work, an interesting geometry of laser diode is investigated, the semiconductor ring laser (SRL). Such devices are highly attractive due to their cavity structure that can be lithographically defined without recourse to cleaved facet mirrors, ideal for monolithic integration. Also, as with conventional Fabry-Perot (FP) lasers, they may be configured in such a way that mode-locking or rather, phase-locking, of the cavity modes is possible, making them suitable candidates for ultrashort pulse sources for deployment in optical communications systems [26]. When mode-locked, ring lasers also have the natural advantage that two counter propagating pulses may be expected to collide within the mode-locking element such that colliding pulse mode-locking (CPM) takes place. The advantages of CPM shall be discussed in detail in subsequent sections of this thesis.

## 1.2.2 Waveguides and Couplers

Waveguides are vital elements in any optical system, as they are used to route the light signals from one desired point to another. Waveguides rely upon the interaction of light (governed by Maxwell's EM equations) with the guiding medium in order to confine the guided modes as required [27]. Various types of semiconductor structure are available for optical wave guiding, for example the slab waveguide, in which a layer of higher refractive index material is sandwiched between two layers of lower index material, with the light being confined due to total internal reflection (admittedly an over simplification, but may be explained in greater detail in any optical textbook). Another guiding structure is the 2-D waveguide geometry where there is not only vertical confinement, as in the slab structure, but also horizontal confinement due to refractive index changes in the lateral direction.

Couplers are also critical circuit elements as they are required for combining and splitting light signals in a network or on a chip. In terms of this work, couplers are used extensively in the realisation of mode-locked ring lasers for extracting light from the circular cavity, and in the Mach-Zehnder interferometer (MZI)s for the splitting and recombining of the light signals.

## 1.2.3 Photonic Integrated Circuits

Most functional devices deployed in optical telecomms systems today are of a discrete nature. The benefit here is that each device may be designed and optimised to perform its sole function to almost perfection. However, complexities arise when packaging these components and subsequently coupling light into and out of each chip. Heavy optical losses are obtained as a result of these numerous couplings and individual packaging costs tend to account for the majority of the overall component price. By reducing the amount of fibre couplings between components, the number of potential failure points also decreases, therefore reliability increases. The associated high cost of such OEO conversions is also reduced [28].

Monolithic integration in such circuits alleviates these issues by allowing a chip with many functions to be manufactured in a single package, hence reducing the number of chip to chip coupling interactions. InP is an attractive integration platform, as it allows both active (e.g. lasers, detectors, modulators) and passive (e.g. couplers, low loss waveguides, gratings) devices operating at 1300 nm and

1550 nm to be realised on a single substrate, thus enabling all the key high value optoelectronic functions required in an optical transport network [29]. Indeed Infinera Corporation, a large scale photonic integrated circuit (PIC) manufacturer, have already produced InP based 100 Gbit/s multi channel transmitter/receiver DWDM chips for commercial deployment [30]. Such large scale PICs represent a significant technology innovation that simplifies optical system design, decreases chip footprint, power consumption and cost, and also improves reliability. An optical image and schematic of such a transmitter chip are shown in Fig. 1.6, where the chip footprint measures around 22 mm<sup>2</sup> only.

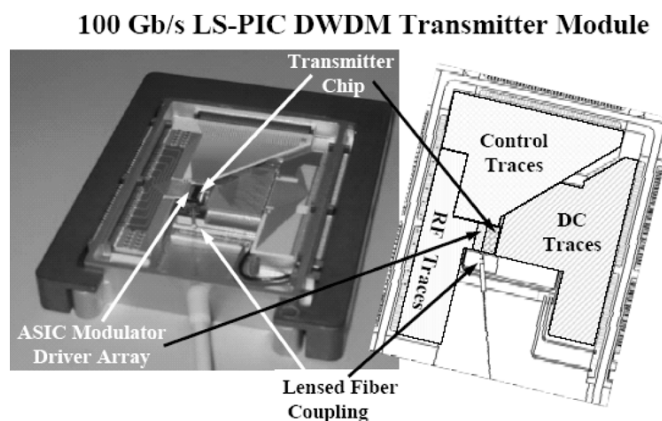


FIGURE 1.6: Optical image and schematic of Infinera’s 100 Gbit/s multi channel transmitter module [30].

### 1.3 Motivation and Aims of This Research

Ultimately, the motivation behind this research lies in the fact that the ever demanding need for network capacity needs to be addressed. Monolithic integration of photonic devices is a highly potential and advantageous solution to this issue. This work brings together several of our groups research strengths, i.e. expertise in semiconductor ring lasers, world class fabrication facilities and a proprietary active/passive integration platform, in order to successfully integrate mode-locked SRLs and MZIs to realise highly functional monolithically integrated photonic circuits for deployment in future optical communications systems.

# Chapter 2

## Material and Device Design Considerations

### 2.1 Introduction

This chapter begins by introducing some of the basic background theory and design considerations relevant to the devices in this research work. Firstly, the Aluminium Gallium Indium Arsenide ([AlGaInAs](#)) material structure is presented, discussing its associated electro-refractive properties, which are vital in the design of electro-optic based photonic components. Both effects based on applied electric field and carrier injection will be considered with a figure of merit being defined, allowing for the optimal design of such devices.

Some general theory on the geometrical structures to be employed in the devices is then presented, with the use of simulation tools to verify and optimise the designs prior to fabrication and testing. Multi-mode interference ([MMI](#)) couplers are discussed in the context of their use in the realisation of MZIs, whose operating principles are then detailed also with specific relevance to optical telecommunications applications.

Mode-locking is introduced as a narrow pulse generation method, with some simple theory and techniques applicable to semiconductor lasers being presented. An alternative geometry of laser is then discussed, the SRL, with its associated advantages over linear cavity devices being reported. Some integrated device designs are then detailed with reference to their relevance in high speed optical networks.

## 2.2 AlGaInAs Multiple Quantum-Well Material System

A QW consists of a thin layer (comparable to the de Broglie wavelength) of semiconductor material embedded between two layers of wider band-gap material, wherein quantum effects transpire. As a result of this quantisation, the energy dependence of the density of states, i.e. the number of quantum states per unit energy per unit volume, is step-like in behaviour, as shown in Fig. 2.1 for a GaInAs well with AlGaInAs barriers [31]. The diagram illustrates (a) a QW energy band-gap structure with the quantised energy levels, and (b) the corresponding density of states for both bulk (dashed) and QW (solid) material [32].

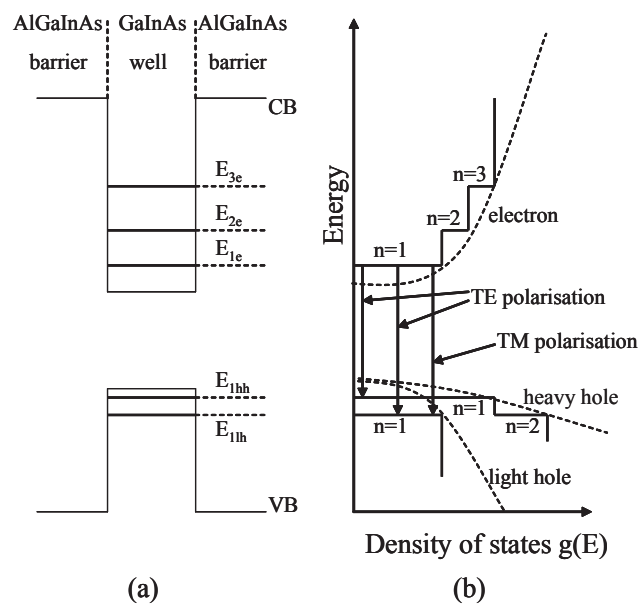


FIGURE 2.1: (a) Energy band structure for the conduction and valence bands in QW material showing the quantised energy levels, and (b) the corresponding density of states for both bulk (dashed) and QW (solid) material. For QWs the density of states is constant at each quantised energy level.

A QW laser diode device allows for photon generation through transitions between confined states in the conduction and valence bands, thus lasing occurs at wavelengths determined by the band-gap of the material and the quantised energy levels. On closer inspection of the density of states, it is observed that for QWs, the lowest energy level in the conduction band and the highest energy level in the valence band have a finite and substantial density of states, whereas for bulk material the value is zero at minimum energy. This implies that in bulk lasers the gain must build up from carriers filling up the low density of states levels

before it can reach high gain levels, and the carriers at energies below that high gain level are ineffective in contributing towards gain [32]. In contrast, carriers in QW lasers contribute to gain at its peak as the maximum gain always occurs at an energy equal to the lowest interband transition energy. This is significant in terms of the laser's operating characteristics. Firstly, the reduced density of states requires fewer electrons to reach optical transparency, leading to a lower threshold current density. Secondly, the differential gain is much larger giving rise to the capability of high speed operation and a narrow output linewidth [33]. The price paid however is that the gain may saturate at a certain value when the electron and hole states of a given discrete energy level are fully inverted, whereas the gain in bulk lasers rarely saturates due to the filling of an ever increasing density of states [34]. Nevertheless, the issue of gain saturation in QW lasers may be overcome by the use of multiple quantum-well (MQW)s. Obviously this leads to larger transparency current densities, but allows for improved differential gain and higher gain saturation [35].

Conventional lattice matched (i.e. unstrained) III-V semiconductor QW edge emitting lasers based on interband transitions predominantly emit transverse electric (TE) polarised light. Here the convention that TE refers to light polarised in the plane of the QWs and transverse magnetic (TM) to light polarised perpendicular to the plane of the QWs is used. This polarisation dependence of the optical gain originates primarily from the symmetry of the uppermost, heavy-hole (hh), valence band in the QWs (Fig. 2.1) [34]. A TE polarised optical wave may couple with both electron to hh transitions and electron to light-hole (lh) transitions due to the quantum mechanical selection rules. However, a TM polarised wave may only couple with electron to lh transitions, where the density of states is less than in the hh case. Furthermore, the larger TE polarised mode overlap with the optical gain distribution in the waveguide core due to the cross sectional geometry, and the higher TE polarised mode reflectivity of the cleaved facets [36], normally yields an overall lower threshold current for TE polarised modes than for TM modes. However, by inducing biaxial strain in the structure, one may alter the polarisation properties as a result of increasing the degeneracy between the lh and hh subbands. Compressive strain serves to increase the splitting, reducing the effective hole mass (greater TE gain), whereas tensile strain decreases the splitting, having the opposite effect on the effective hole mass (greater TM gain) [31]. Compressive strain in QW lasers leads to lower transparency levels and a higher differential

gain [34]. Such polarisation dependence is also important for many other photonic applications, for example, in polarisation insensitive semiconductor amplifiers [37].

Direct band-gap QW structures for telecommunications devices operating in the conventional or C-band wavelength range (1530-1565 nm), tend to be based on the GaInAsP material system, usually termed the phosphorus quaternary [22]. This is mainly due to the maturity of the growth techniques used for producing such materials and also the availability of advanced chip processing. However, the temperature dependence of lasers fabricated using GaInAsP is an issue that restricts their thermal performance, arising due to reduced electron confinement and, to a lesser extent, Auger losses [38]. The so called aluminium quaternary, AlGaInAs, has been the focus of much interest recently mainly due to its attractive band discontinuity properties, for example, a large conduction band offset, ( $\Delta E_c = 0.72\Delta E_g$ ), compared to that of the phosphorus system, ( $\Delta E_c = 0.40\Delta E_g$ ), leading to improved electron confinement (see Fig. 2.2). This property give rise to advantages such as a lower threshold current density and higher differential gain [39].

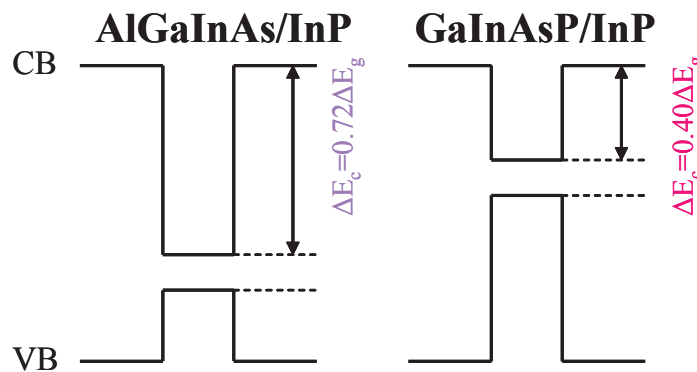


FIGURE 2.2: Comparison of the band discontinuities between the AlGaInAs and GaInAsP material systems.

The QW material used for the devices in this work is a commercially available 1550 nm *p-i-n* laser diode wafer structure grown by metal organic chemical vapour deposition (MOCVD), consisting of five compressively strained (12000 ppm) 6 nm thick  $\text{Al}_{0.07}\text{Ga}_{0.22}\text{In}_{0.71}\text{As}$  wells with six tensile strained (-3000 ppm) 10 nm thick  $\text{Al}_{0.224}\text{Ga}_{0.286}\text{In}_{0.49}\text{As}$  barriers. The QWs and barriers are situated between two 60 nm AlGaInAs graded index separate confinement heterostructure (GRINSCH) layers. The GRINSCH section is included to generate a much smaller carrier population in the optical core layer at threshold, as compared to standard SCH

structures, thus lowering the threshold current density and increasing the differential gain [40]. An 800 nm InP lower cladding, 1720 nm InP upper cladding and a 200 nm highly doped ( $1.5 \times 10^{19} \text{cm}^{-3}$ ) GaInAs contact layer complete the structure. All layers (except the wells and barriers) are lattice matched to a n-doped InP substrate with Zn and Si used as the p-type and n-type dopants respectively. The conduction band diagram for the epitaxial layers is shown for reference in Fig. 2.3.

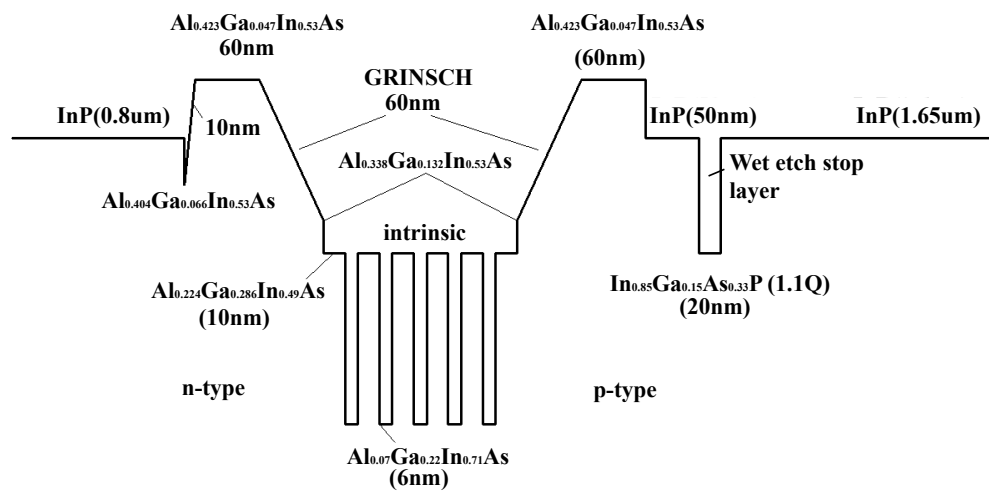


FIGURE 2.3: Energy band diagram for the conduction band of the layers in the AlGaInAs structure. Note the omission of the highly doped p-type contact layer as it is far enough away from the core it plays no part in the optical confinement.

## 2.3 Electro-Optic Properties

An important property of semiconductor materials applicable in photonics is the electro-optic effect. This phenomenon is essential for the functionality of many integrated optical devices. For the AlGaInAs QW material system, or indeed the phosphorus quaternary, there are two distinct types of electro-optic effect, namely that of an applied electric field [41], and that of current injection [42]. As the MZI devices in this work utilise electro-optic phase modulating sections, it is important to consider these effects.

### 2.3.1 Quantum Confined Stark Effect

When an electric field is applied across a QW via a reverse bias voltage, there is an associated tilting of the conduction and valence bands leading to a shift in the absorption band edge to higher wavelengths. This phenomenon is known as the quantum confined stark effect (QCSE) and is commonly used in high speed integrated optics [43]. For example, high speed QW electro-absorption modulators rely on the QCSE in order to modulate the optical signal via electrical control [44, 45]. It is also known, through the Kramers-Kronig relations, that a change in absorption also leads to a change in the refractive index of the material [43, 46].

### 2.3.2 Carrier Induced Electro-Optic Effects

By changing the carrier concentration in QW structures, interactions between the carriers leads to a change in the absorption band edge of the material [47]. As noted previously, this will also result in a refractive index change. There are three main contributing factors in electro-optic effects based on current injection: band filling, band-gap shrinkage and free carrier absorption. These mechanisms are described briefly in the following sections.

#### 2.3.2.1 Band Filling

Similar to the Burstein-Moss effect, band filling occurs when doping is introduced into the material and manifests itself as a decrease in absorption for photon energies slightly above the nominal band-gap [48]. By doping the semiconductor material, the low states in the conduction band (n-type) or the high states in the valence band (p-type) become sufficiently occupied, resulting in electrons from the valence band requiring energies greater than the nominal band-gap to be optically excited to the conduction band. Since band filling is a result of free carriers, injection can be considered to be equivalent to doping, except that injection will result in band filling effects from both electrons and holes [47]. The carrier induced refractive index change appears to be largest for photon energies near the material band-gap, and decreases then approaches zero for energies far above and below the band-gap.

### 2.3.2.2 Band-Gap Shrinkage

Band-gap shrinkage, or re-normalisation, transpires when injected electrons populate the states at the bottom of the conduction band such that the electron wave functions overlap (if the carrier concentration is sufficient), forming a gas of interacting species. The electrons in this gas repel each other due to the Coulombic forces, resulting in a reduction of the band-gap energy and thus a change in absorption and refractive index [48]. This effect is also valid for holes at the top of the valence band. As in the case of band filling, the largest changes in refractive index are observed near the band-gap wavelength. Unlike band filling, however,  $\Delta n$  is positive for photon energies below the nominal band-gap.

### 2.3.2.3 Free Carrier Absorption

Both the band filling and band-gap shrinkage effects are based upon interband photon absorption by free carriers. However, it is also possible that a free carrier may absorb a photon and move to a higher energy state intraband. This mechanism is known as free carrier absorption or the plasma effect. It has been shown using the Drude model that the refractive index change due to the intraband transitions is proportional to the concentration of carriers and the square of the wavelength [48]. From this model,  $\Delta n$  is always negative supplementing the index change by band filling for energies below the material band-gap.

### 2.3.2.4 Collective Carrier Induced Effects

Until now we have briefly considered the three carrier induced electro-optic effects individually, however, the net effect will be a result of them all. The theoretical combination of all three effects for InP with a high carrier concentration value of  $N=P=3 \times 10^{18} \text{cm}^{-3}$ , is illustrated in Fig. 2.4. From this plot it is evident that for efficient electro-optic devices, i.e. maximum changes in index, one should operate at a wavelength close the band-gap wavelength of the material.

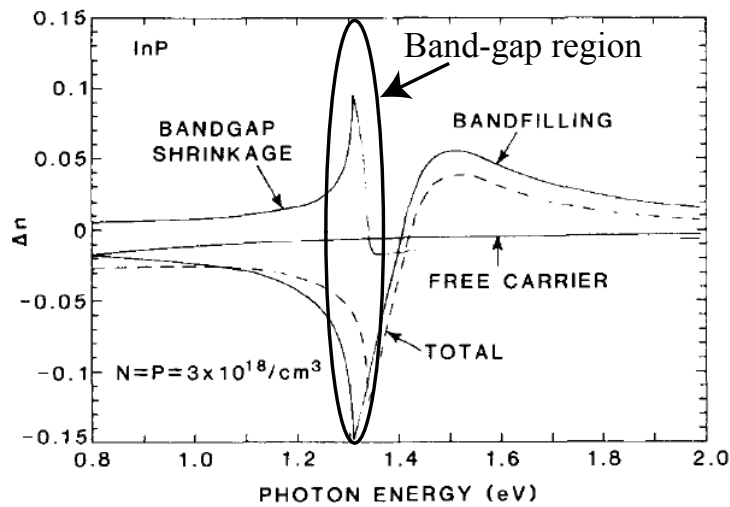


FIGURE 2.4: Predicted individual and net carrier induced refractive index change versus photon energy for InP at carrier concentration  $N=P=3 \times 10^{18} \text{ cm}^{-3}$  [48].

### 2.3.3 Comparison of Quantum Confined Stark Effect and Carrier Induced Electro-Optic Effects

It has been shown that the carrier induced  $\Delta n$  value can typically be an order of magnitude greater than that of an applied electric field [48, 49]. However, the QCSE is known to achieve faster switching speeds as the mechanism is not limited by the spontaneous recombination lifetime of free carriers, thus may be seen as more suitable for high speed applications [50]. Nevertheless, despite the relatively low switching speed of devices based on current injection, numerous devices have been successfully produced such as phase modulators [51], high speed tunable laser diodes [52] and optical switches/demultiplexers [53, 54].

### 2.3.4 Chirp Parameter

The equation of a guided EM wave propagating in the  $z$  direction may be described by:

$$E = E_0 \exp^{j(\omega t - \kappa z)}, \quad (2.1)$$

where  $E_0$  is the amplitude of the wave,  $\omega$  is the angular frequency,  $t$  is time and  $\kappa$  is the wave number.

Soref has shown that by including the effect of optical loss in the equation for the complex wave number we obtain [55]:

$$\kappa = \frac{2\pi(n + jk)}{\lambda_0}, \quad (2.2)$$

where  $n$  is the real part and  $k$  the imaginary part (linear extinction coefficient) of the complex refractive index, and  $\lambda_0$  is the free space wavelength.

We can define the propagation constant of the wave,  $\beta$ , as being the phase change per unit length, equal to:

$$\beta = \frac{2\pi n}{\lambda_0}, \quad (2.3)$$

and the absorption term,  $\alpha$ , equal to:

$$\alpha = \frac{4\pi k}{\lambda_0}. \quad (2.4)$$

Of interest are the electro-optic effects that result in a change of the complex index i.e.:

$$\Delta \mathbf{n} = \Delta n + j\Delta k. \quad (2.5)$$

This change transpires in a perturbation of the mode in the form of:

$$\exp^{j(\Delta\beta + j\Delta\alpha/2)z}, \quad (2.6)$$

where

$$\Delta\beta = \frac{2\pi\Delta n}{\lambda_0}, \quad (2.7)$$

and

$$\Delta\alpha = \frac{4\pi\Delta k}{\lambda_0}. \quad (2.8)$$

A key parameter in the design of electro-optic based devices is the wavelength dependant chirp parameter,  $\rho$  [34, 55]. It is defined as being the ratio of the changes in the real to the imaginary parts of the refractive index, i.e.:

$$\rho = \frac{\Delta n}{\Delta k} = \frac{2\Delta\beta}{\Delta\alpha} = \frac{4\pi\Delta n}{\lambda_0\Delta\alpha}. \quad (2.9)$$

In practical terms  $\rho$  can be viewed as the measure of the relative strength of the phase versus the amplitude modulation at a given bias level. It has been shown that for MZI devices based on electro-refractive phase modulation, higher  $\rho$  values are desirable for successful operation, i.e. maximum refractive index change with minimum losses [55].

## 2.4 Constitutional Component Design

### 2.4.1 Waveguide Design

From slab waveguide theory it is known that in optical waveguides, photon confinement in the vertical direction (1-D) is achieved by introducing an optical core layer of higher refractive index than the surrounding cladding layers during the epitaxial growth stage. However, for waveguiding in both the vertical and the lateral direction (2-D), one must also introduce lateral confinement of carriers and photons. In this work the etched ridge waveguide technique was chosen to induce lateral index guiding with current confinement. There are two commonly used regimes for achieving such index guiding: shallowly etched and deeply etched ridges, as shown in Fig. 2.5. Relatively weak photon confinement is achieved in shallowly etched structures by selectively etching a ridge into the semiconductor material, whereby the effective refractive index of the region directly below the etched surface decreases, providing optical confinement due to the step-like refractive index profile between the etched and non-etched areas. Current injection efficiency here can be high, however, as the etching ceases just above the active region, lateral confinement of the carriers is not optimum, thus losses arise from diffusion and recombination of carriers that do not contribute towards gain [34]. Scattering losses tend to be low as there is little interaction between the optical mode and the sidewalls of the ridge. Single lateral mode operation is typically

readily obtainable with robust tolerances to fabrication of waveguide width and height [56].

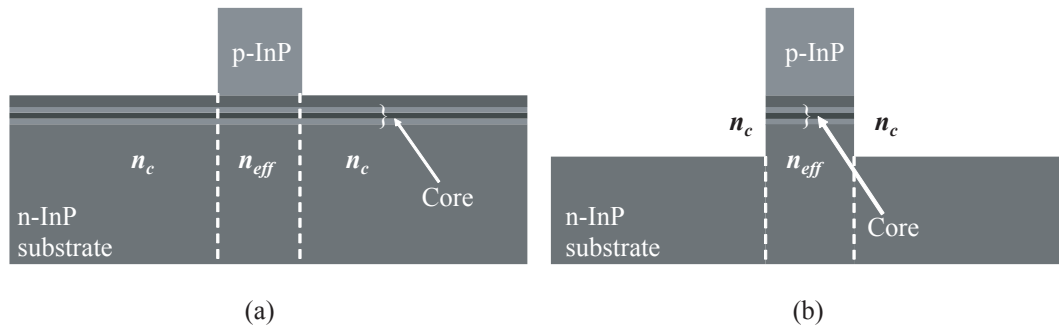


FIGURE 2.5: Schematic of a (a) shallow etched waveguide and (b) a deeply etched waveguide.

Deep etching (through the core) allows for stronger confinement of the optical mode as there is a large contrast in refractive index between the waveguide and the surrounding medium (usually air). This may be beneficial in situations where tightly curved waveguides or high levels of confinement are necessary. However, difficulties may arise in achieving single-mode operation as very narrow waveguide widths are typically required that are inherently sensitive to any variations in waveguide dimensions. Also, scattering losses may be an issue if the sidewalls of the ridges are not sufficiently smooth as, unlike the shallow etched case, there is a strong interaction between the mode and the sidewall. Another loss source arises from the fact that the active layers are exposed to the atmosphere, therefore non-radiative recombination transpires due to the dangling bond surface states. These recombination events lead to the generation of phonons and device heating and thus the potential for decreasing device performance and lifetime.

For the reasons highlighted above, shallow etched waveguides were used in this project to achieve stable single-mode guides. Single-mode operation is required in long haul telecommunications to avoid effects of modal dispersion. In order to comprehensively design the waveguides, a commercially available 2-D mode solver package, FimmWave, was used to determine the correct geometrical structure of the guides. FimmWave models waveguide structures using a rigorous fully vectorial formalism based on the film mode matching method. It has been shown previously that the best effective index contrast,  $\Delta n$ , for this material occurs when the ridge waveguide is shallow etched down to the top of the optical core layer,

i.e. an etch depth of 1920 nm [56]. This is also beneficial in the fabrication process as this is where the first aluminium containing layer appears, which may be used as a dry etch stop layer (detailed in the next chapter). At this etch depth, the simulations yield ridge and cladding effective indices of  $n_{eff}=3.201$  and  $n_c=3.166$  respectively, therefore an index contrast of  $\Delta n=0.035$ . By varying the ridge width one can also determine the modal index of the fundamental TE polarised mode, as well as higher order modes. This is useful to determine at which width the higher order modes are suppressed, i.e. the appropriate width for single-mode operation. Fig. 2.6 shows a plot of the waveguide modal index versus ridge width for the fundamental, 1<sup>st</sup> and 2<sup>nd</sup> order TE polarised modes at a wavelength of 1550 nm. For a waveguide width of 2  $\mu\text{m}$  and below, only the fundamental mode is supported, therefore this width was chosen for the guides.

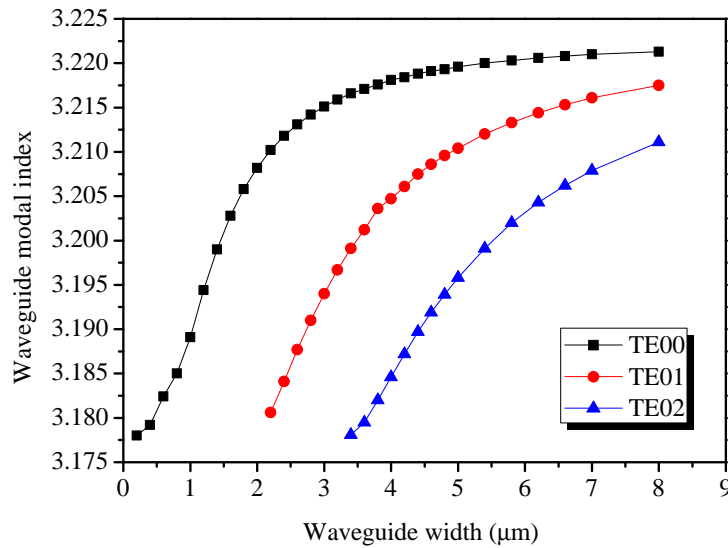


FIGURE 2.6: Waveguide modal index versus ridge width for the fundamental, 1<sup>st</sup> and 2<sup>nd</sup> order TE polarised modes at a wavelength of 1550 nm .

Fig. 2.7 shows the simulated optical field contour profile of a 2  $\mu\text{m}$  wide, 1920 nm deep ridge where the single-mode is sufficiently confined within the structure. The refractive indices of the epitaxial layers used in the simulation were calculated using equations derived in [57], and from the website for thin film and bulk index of refraction and photonics calculations, as detailed in [58]. The optical confinement factor per well for the TE polarisation state,  $\Gamma$ , was also obtained from the simulations, and is equal to 0.01.

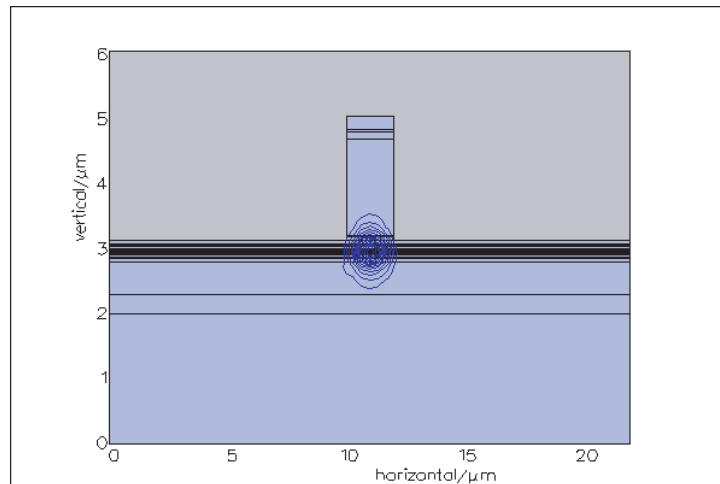


FIGURE 2.7: Simulated waveguide mode contour plot for the  $2\ \mu\text{m}$  wide,  $1920\ \text{nm}$  deep ridge.

### 2.4.2 Curved Waveguide Design: Assessment of Bending Losses

As both the MZIs and ring lasers require curved waveguides, it is important to consider the effects of bending losses in these sections [59]. A 3-D beam propagation method (BPM) simulation, using Rsoft BeamPROP, was performed in order to ascertain the waveguide losses as a function of bend radius. This software allows for superior, robust and efficient results via an implementation of the BPM based on an implicit finite-difference scheme. Fig. 2.8 shows the bending loss as a function of waveguide bend radius for the single-mode guides. From the plot, it is evident that negligible losses are incurred for a bend radius of down to  $250\ \mu\text{m}$ , therefore this value was chosen to be the minimum allowed in subsequent designs.

### 2.4.3 Multi-Mode Interference Coupler Design

A vital function in any integrated photonic device is the splitting, routing and recombination of light waves around the circuit. MMI couplers are suitable candidates for this purpose due to several advantages such as multiple access ports, minimal insertion loss figures, compactness, polarisation and wavelength insensitivity, and fabrication robustness [60]. They also lend themselves favourably to other more complex devices such as ring lasers, modulators and MZIs, hence the

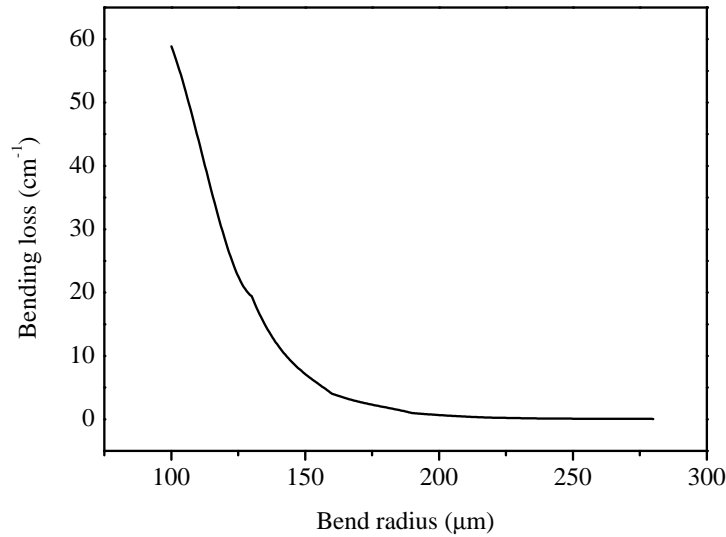


FIGURE 2.8: Simulated BPM bending loss as a function of bend radius for the  $2\ \mu\text{m}$  wide,  $1920\ \text{nm}$  deep ridge waveguide.

relevance to this body of work. MMI couplers operate by exploiting the self imaging principle in uniform index slab waveguides, as first proposed by Bryngdahl [61], in which specific integral relationships exist among the propagation constants of different modes, producing equivalent images of the input field along the length of the coupler. Fig. 2.9 shows a multi-mode waveguide of physical width  $W$ , effective ridge index  $n_{eff}$  and effective cladding index  $n_c$ . The waveguide supports  $m$  lateral modes (typically  $m \geq 3$ ) at the free space wavelength  $\lambda_0$  with propagation constants  $\beta_i$ , where  $i = 0, 1, 2, 3, \dots, (m - 1)$ .

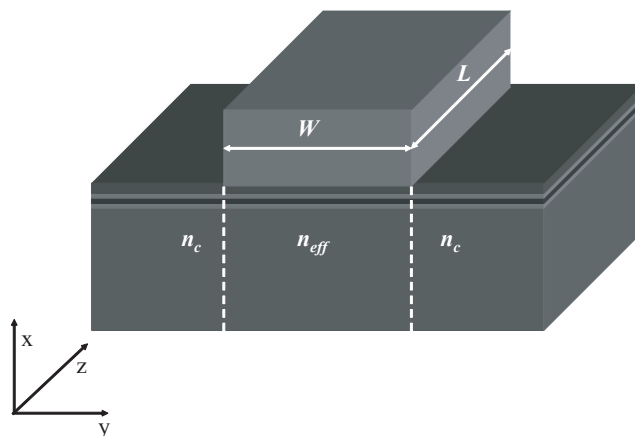


FIGURE 2.9: Multi-mode waveguide of width  $W$ , effective ridge index  $n_{eff}$  and effective cladding index  $n_c$ .

From slab waveguide theory and [62], it can be shown that the effective ridge index,  $n_{eff}$ , is related to both the propagation constant,  $\beta_i$ , and the lateral angular wavenumber,  $k_{yi}$ , via the material dispersion equation:

$$n_{eff}^2 k_0^2 = k_{yi}^2 + \beta_i^2. \quad (2.10)$$

In this relationship

$$k_0 = \frac{2\pi}{\lambda_0}, \quad (2.11)$$

and

$$k_{yi} = \frac{(i+1)\pi}{W_{eff}}, \quad (2.12)$$

where  $W_{eff}$  is the “effective” waveguide width taking into account the Goos-Hänchen shift for low contrast waveguides. This effective width is defined as:

$$W_{eff} \simeq W + \left(\frac{\lambda_0}{\pi}\right) \left(\frac{n_c}{n_{eff}}\right)^{2\sigma} / \sqrt{n_{eff}^2 - n_c^2}, \quad (2.13)$$

where  $\sigma=0$  for the TE polarisation state and  $\sigma=1$  for TM. Using a binomial expansion with  $k_{yi}^2 \ll k_0^2 n_{eff}^2$  and equations 2.10-2.12 we obtain:

$$\beta_i \simeq n_{eff} k_0 - \frac{(i+1)^2 \pi \lambda_0}{4n_{eff} W_{eff}^2}. \quad (2.14)$$

We can specify the beat length  $L_\pi$  between the fundamental ( $i=0$ ) and first order ( $i=1$ ) modes as:

$$L_\pi = \frac{\pi}{\beta_0 - \beta_1} \simeq \frac{4n_{eff} W_{eff}^2}{3\lambda_0}, \quad (2.15)$$

therefore the propagation constants spacing is:

$$(\beta_0 - \beta_i) \simeq \frac{i(i+2)\pi}{3L_\pi}. \quad (2.16)$$

Soldano has next shown, using guided mode propagation analysis, that an input field profile at  $z=0$  will be decomposed into the modal field distributions  $\psi_i(y)$  of all modes, i.e.:

$$\Psi(y, 0) = \sum_i c_i \psi_i(y), \quad (2.17)$$

where  $c_i$  is the field excitation coefficient, estimated from the overlap integral between the input field profile,  $\Psi(y, 0)$ , and  $\psi_i(y)$ :

$$c_i = \frac{\int \Psi(y, 0) \psi_i(y) dy}{\sqrt{\int \psi_i^2(y) dy}}. \quad (2.18)$$

If the “spatial spectrum” of the input field,  $\Psi(y, 0)$ , only excites guided modes then it becomes:

$$\Psi(y, 0) = \sum_{i=0}^{m-1} c_i \psi_i(y), \quad (2.19)$$

implying the decomposition of the input field into the modal field distributions of all the possible guided modes in the multi-mode waveguide.

The field profile at any position along the  $z$  axis may be expressed as a linear superposition of the eigenmodes,  $\psi_i(y)$ , i.e. [62]:

$$\Psi(y, z) = \sum_{i=0}^{m-1} c_i \psi_i(y) \exp[j(\omega t - \beta_i z)], \quad (2.20)$$

On inspection of equation 2.20, the phase of the fundamental mode may be taken out as a common factor and then dropped such that the equation is time independent and the field profile now becomes:

$$\Psi(y, z) = \sum_{i=0}^{m-1} c_i \psi_i(y) \exp[j(\beta_0 - \beta_i)z]. \quad (2.21)$$

The field at a distance  $L$  may now be found by substituting equation 2.16 into equation 2.21:

$$\Psi(y, L) = \sum_{i=0}^{m-1} c_i \psi_i(y) \exp \left[ j \frac{i(i+2)\pi}{3L\pi} L \right]. \quad (2.22)$$

The images formed along the multi-mode waveguide are thus dependant on the modal excitation,  $c_i$ , and the mode phase factor equal to:

$$\exp \left[ j \frac{i(i+2)\pi}{3L_\pi} L \right]. \quad (2.23)$$

Under certain conditions the output field is a complete reproduction of the input field, i.e. self imaging occurs. On inspection of equation 2.22 it is observed that  $\Psi(y, L)$  shall be a reproduction of  $\Psi(y, 0)$  when:

$$\exp \left[ j \frac{i(i+2)\pi}{3L_\pi} L \right] = 1 \text{ or } (-1)^i. \quad (2.24)$$

It has been shown that the first and second conditions are fulfilled when:

$$L = p(3L_\pi) \text{ with } p = 0, 1, 2, \dots \quad (2.25)$$

for  $p$  even and  $p$  odd respectively. The factor  $p$  denotes the periodicity of the image formation along the waveguide. Direct images are formed when  $p$  is even, and mirrored images formed when  $p$  is odd, as shown in Fig. 2.10.

Now by looking at the images formed half way between the direct and mirrored images, i.e. at distances:

$$L = \frac{p}{2}(3L_\pi) \text{ with } p = 1, 3, 5, \dots \quad (2.26)$$

we find that

$$\Psi(y, \frac{p}{2}(3L_\pi)) = \frac{1 + (-j)^p}{2} \Psi(y, 0) + \frac{1 - (-j)^p}{2} \Psi(-y, 0). \quad (2.27)$$

This last condition represents a pair of images in quadrature with amplitudes of  $1/\sqrt{2}$  formed at distances  $z = \frac{1}{2}(3L_\pi), \frac{3}{2}(3L_\pi), \dots$ , as shown in Fig. 2.10.

For the MZIs in this work,  $2 \times 2$  MMIs are required. There are two suitable regimes of self imaging in multi-mode waveguides for this case. These are the  $N \times N$  *general interference* regime in which the images are independent of modal excitation conditions, and the  $2 \times N$  *restricted paired interference* regime in which

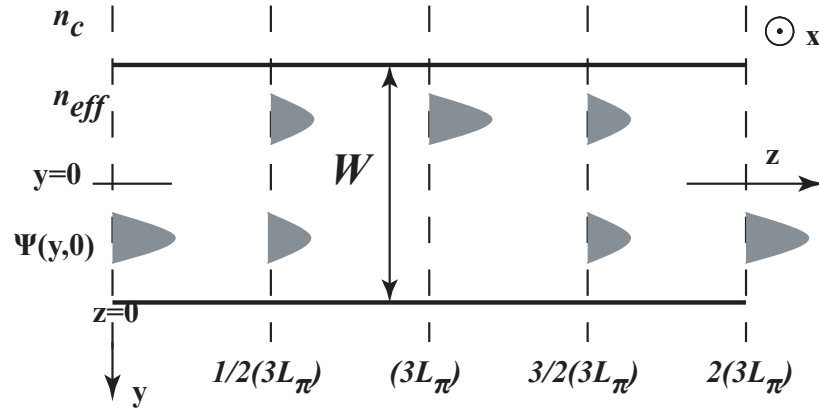


FIGURE 2.10: Graphical representation of the imaging properties in the multi-mode waveguide with an input field injected at  $z=0$ .

the images are dependant on the modal excitation, i.e. where the input field is launched ( $N$  is the number of inputs/outputs).

In general self imaging couplers, as shown schematically in Fig. 2.11 where  $N=2$ , the first single image distance is found at  $3L_\pi$  with the first  $N$ -fold image being found at:

$$L = \frac{3L_\pi}{N}. \quad (2.28)$$

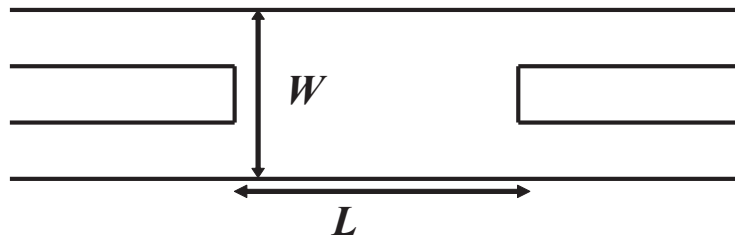


FIGURE 2.11: Schematic layout of a  $2 \times 2$  general interference MMI coupler.

Compare this to the restricted paired case, as shown in Fig. 2.12, where the first single image may be found at  $L_\pi$  and the first  $N$ -fold image at:

$$L = \frac{L_\pi}{N}. \quad (2.29)$$

At first sight, one would therefore assume that the restricted paired type would offer a shorter  $2 \times 2$  coupler length. However, this is not necessarily the case as  $L_\pi$  will most likely differ between the two situations. This may be explained

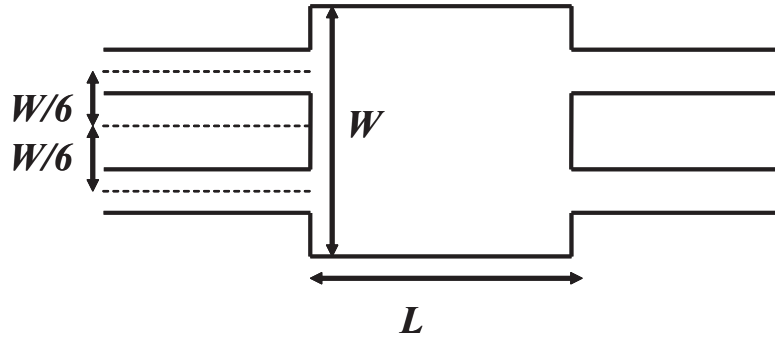


FIGURE 2.12: Schematic layout of a  $2 \times 2$  restricted paired interference MMI coupler.

as follows. A realistic distance must be kept between the access waveguides such that no evanescent field coupling occurs between them leading into the multi-mode waveguide. For these devices, this distance has been chosen to be at least  $2 \mu\text{m}$ . As the access guides are also  $2 \mu\text{m}$  wide, and the restricted paired couplers require that the input waveguides be located at  $\pm W/6$ , this would imply that the minimum physical coupler width,  $W$ , would be  $12 \mu\text{m}$ . As there are no restrictions in the general coupler case, a minimum coupler width of  $6 \mu\text{m}$  is allowed. However, as detailed in [62], general interference mechanisms may suffer from relatively higher losses than their paired equivalents in weakly guiding structures due to decreased image resolution. This is because reducing the width of the coupler also reduces the number of guided modes, resulting in an increase in the influence of width deviations on the splitting ratio and also a deterioration of the crosstalk [63]. Owing to these factors, restricted paired type couplers were chosen for this work, even though the coupler length may be slightly longer.

In order to allow for as many modes as possible in the multi-mode guide for increased image resolution, a physical width of  $15 \mu\text{m}$  was chosen. By inserting this value into equation 2.13 with  $n_{\text{eff}}=3.201$ ,  $n_c=3.166$  and  $\lambda_0=1550 \text{ nm}$ , we obtain an effective waveguide width  $W_{\text{eff}} \simeq 16 \mu\text{m}$ . One can now calculate the coupler length that yields 2 self images at the coupler output using equation 2.29. This length is calculated to be  $355 \mu\text{m}$ . In order to verify this result, a 3-D BPM simulation was also carried out. Fig. 2.13 shows the simulated power monitor values of the output waveguides, that are placed at  $\pm W/6$ , as a function of coupler length. The curves intersect each other at a coupler length of  $354 \mu\text{m}$ , indicating equal power splitting. This coupler length compares well with the theoretical value obtained of  $355 \mu\text{m}$ . A cross sectional view of the coupler output at this length is also shown in Fig. 2.14, illustrating equal mode profiles in each output waveguide, as required.

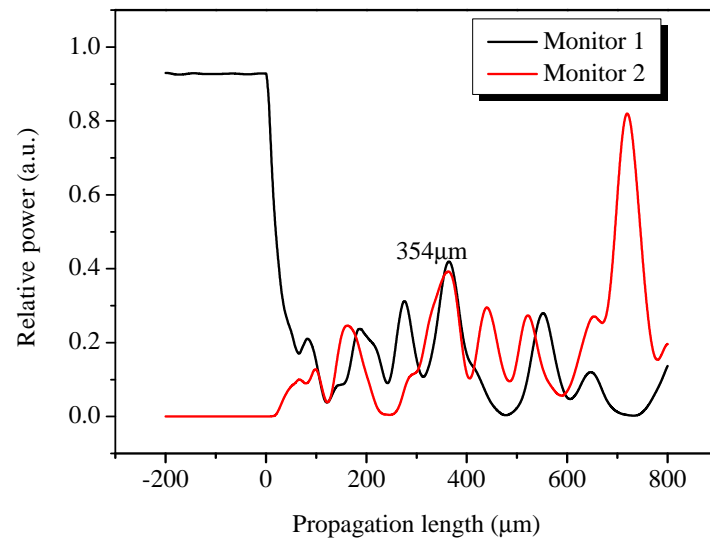


FIGURE 2.13: 3-D BPM simulation of the restricted paired coupler with a physical width of  $15 \mu\text{m}$ . The 3 dB coupling length appears at  $354 \mu\text{m}$ .

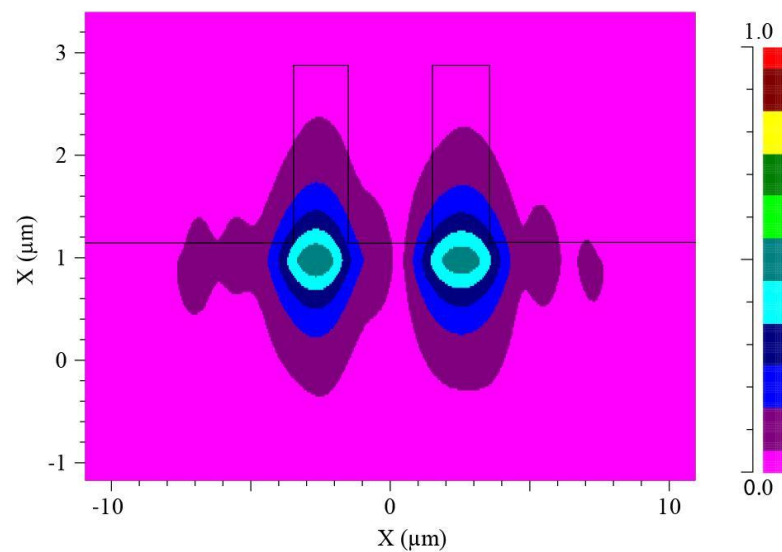


FIGURE 2.14: Cross sectional view of the simulated coupler illustrating the equal mode profiles in each output waveguide at  $L=354 \mu\text{m}$ .

It has also been shown in [62] and [64] that the phase relations between the MMI outputs can be derived and that they exhibit a  $\pi/2$  difference in the case when the exact 3 dB coupling length is achieved. As will be shown in section 2.5, this phase difference is paramount in the operation of MZIs utilising such 3 dB MMI couplers.

Another important factor in the design of MMI couplers is the understanding and elimination of undesirable back reflections arising from the coupler itself [65]. Hanfoug has shown that by chamfering off any of the right angled edges of the coupler corners, suppression of the back reflections by more than 10 dB is achievable [66]. This approach has also been taken in the design of the MMI couplers here, as illustrated in Fig. 2.15. The angle is chosen to be  $31^\circ$  as this is much larger than the divergence angle of the light entering the MMI structure from the single-mode input waveguide (estimated to be around  $10^\circ$  from BPM simulations).

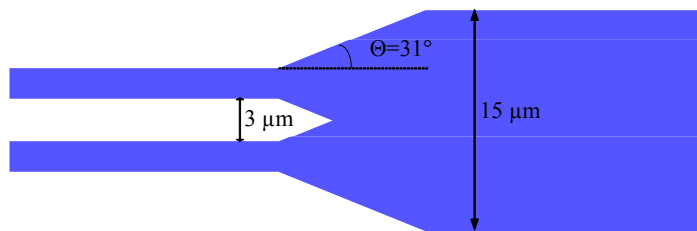


FIGURE 2.15: Geometry of the MMI device design including reflection reduction measures as reported in [66].

## 2.5 Mach-Zehnder Interferometer Design

MZIs have been used successfully as a basis for high speed optical switching [53], wavelength demultiplexing [67] and wavelength conversion [68]. In this work, the MZI is constructed by adjoining two 3 dB couplers/combiners together via passive waveguide interconnects. Also included are monolithically integrated phase shifters, comprising of active waveguide sections on each arm allowing for electrorefractive phase modulation. The active/passive integration technique shall be discussed in the following chapter. Important performance requirements for the MZI include low insertion losses, high phase shift efficiencies and low crosstalk

values, leading to a desirably high extinction ratio (ER) [63]. In order to minimise the losses, one must carefully design the MZI using low loss waveguides with negligible bending losses, therefore curved waveguides of  $500\ \mu\text{m}$  bend radius were employed, so also allowing sufficient space between input/output waveguides for fibre alignment. As the ER in a MZI is limited by the imbalance of the splitting and recombining in the couplers used, it is vital that the couplers are designed correctly. Also, any output phase deviations will also compromise the ER performance of the device. The stable balance and phase performance of MMIs, as well as their polarisation/wavelength insensitivity, make them highly suitable candidates in the realisation of MZIs.

By considering the input and output fields of the MMI coupler, the theoretical operating principle of the MZI may be described by means of transfer matrix theory [69]. Firstly, the input/output relationships of an ideal 3 dB  $2\times 2$  coupler, as shown in Fig. 2.16, is determined.

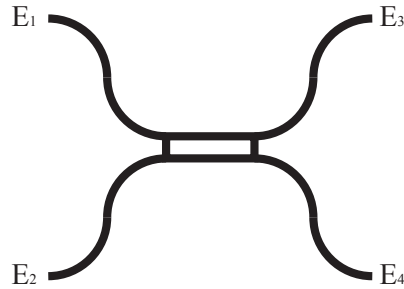


FIGURE 2.16: Schematic of an ideal 3 dB  $2\times 2$  MMI coupler.

We can relate the input fields,  $E_1$  and  $E_2$ , to the output fields,  $E_3$  and  $E_4$ , via the complex transfer matrix:

$$\begin{bmatrix} E_3 \\ E_4 \end{bmatrix} = \frac{1}{\sqrt{2}} \begin{bmatrix} 1 & j \\ j & 1 \end{bmatrix} \begin{bmatrix} E_1 \\ E_2 \end{bmatrix}, \quad (2.30)$$

where  $j=\sqrt{-1}$  denotes a  $\pi/2$  phase difference between  $E_1$  and  $E_4$  or  $E_2$  and  $E_3$ . If two couplers are connected, as shown in Fig. 2.17, then a MZI is formed, where a phase difference,  $\Delta\phi$ , may exist between the upper and lower arms.

One can define the transfer matrix of the interferometric arms section as being (assuming a phase difference of  $\Delta\phi$  between the arms):

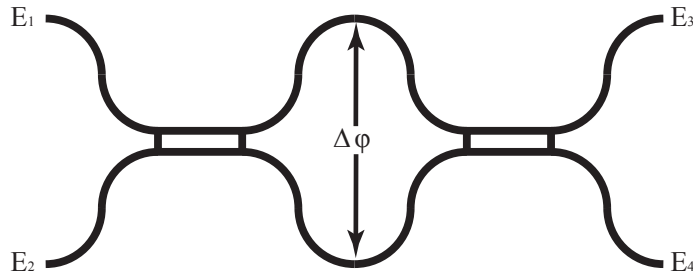


FIGURE 2.17: Schematic of a MZI consisting of two adjoined 3 dB 2×2 MMI couplers.

$$\begin{bmatrix} 1 & 0 \\ 0 & \exp^{j\Delta\phi} \end{bmatrix}, \quad (2.31)$$

therefore the complete transfer matrix for the MZI can be determined by multiplying the individual matrices of the MMIs and the interferometric arms together [70], i.e.:

$$\begin{bmatrix} E_3 \\ E_4 \end{bmatrix} = \frac{1}{\sqrt{2}} \begin{bmatrix} 1 & j \\ j & 1 \end{bmatrix} \begin{bmatrix} 1 & 0 \\ 0 & \exp^{j\Delta\phi} \end{bmatrix} \frac{1}{\sqrt{2}} \begin{bmatrix} 1 & j \\ j & 1 \end{bmatrix} \begin{bmatrix} E_1 \\ E_2 \end{bmatrix}, \quad (2.32)$$

which can be simplified to:

$$\begin{bmatrix} E_3 \\ E_4 \end{bmatrix} = \frac{1}{2} \begin{bmatrix} (1 - \exp^{j\Delta\phi}) & j(1 + \exp^{j\Delta\phi}) \\ j(1 + \exp^{j\Delta\phi}) & (-1 + \exp^{j\Delta\phi}) \end{bmatrix} \begin{bmatrix} E_1 \\ E_2 \end{bmatrix}. \quad (2.33)$$

If  $\Delta\phi=0$ , then the MZI transfer matrix yields:

$$\begin{bmatrix} E_3 \\ E_4 \end{bmatrix} = j \begin{bmatrix} 0 & 1 \\ 1 & 0 \end{bmatrix} \begin{bmatrix} E_1 \\ E_2 \end{bmatrix}, \quad (2.34)$$

i.e.  $|E_3|=|E_2|$  and  $|E_4|=|E_1|$  with the phase relationship preserved.

However, if  $\Delta\phi=\pi$ , the MZI transfer matrix now yields:

$$\begin{bmatrix} E_3 \\ E_4 \end{bmatrix} = \begin{bmatrix} 1 & 0 \\ 0 & -1 \end{bmatrix} \begin{bmatrix} E_1 \\ E_2 \end{bmatrix}, \quad (2.35)$$

i.e.  $|E_3|=|E_1|$  and  $|E_4|=|E_2|$  except now one is  $\pi$  phase shifted with respect to the other.

It is now apparent that the MZI can act as a switch where  $\Delta\phi=0$  corresponds to the so called cross state, and  $\Delta\phi=\pi$  corresponds to the bar state. Such operations can be explained graphically using Fig. 2.18 and Fig. 2.19.

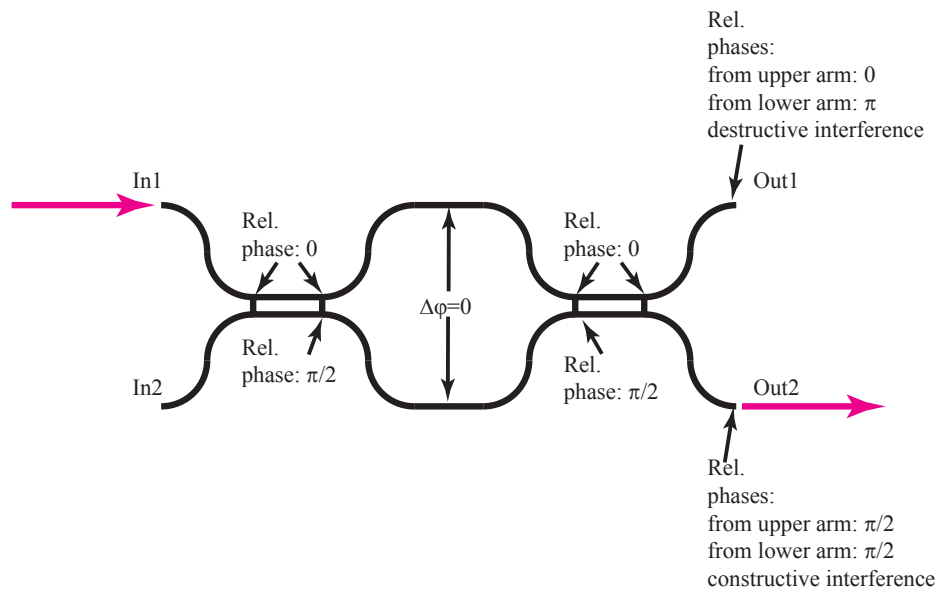


FIGURE 2.18: Schematic illustration of the MZI in the cross state.

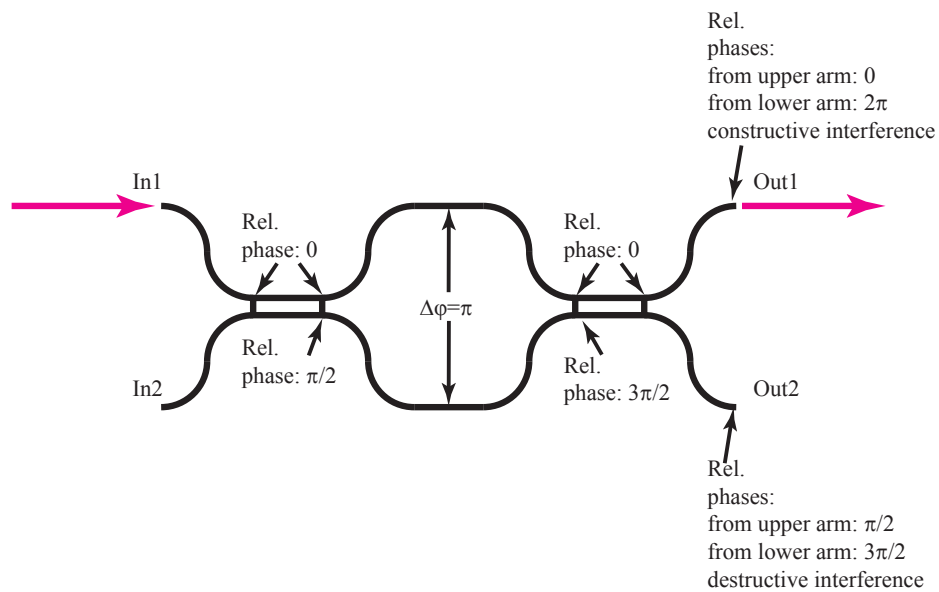


FIGURE 2.19: Schematic illustration of the MZI in the bar state.

Firstly, if we consider an input optical field being injected at  $In_1$  in the schematic of Fig. 2.18, it will be guided towards the first MMI coupler which splits the signal in half with a constant phase difference of  $\pi/2$  between the two outputs. The signals then traverse the interferometer arms to recombine at the second coupler. In the absence of a phase shift difference between the arms, i.e.  $\Delta\phi=0$ , the MZI is balanced such that there is destructive interference at  $Out_1$  and constructive interference at  $Out_2$ , therefore the MZI is in the cross state. However, by inducing a  $\Delta\phi=\pi$  phase shift difference between the two arms, as in Fig. 2.19, the MZI is now balanced such that there is constructive interference at  $Out_1$  and destructive interference at  $Out_2$ , therefore the MZI is now in the bar state. The additional phase shift difference,  $\Delta\phi$ , between the two arms may be obtained by inducing a refractive index change,  $\Delta n$ , in one (or both) of the phase shifting sections according to [55, 63, 70]:

$$\Delta\phi = \Delta\beta L = k_0\Delta nL, \quad (2.36)$$

in which  $k_0=2\pi/\lambda_0$  and  $L$  is the length of the phase shifting section.

The theoretical performance of the MZI can be simulated in terms of the ER as a function of the chirp parameter,  $\rho$ . As mentioned previously, it is known that various factors contribute to achieving a high ER, such as the reduction of any imbalance between the interferometer arms, leading to a lower crosstalk level. In order to obtain a low crosstalk value it is imperative that the power levels in both the interferometer arms are equal. If they are not level then the destructive inference that is required at the off output of the MZI will not be sufficient, therefore leading to an increased power level at this output, lowering the ER value [63].

In the following ER analysis, perfect imaging in the MMI couplers is assumed and the electro-optic interaction is induced over a length,  $L$ , in order to produce a uniform perturbation of the waveguide of  $\Delta\beta + j\Delta\alpha/2$ . The lossless initial state of the device is defined as being when both guides are phase matched, i.e.  $\Delta\beta=0$  and  $\Delta\alpha=0$ , thus the MZI is in the cross state. The device switches to the bar state when there is a velocity mismatch between the upper and lower guides of  $\Delta\beta + j\Delta\alpha/2$  [55].

The power at Out2 may be defined as being  $P_{out2} \simeq E_t E_t^*$ , where  $E_t$  is the total optical field at the second MMI equal to:

$$E_t = \left( \frac{E_0}{\sqrt{2}} \right) + \left( \frac{E_0}{\sqrt{2}} \right) \exp^{-\Delta\alpha L/2} \exp^{j\Delta\beta L}, \quad (2.37)$$

thus

$$P_{out2} = \left( \frac{E_0^2}{2} \right) [1 + \exp^{-\Delta\alpha L/2} \exp^{j\Delta\beta L}] [1 + \exp^{-\Delta\alpha L/2} \exp^{-j\Delta\beta L}]. \quad (2.38)$$

With no mismatch between the arms, i.e.  $\Delta\beta=0$  and  $\Delta\alpha=0$ , constructive interference occurs at this output and the transmission is at a maximum, i.e.  $2E_0^2$ . Taking the normalised output power as  $P_{out2}/P_{in}$  with  $P_{in}=2E_0^2$ , then the throughput at this output is defined as:

$$P_{out2}/P_{in} = \left( \frac{1}{4} \right) [1 + \exp^{-\Delta\alpha L} + 2 \exp^{-\Delta\alpha L/2} \cos(\Delta\beta L)]. \quad (2.39)$$

Now, if we substitute the chirp parameter,  $\rho = \frac{2\Delta\beta}{\Delta\alpha}$ , into equation 2.39, the output power becomes:

$$P_{out2}/P_{in} = \left( \frac{1}{4} \right) [1 + \exp^{-2\Delta\beta L/\rho} + 2 \exp^{-\Delta\beta L/\rho} \cos(\Delta\beta L)], \quad (2.40)$$

where  $\Delta\beta L = \Delta\phi$ . Note,  $P_{out1}/P_{in}$  is defined simply by:

$$P_{out1}/P_{in} = \left( \frac{1}{4} \right) [1 + \exp^{-2\Delta\beta L/\rho} - 2 \exp^{-\Delta\beta L/\rho} \cos(\Delta\beta L)]. \quad (2.41)$$

Fig. 2.20 shows a plot of the normalised MZI cross output,  $P_{out2}/P_{in}$ , as a function of  $\Delta\phi$  for two different values of  $\rho$ , i.e. 10 and 100. The higher value of  $\rho$  leads to a greater value of ER, therefore it is prudent to maximise  $\rho$  in order to obtain a successful device in terms of ER. A general rule of thumb for low loss phase modulation is to have a chirp parameter of 10 or greater [34].

As the MZI is formed by adjoining two MMI couplers as discussed in section 2.4.3, the BPM simulation of the MMI may be extended to the MZI case. The MZI

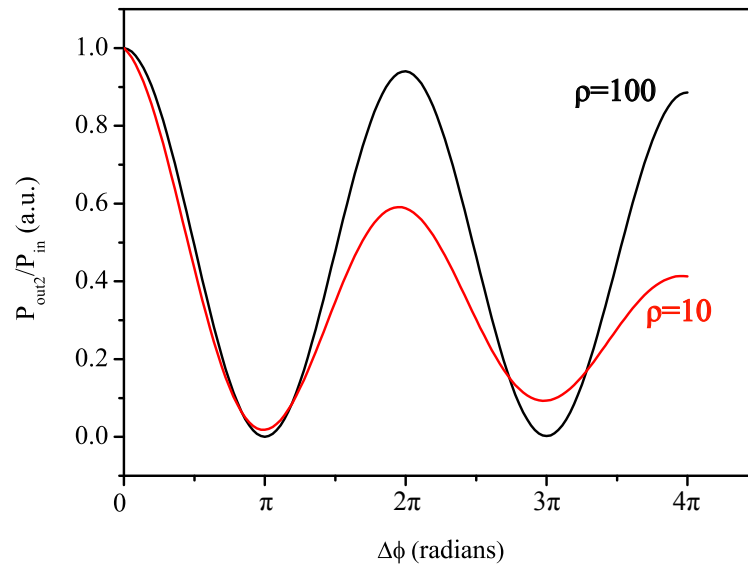


FIGURE 2.20: Simulated MZI cross output as a function of  $\Delta\phi$  for chirp parameter values  $\rho=10$  and  $\rho=100$ .

design was constructed with two  $354\ \mu\text{m}$  long MMIs being connected with  $2\ \mu\text{m}$  wide waveguide interconnects. The geometry and results of the BPM are shown in Fig. 2.21. With no phase difference between the interferometer arms, the device is in the cross state as expected. For the actual fabricated device, the phase shifters are chosen to be  $500\ \mu\text{m}$  long in order that sufficient values of  $\Delta n$  are achievable according to equation 2.36.

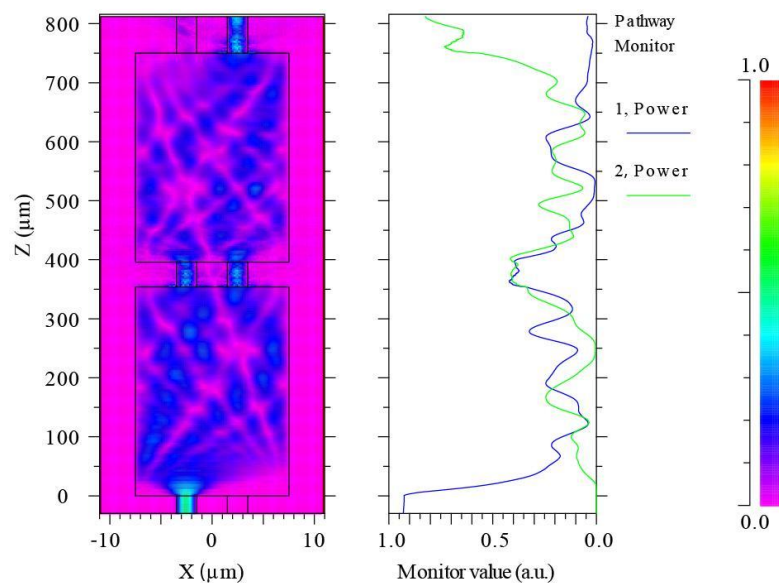


FIGURE 2.21: Simulated BPM MZI performance, in the cross state (i.e.  $\Delta\phi=0$ ), constructed using  $354\ \mu\text{m}$  long MMI couplers.

### 2.5.1 OTDM: MZI Operation Principle as an OTDM demultiplexer

OTDM was first proposed as a viable technique for increasing the usable bandwidth of optical communication systems back in 1970 [71]. The basic idea is that a high bit rate data stream may be constructed by interleaving several lower bit rate streams together, i.e. time multiplexing them for transmission. At the receiver end of the system, the high bit rate stream is then demultiplexed back into the lower bit rate streams for the intended recipients. Each user is assigned a discrete time slot within a particular data frame period, whose length is dependant on the number of users. The data frame period is defined by a periodic pulse train or “clock”.

One of the most critical elements of an OTDM system is the demultiplexer as it is the only component that has to direct signals from the high data rate stream, therefore has a profound effect on the system throughput. Various fibre based technologies have been employed for use as a demultiplexer, essentially performing a logical AND gate function, such as soliton gates [72] and non-linear optical loop mirror (NOLM)s [73, 74]. However, as the intensity dependant phase change in optical fibres is relatively weak, long lengths of fibre and high powers are required in the loop in order to switch the pulses. Also, to achieve the AND gate function, a non-linear element, which can be controlled optically, is required. Thus, a new configuration was presented in order to circumvent these issues, the terahertz optical asymmetric demultiplexer (TOAD) [75]. It consists of a NOLM with a non-linear element asymmetrically placed within the loop, and another directional coupler for the injection of the control pulses. All optical demultiplexing of 250 Gbit/s signals has been achieved using the TOAD, requiring only sub pJ control pulse energies [76]. However, for practical applications, compact, highly stable monolithically integrated solutions would be more advantageous. MZI structures based on cross phase modulation (XPM) have been utilised to this effect with great success. In this configuration the non-linear properties of the integrated semiconductor optical amplifier (SOA)s are exploited in order to achieve the XPM.

The first monolithically integrated MZI with SOAs used as the non-linear elements was presented by Jahn et al. in 1995 with 40 Gbit/s demultiplexing being demonstrated using a bulk GaInAsP device [77]. The experimental set-up used in that work is shown in Fig. 2.22, with the actual device schematic shown within the



## 2.6 Asymmetric Mach-Zehnder Interferometer Design

By increasing the path length of only one of the MZI arms a new device is formed: the asymmetric Mach-Zehnder interferometer ([AMZI](#)). Such AMZIs may be used as tunable filters, wavelength (de)multiplexers or as OCDMA encoders/decoders.

### 2.6.1 DWDM: AMZI Operation Principle as a Wavelength Demultiplexer

As mentioned previously, the technology of combining several wavelengths onto a single fibre for increased bandwidth transmission is termed wavelength division multiplexing ([WDM](#)) and was first proposed by DeLange in 1970 [12]. However, it was later that decade when the first practical research began, focusing on useful applications in telecommunications systems [79]. Several advances have occurred since then with many believing that the emergence of WDM is one of the most important and ground breaking developments in fibre optic transmission as it is known today. One of the main reasons for this was that it allowed the existing network capacity to be increased without the need to re-lay new fibre links [2, 80].

Conceptually, WDM is similar to the frequency division multiplexing schemes employed in radio frequency ([RF](#)) and satellite communications systems. The wavelengths (or optical frequencies) must be sufficiently spaced so as to avoid any interference between adjacent channels. Early WDM systems in the 1990s consisted of 2 to 8 channels spaced at 400 GHz (3.2 nm) in the 1550 nm spectral window. However, as the availability of high quality tunable laser sources increased, a new form of WDM emerged, DWDM. The first DWDM systems had 16 to 40 channels spaced from 100 to 200 GHz (0.8 nm to 1.6 nm) as defined by the International Telecommunication Union ([ITU](#)) standards. Indeed, recent advances include the new field trial record of 3040 km reach with sixty eight 10 Gbit/s non-return to zero ([NRZ](#)) channels and two 40 Gbit/s carrier suppressed return to zero ([CS-RZ](#)) channels transmitted using an all-Raman-based wide reach DWDM platform in a field environment [14].

A vital component in any DWDM system is the wavelength demultiplexer, required to split the spectrum of closely spaced wavelength components into the

individual wavelengths. Such demultiplexers have been realised successfully using both arrayed waveguide grating [81] and MZI structures [82], both based on silica. For the principle of operation as a wavelength demultiplexer, consider the AMZI device structure as depicted in Fig. 2.23, where a path length difference of  $\Delta L$  exists between the arms. If a signal is input at  $In_1$ , it will be divided equally by the first MMI between the two arms of the AMZI with a constant phase difference of  $\pi/2$  between the two signals, as with the MZI structure described in section 2.5. However, since there is a path length difference between the two arms of  $\Delta L$ , there also exists a further phase lag of  $\beta\Delta L$  in the lower arm. In the second MMI, the signal from the lower arm undergoes another  $\pi/2$  phase delay in traversing to  $Out_1$ . Thus the total signal at  $Out_1$  consists of the interference of the signal with a relative phase of 0, with the signal with a relative phase of  $\pi/2$  from the first MMI,  $\beta\Delta L$  from the lower arm and  $\pi/2$  from the second MMI, i.e.  $\pi + \beta\Delta L$ . Conversely, at  $Out_2$  the signal from the upper arm lags the signal from the lower arm by  $\pi/2$ . Therefore the total signal at  $Out_2$  is given by the interference between the upper arm signal with  $\pi/2$  and the lower arm signal with  $\pi/2 + \beta\Delta L$ .

When  $\Delta\phi = \beta\Delta L = m\pi$ , and the integer  $m$  is odd, then the resultant interference at  $Out_1$  will be constructive and destructive at  $Out_2$ . Conversely if  $m$  is even, the resultant interference at  $Out_1$  will now be destructive with constructive interference at  $Out_2$ . Thus the wavelengths for which  $\beta\Delta L = m\pi$  where  $m$  is odd will pass from  $In_1$  to  $Out_1$  and the wavelengths for which  $\beta\Delta L = m\pi$  where  $m$  is even will pass from  $In_1$  to  $Out_2$ . Therefore if there are only two wavelengths, one where  $m$  is odd and one where  $m$  is even, then the device acts as a  $1 \times 2$  wavelength demultiplexer. Since the device is reciprocal it can also be used as a  $2 \times 1$  wavelength multiplexer, shuffling the odd and even signals back together [9, 70].

By inserting a phase shifting section into one of the AMZI arms, the device may perform as a tunable wavelength filter. By changing the refractive index of one of the arms by current injection or indeed reverse bias voltage as detailed earlier, the phase relationships between the signals in the two arms causes different wavelengths to be coupled out by virtue of constructive and destructive interference.

The transmission characteristics of the AMZI can be described by slightly adjusting the transfer matrix of the MZI as in equation 2.31. To account for the additional phase shift introduced by the longer arm,  $\beta\Delta L$ , the matrix now becomes:

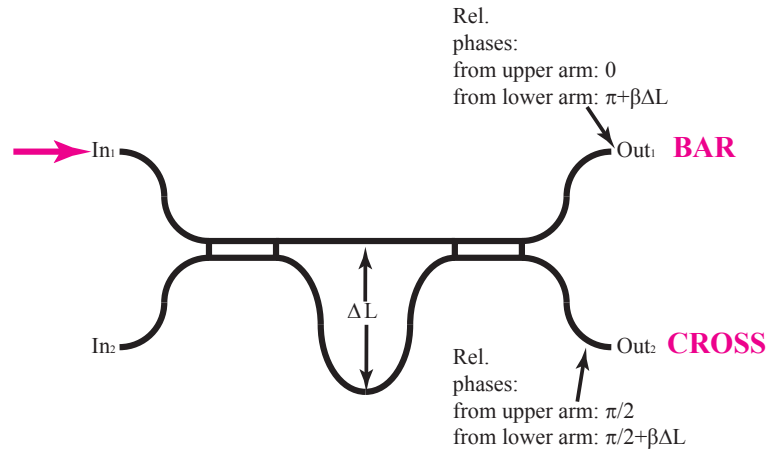


FIGURE 2.23: Schematic of an AMZI constructed by adjoining two 3 dB  $2 \times 2$  MMI couplers.  $\Delta L$  denotes the fixed path length difference between the two arms.

$$\begin{bmatrix} 1 & 0 \\ 0 & \exp^{j\beta\Delta L} \end{bmatrix}, \quad (2.42)$$

where

$$\beta\Delta L = \frac{2\pi n_g \Delta L}{\lambda}. \quad (2.43)$$

From equation 2.42 and assuming ideal 3 dB couplers, the transfer matrix for the AMZI device becomes:

$$\begin{bmatrix} E_3 \\ E_4 \end{bmatrix} = \frac{1}{2} \begin{bmatrix} (1 - \exp^{j\beta\Delta L}) & j(1 + \exp^{j\beta\Delta L}) \\ j(1 + \exp^{j\beta\Delta L}) & (-1 + \exp^{j\beta\Delta L}) \end{bmatrix} \begin{bmatrix} E_1 \\ E_2 \end{bmatrix}. \quad (2.44)$$

The output powers at the bar and cross of the AMZI can now be defined as being:

$$P_{bar} = \sin^2 \left( \frac{\beta\Delta L}{2} \right) \quad (2.45)$$

and

$$P_{cross} = \cos^2 \left( \frac{\beta\Delta L}{2} \right). \quad (2.46)$$

The output of the (de)multiplexer can now be simulated by assuming that light is launched at  $In_1$ . The simulation results are shown in Fig. 2.24 where  $\Delta L$  is chosen such that the channel spacing is 100 GHz or 0.8 nm. The wavelength channel spacing is defined as [82]:

$$\Delta\lambda = \lambda_1 - \lambda_2 = \frac{\lambda_1\lambda_2}{2n_g\Delta L}, \quad (2.47)$$

thus for a 0.8 nm channel spacing, knowing that  $n_g=3.55$ , the path length difference should be  $423 \mu\text{m}$ .

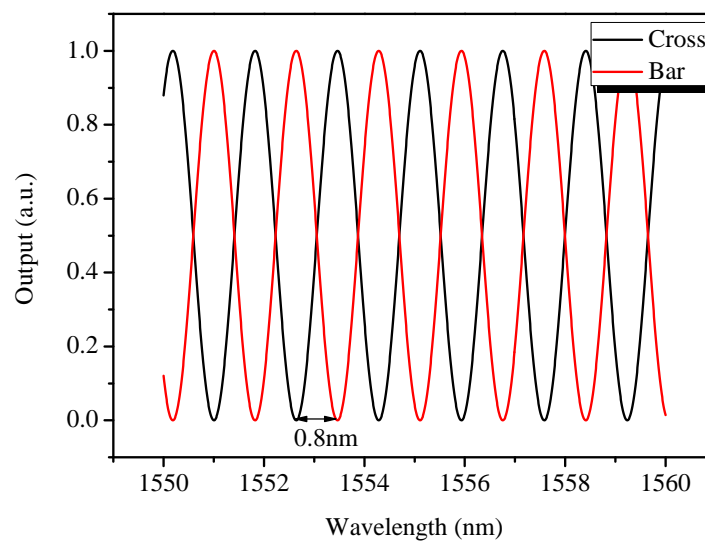


FIGURE 2.24: Simulated performance of an AMZI DWDM (de)multiplexer with  $\Delta L$  chosen to give a 100 GHz (0.8 nm) channel spacing.

## 2.6.2 OCDMA: AMZI Operation Principle as an OCDMA encoder/decoder

Two technical papers published in the 1980's kick started the serious development of optical code division multiple access (OCDMA) as it is known today. The first was written by Prucnal et al. and it showed that incoherent optical signal processing and pseudo orthogonal sequences, such as prime sequence codes [83], could be realised using fibre based tapped delay lines [15]. The second, by Weiner et al., demonstrated that coherent, short pulse, ultrawide bandwidth spectra could be produced and controlled in the phase or spectral domain [16]. These papers

proved that encoding and code correlation (decoding) could be implemented all optically, thus paved the way for a new generation of research into OCDMA for potential deployment in future digital all optical networks. They showed that the successful developments of pulse coding and spread spectrum techniques made in RF CDMA, such as resistance to detection and jamming, could be applied in the optical domain [17].

The basic operation of an OCDMA system relies upon the correlation process between the code sequences of the encoders and decoders. At the transmitter, each data bit is optically coded then transmitted asynchronously (with respect to the other users) over a common channel. At the receiver, the encoded signals are decoded with the original data being reconstructed only when the codes at the encoder and decoder match. While on the other hand, unmatched codes remain randomly spread over time after the decoding, appearing as noise. This methodology allows for multiple users to share the bandwidth and communicate simultaneously with the additional benefit of increased data security due to the presence of unique coding implementations.

OCDMA can generally be categorised into two main regimes, i.e. coherent and incoherent, depending on the correlation properties of the optical codes. In coherent OCDMA, the codes are applied via phase encoding of the optical signal on a field basis. The signal is typically produced by a highly coherent pulse source such as a mode-locked laser. In contrast, incoherent OCDMA applies amplitude modulation to the signal power with the receiver being based upon an incoherent decoding and recovery process [17]. It has been shown that coherent OCDMA exhibits many advantages over its incoherent counterpart in terms of autocorrelation value strength (suppression of side lobes caused by interference), code orthogonality and code length, thus enhancing signal to noise ratios and therefore system performance [84, 85]. OCDMA may also be differentiated in terms of the coding domain, i.e. spectral, as realised to great effect in [86], or temporal as utilised by several other groups [20, 84, 87, 88, 89]. In this work, we consider the coherent temporal phase coded (TPC) approach to OCDMA, as we also develop an ultrafast, coherent light source for monolithic integration.

Fig. 2.25 shows a schematic illustration of a monolithically integrated AMZI based 2-bit TPC-OCDMA encoder. When an optical pulse is input at  $In_1$ , the temporal phase encoder creates  $N$  pulse copies or chips (here  $N=2$ ), each of which is delayed by a fixed time introduced by the path length difference between the AMZI arms,

$\Delta L$ . The spacing between the chips is termed the *temporal chip interval*,  $T_c$ , and is given by:

$$T_c = \frac{n_g \Delta L}{c}. \quad (2.48)$$

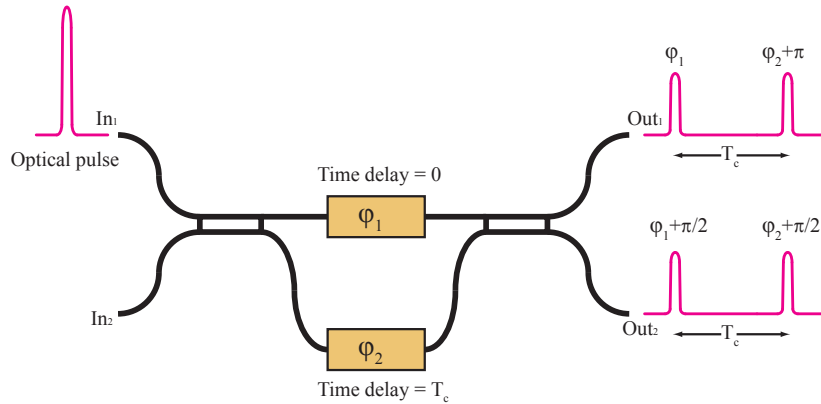


FIGURE 2.25: Schematic illustration of a 2-bit AMZI based temporal phase coded OCDMA encoder.

Each pulse copy is also assigned with a binary phase shift arising from the phase dependance of the MMI couplers and from the integrated phase shifting sections on the interferometer arms. Both the time delay and phase shifts form the particular users unique code ready for transmission. Here, the individual phase components are constructed from simple binary codes, i.e. 0 and  $\pi$ . The time and phase information of the code sequence are also shown at the outputs in Fig. 2.25.

At the receiver, in order to recover a given users coded data stream, a matched filtering technique is used. Fig. 2.26 shows such a decoder, primarily identical to the encoder. In order to decode the signal, both the time delay and relative phase shifts of the decoder must be identical to that of the encoder. The decoder spreads the received pulses in time again to make  $N$  pulse copies, applying the binary phase shifts to each. When the time delay and phase shifts match that of the encoder, a strong autocorrelation peak at the output is observed, i.e. the matched case. If the time delay or phase shifts do not match, then the operation represents a cross correlation between two differing codes hence the value is zero and the pulse is not reconstructed, i.e. the unmatched case [17, 70, 90].

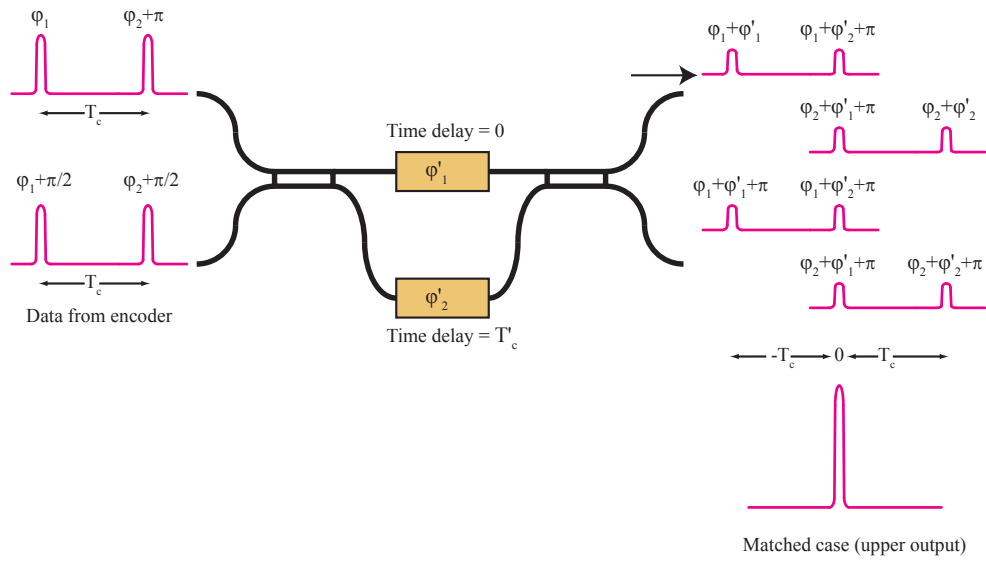


FIGURE 2.26: Schematic illustration of a 2-bit AMZI based temporal phase coded OCDMA decoder.

An important design parameter for the monolithically integrated AMZI based TPC-OCDMA encoder/decoder is the path length difference between the interferometric arms, which leads to the temporal chip interval. This chip interval must satisfy the condition that it is sufficiently larger than the pulse width duration, such that erroneous overlapping of pulses does not occur. If  $L_p$  is the number of pulses contained within a code word, it has been shown that the temporal correlation arriving at the receiver is equal to  $(2L_p - 1)T_1$ . In order to ensure that adjacent data bits correlation functions do not interfere, the data rate of the OCDMA system should thus be limited to  $1/(2L_p - 1)T_1$  [84].

As the pulse source tends to be a mode locked laser, which typically emits pulses in the range of 1-3 ps, the temporal chip interval should be chosen such that these pulses do not overlap. With this in mind, the interval is chosen here to be around 5 ps, coincidentally corresponding to the same path length difference from previously, i.e.  $\Delta L = 423 \mu\text{m}$ . Here, the number of pulses contained within the code word is 2, therefore the maximum data rate of this OCDMA system would be 65 Gbit/s.

## 2.7 Semiconductor Mode-Locked Lasers

Mode-locking is a commonly used resonant phenomenon that can be applied to lasers for the generation of high repetition rate, ultrashort optical pulse trains. Such pulse trains are required for various applications such as high speed optical telecommunications systems, radio over fibre communications systems and fast optical sampling oscilloscopes. Other methods exist for generating pulses from lasers, for example: *Q-switching*, whereby modulation of the intracavity losses (and thus the Q factor) of the laser results in the emission of short optical pulses that are many cavity roundtrips in duration, and *Gain switching* where the same effect is obtained by switching the carrier concentration in the device. However, due to the drastic changes in the carrier and photon intensities within the laser cavity during these switching processes, pulses tend to be broadened, incoherent and of poor quality [91]. In order to achieve the shortest, high quality pulses possible from laser diodes, mode-locking must be used [92]. Long wavelength (1550 nm) semiconductor mode-locked laser diodes have proven to be successful candidates for short pulse sources in high speed OTDM systems owing to several attractive features such as compactness, reliability, low timing jitter, direct electrical pumping ability, cost and the availability of a broad band of repetition rates [93, 94]. The first demonstration of short pulses (20 ps) from an AlGaAs based laser diode in 1978 paved the way for decades of research into reducing the pulse widths and improving the overall performance of the devices [95].

### 2.7.1 Mode-Locking Theory

In a typical semiconductor laser, such as a FP cavity based device, there exists a large number of optical frequency components that are determined by both the gain bandwidth of the material and the resonance condition, set by the cavity length, as shown in Fig. 2.27. These wavelength components, or longitudinal modes, are equally spaced in the frequency domain by:

$$\Delta f = \frac{c}{2n_g L}, \quad (2.49)$$

where  $L$  is the cavity length. This frequency spacing value,  $\Delta f$ , is also known as the free spectral range (FSR) of the cavity. It is also known that the relationship between frequency and wavelength is defined by:

$$f = \frac{c}{\lambda}, \quad (2.50)$$

therefore the mode spacing can also be defined in the wavelength domain. By differentiating equation 2.50 around a centre wavelength,  $\lambda_0$ , we obtain:

$$\Delta f = -\frac{c}{\lambda_0^2} \Delta \lambda. \quad (2.51)$$

Substituting equation 2.49 into 2.51 and rearranging yields:

$$\Delta \lambda = \frac{\lambda_0^2}{2n_g L}. \quad (2.52)$$

This relationship is valid as long as the wavelength spacing is small compared to the actual operational wavelength [9].

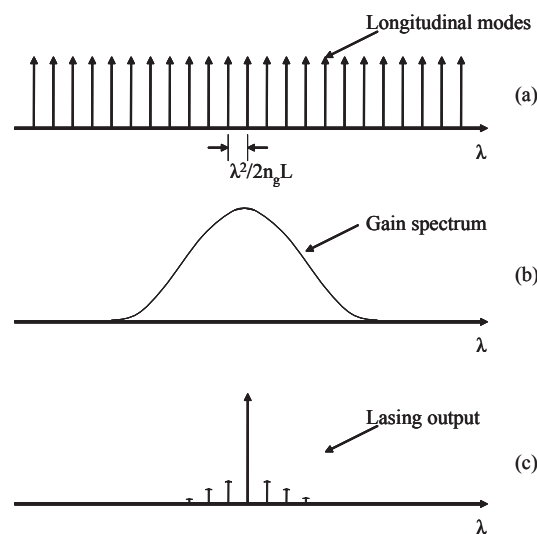


FIGURE 2.27: Graphical illustration of a FP lasers emission modes: (a) longitudinal resonant modes of the cavity of length  $L$ , (b) material gain spectrum and (c) resultant laser output.

The modes normally oscillate with random phases such that the free running laser output fluctuates randomly in time, as shown in Fig. 2.28 (a). This is known as continuous wave multi-mode operation. However, by enforcing coherence between

the phases of different modes, they begin to oscillate in tandem and add constructively such that the steady state output of the laser is a stream of optical bursts with a periodicity,  $T_R$ , equal to  $\frac{1}{\Delta f}$ , as illustrated in Fig. 2.28 (b).

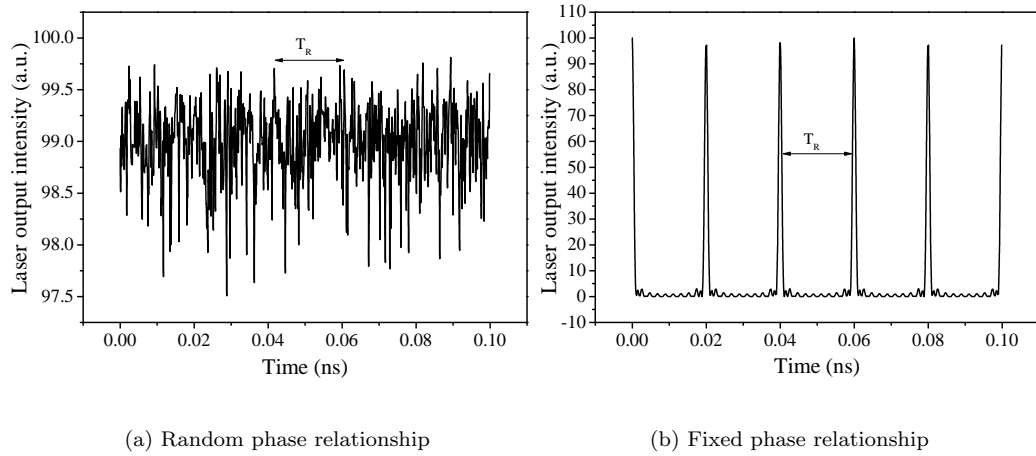


FIGURE 2.28: Laser temporal output with an (a) arbitrary, and (b) enforced coherence between the phases of different modes.

## 2.7.2 Mode-Locking Methods

Three techniques are generally available to induce mode-locking in semiconductor lasers, namely active, passive and hybrid mode-locking.

### 2.7.2.1 Active Mode-Locking

In active mode-locking the gain or loss of the laser is modulated at a frequency synchronised to the FSR of the cavity or at a harmonic thereof. This modulation is achieved by applying an external electrical signal to a modulation device, for example, an electro-absorption modulator, such that all of the longitudinal modes resonating within the cavity are intensity modulated at the FSR, and a constant phase relationship is established between them. This process can also be described in the time domain where the intensity modulator behaves as a weak shutter to the light resonating between the mirrors of the laser, absorbing the light when it is “closed” and passing the light when it is “open”. If the modulation rate is synchronised to the cavity round trip time, then a single pulse of light will oscillate back and forth within the cavity [96].

### 2.7.2.2 Passive Mode-Locking

The phase values of the modes may also be locked together more efficiently by introducing an intensity dependant loss element (as shown in upper schematic in Fig. 2.29) into the structure as the mode coupling mechanism. Typically in QW lasers, this non-linear element is an intracavity saturable absorber (SA), i.e. the absorption is intensity dependant. The interplay between this saturable absorption, gain saturation and carrier lifetimes in both the absorber and gain sections leads to the formation of a pulse traversing the laser cavity [97]. As there should be at least a single pulse every round trip time,  $T_R$ , it follows that the SA must be able to fully recover within that round trip time. However, even within that constraint there are two types of SA available for passive mode-locking, fast and slow. In a fast SA, the recovery time is fast compared to that of the pulse duration and the opposite is true for a slow SA. The theory of mode-locking using both fast and slow SAs has been described previously in great detail by Haus [98, 99]. In comparison with active mode-locking, passive mode-locking allows for the generation of narrower pulses, because the SA, driven by already very narrow pulses, can modulate the cavity losses much faster than any electronic modulator and the shorter the pulse becomes, the faster the loss modulation. Passive mode-locking is also advantageous in that no high speed electronics are required. However, this also leads to timing jitter and synchronisation issues.

For monolithically integrated passively mode-locked QW lasers, the SA recovery time tends to be greater than that of the gain section, therefore mode-locking is in the slow SA regime. At the start up of lasing, the modes of the laser are initially unlocked. However, because of the somewhat random intensity fluctuations experienced, any arbitrary high intensity spike will be transmitted preferentially by the SA. As the light in the cavity oscillates, this process repeats, leading to the selective amplification of the high intensity spike and the absorption of the low intensity light. Every time this spike traverses the SA it is reshaped such that it becomes narrower and of higher intensity until it reaches its shortest width, thus forming an ultrashort optical pulse. This can be described in the time domain as follows, with the aid of Fig. 2.29.

As the randomly formed pulse enters the SA, the leading edge experiences loss until such a time when the intensity of the pulse is suffice to begin saturation of the SA. At this point the net gain and loss are equal. As the intensity of the pulse

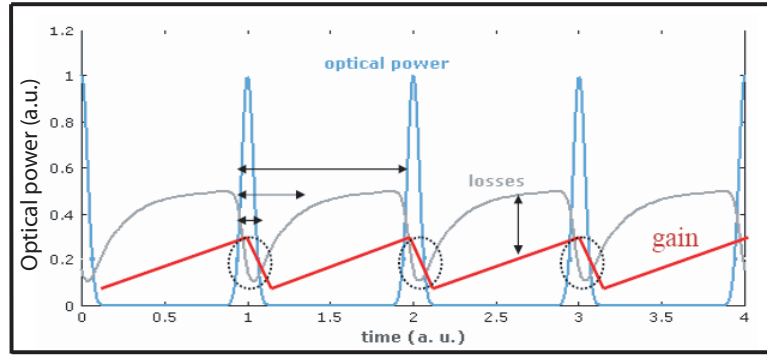


FIGURE 2.29: Temporal evolution of optical power, gain and losses in a passively mode-locked laser with a slow saturable absorber. The saturable absorber causes a loss modulation, which is fast for the leading edge of the pulse, whereas recovery of the absorber takes some longer time.

is increased, the SA is bleached such that the pulse experiences net gain, therefore is amplified. For this to happen, the loss has to saturate faster than the gain, i.e. the saturation energy of the absorber,  $E_a^{sat}$ , must be less than that of the gain section  $E_g^{sat}$ . This is the main requirement for mode-locking [100].

On the trailing edge of the pulse again comes the point when the gain and losses are equal. After this point the trailing edge shall experience loss in the SA. Negative net gain is required here to stop stimulated emission on the trailing edge of the pulse, thus the SA must recover faster than the gain section, i.e.  $\tau_g > \tau_a$ , where  $\tau_g$  and  $\tau_a$  are the carrier recovery times of the gain and absorber sections respectively. The loss will remain greater than the gain everywhere except for the peak region of the pulse. This requirement is known as New's background stability criterion [101]. However, stable mode-locked pulses have actually been found even with positive net gain at the leading edge of the pulse under certain operating conditions [102].

The first requirement,  $E_g^{sat} > E_a^{sat}$ , may be analysed further as it is known that the saturation energy of the gain or absorber section may be given by [103]:

$$E_{g,a}^{sat} = \frac{hfA_{g,a}}{d(g,a)/dN_{g,a}}, \quad (2.53)$$

where  $h$  is Planck's constant,  $f$  is the optical frequency,  $A_{g,a}$  is the cross sectional area of the laser mode and  $d(g,a)/dN_{g,a}$  is the differential gain or absorption. The condition may therefore be rewritten as:

$$\frac{hfA_g}{dg/dN_g} > \frac{hfA_a}{da/dN_a}. \quad (2.54)$$

This condition is satisfied in QW material due to the non-linear dependence of the gain on the carrier density, as shown in Fig. 2.30 [34, 104, 105]. Here it is known that the modal gain may be well approximated by the simple three parameter logarithmic formula (for  $g \geq 0$ ):

$$g = g_0 \ln \left( \frac{N}{N_{tr}} \right), \quad (2.55)$$

where  $g_0$  is the optimum gain point,  $N$  is the carrier density and  $N_{tr}$  is the transparency carrier density. The larger differential gain in the absorber section (lower carrier density) compared with the smaller differential gain in the gain section (higher carrier density) ensures that the requirement is met. The reduction in differential gain with increased carrier density is particularly large in QW lasers due to the step-like density of states characteristic [35].

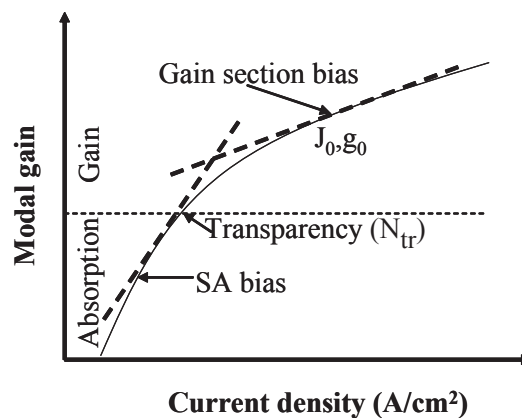


FIGURE 2.30: Schematic illustration of the modal gain (or absorption) versus current density for QW material. The dashes lines represent the differential gain/absorption.

The relaxation time of QW SAs tends to be around 1 ns, too long for most mode-locking applications, where the cavity round trip time is of the order of several ps. In order to reduce the absorption recovery time in the SA, one must employ various methods such that  $\tau_g > \tau_a$  is achievable. Proton or ion bombardment has been used to introduce defects into the semiconductor lattice reducing the recovery time, with thermal annealing being used to somewhat retain the non-linear properties. This method is commonly used in the realisation of semiconductor saturable absorber

mirror (SESAM) lasers [106]. However, for monolithic devices, by the utilisation of split contacts, a reverse bias voltage may be applied across the absorber, thus increasing the absorption due to the QCSE. The electric field produced by the applied voltage sweeps out the generated carriers from the absorber region more quickly, therefore decreases the absorption recovery time. As no damage is induced in the material, the technique is thought to be more reliable and is now commonly used in the fabrication of monolithic semiconductor mode-locked lasers.

### 2.7.2.3 Hybrid Mode-Locking

Hybrid mode-locking may be considered as a combination of both active and passive mode-locking, wherein the optical pulses are generated in the same way as in a passively mode-locked laser, but the pulses are synchronised by means of an external electrical signal applied to the absorber [107, 108], or by the injection of subharmonic repetition rate optical pulse trains from an actively mode-locked laser [109]. Benefits here include the possibility to control the pulse timing externally, as in an actively mode-locked laser, whilst achieving shorter pulse durations, as in a passively mode-locked device. There is also associated timing jitter reductions, even with subharmonic modulation.

## 2.7.3 Pulse Duration and Spectral Width

When discussing pulse durations and spectral widths, the full width half maximum (FWHM) of the intensity profiles is normally used, as shown in Fig. 2.31 for the temporal width case. Due to the difficulty in determining the exact pulse shape, it is usually approximated with either a Gaussian, Lorentzian or  $\text{sech}^2$  distribution, depending on which provides the best fit [110]. Normally, one would desire the shortest pulse width possible, i.e. a Fourier transform limited pulse, that is a pulse which exhibits the narrowest FWHM temporal width possible for a given spectral width. As the temporal and spectral characteristics of the EM field are related via Fourier transforms, the pulse width and spectral bandwidth cannot vary independently of one and other. Thus, it follows that in order to produce narrow optical pulses, many modes have to be locked over a large optical bandwidth as the pulse width is inversely proportional to the locked optical bandwidth [100].

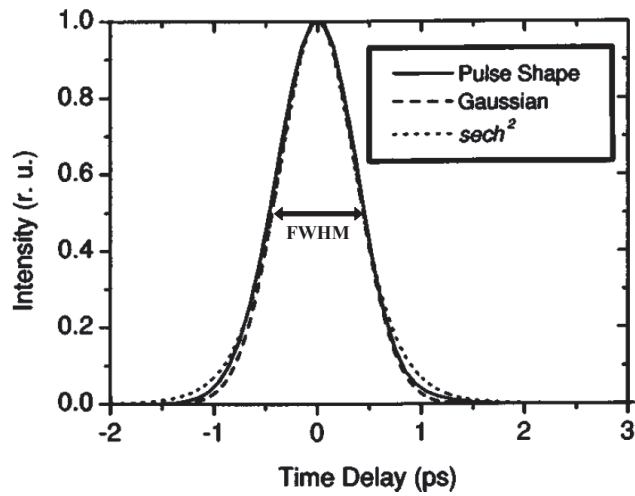


FIGURE 2.31: Definition of pulse shape using Gaussian and  $\text{sech}^2$  fitting (courtesy of [111]).

Depending on which type of curve fitting is used, the theoretical pulse width of a transform limited pulse can be calculated using the time bandwidth product (TBP), defined as:

$$TBP = \Delta\nu \cdot \Delta\tau, \quad (2.56)$$

where  $\Delta\nu$  is the spectral bandwidth of the locked modes and  $\Delta\tau$  is the FWHM pulse width. For Gaussian shaped pulses, the transform limited TBP is  $\sim 0.441$ ,  $\sim 0.315$  for  $\text{sech}^2$  shaped pulses and  $\sim 0.142$  for a Lorentzian. However, when a transform limited pulse propagates in a dielectric waveguide its TBP may increase due to chromatic dispersion and/or other non-linearities within the medium such as self phase modulation (SPM). Chromatic dispersion, also known as group velocity dispersion (GVD), is the phenomenon by which different spectral components of the pulse travel at different velocities such that they reach the output facet at different times, hence the pulse becomes wider. Dispersion also imposes chirp on the pulse, i.e. the instantaneous frequency of the pulse in the time domain is varying such that the pulse is spread in time. The pulse width may only reach a minimum value, i.e. the transform limit, and be unchirped when dispersion is absent in the mode-locking system. The physical mechanism behind SPM is gain saturation, which leads to intensity dependent changes in the refractive index in response to variations in the carrier density. The effect of SPM in the pulsed regime is also to impose chirp on the pulses. If the dispersion is positive, then the SPM of

the gain and absorber sections causes serious chirp, which increases with increasing SPM. For negative dispersion, almost no chirp is induced as it is compensated by the chirp caused by the gain and absorber sections, thus the presence of both dispersion and SPM do not necessarily have a detrimental impact on the quality of the mode-locking[112]. Nevertheless, chirped pulses may be compressed back to, or near to, the transform limit by use of pulse dispersion compensation techniques, for example, integrated chirped Bragg gratings, as demonstrated in [113].

Bandelow and Kaiser carried out a thorough theoretical and experimental investigation of 40 GHz monolithic mode-locked lasers applicable to high speed OTDM systems, wherein it was found that some of the important performance parameters of the lasers are [93, 114]:

- Pulse width ( $\leq 1.6$  ps is generally regarded to be required for high speed applications to avoid any inter symbol interference).
- RF spectrum ER ( $\geq 25$  dB).

As a quality measure, the devices produced in this work were measured against these parameters and reported accordingly.

#### **2.7.4 Semiconductor Ring Lasers**

Since the first demonstration of a truly ring shaped waveguide laser resonator in 1980 [115], semiconductor ring laser (SRL)s have been the focus of increased interest in the PIC domain. They exhibit several advantages over their FP counterpart, for example, they do not require cleaved mirror facets or gratings for optical feedback, thus are highly suitable for monolithic integration. Also, as they operate in the traveling wave regime (as opposed to the standing wave regime in FP devices), they support two counter propagating longitudinal modes wherein the gain competition between these two may lead to stable unidirectional operation, where only one of the directions is maintained, while the other becomes highly suppressed. In this situation, the SRL may behave as an optical bistable device since the lasing direction can be selected or switched by external optical injection. This property has created a lot of interest in SRLs for applications such as all optical signal processing and optical memory [116, 117]. Additionally, in

the unidirectional regime, there is no standing wave interference pattern in the laser gain medium and thus no spatial hole burning, therefore single frequency operation can be readily achieved.

#### 2.7.4.1 Evanescent Field Couplers

An important design feature of a SRL is the output coupler, which allows extraction of light from the otherwise enclosed ring cavity. The coupler also has a profound effect on the performance of the device. Several studies have reported on the benefits and limitations of various coupler types such as MMI, evanescent field and Y-junction [118, 119]. In this work, evanescent field couplers were chosen over other couplers for the ring lasers due to several advantages. Firstly, any type of back reflection will strongly affect the SRL behavior and the ring is known to be least perturbed using evanescent field couplers, as simulated in [56]. Next, arbitrary coupling ratios are more easily achievable with evanescent couplers than with MMIs or Y-junctions and they may also be tuned using electro-optic effects. A limitation, nevertheless, is that evanescent field couplers are more susceptible to fabrication tolerances, this may be negated however by use of the dry etching control measures that shall be discussed in the following chapter.

Evanescent field couplers (also referred to as directional couplers) typically consist of two parallel waveguides that are sufficiently close such that the waveguide modes may overlap, as shown in Fig. 2.32. This overlapping results in the periodic transfer of energy from one guide to another as the light propagates along the guide. If the waveguides are identical, such that the light waves propagating in both guides have the same velocity and propagation vector, then the power propagating in the  $z$  direction in the two guides is given by:

$$P_1(z) = \cos^2(Kz) \exp^{-\alpha z}, \quad (2.57)$$

and

$$P_2(z) = \sin^2(Kz) \exp^{-\alpha z}, \quad (2.58)$$

where  $\alpha$  is the waveguide loss coefficient and  $K$  is the coupling constant defined as:

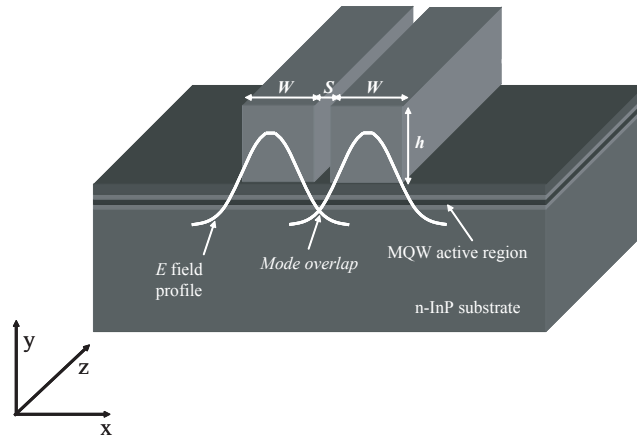


FIGURE 2.32: Schematic cross section of evanescent field coupler showing the overlap of the E-field between the modes.

$$K = \left( \frac{2\beta_y^2 b \exp^{-bs}}{\beta_z W (\beta_y^2 + \beta_z^2)} \right), \quad (2.59)$$

with  $b$  being the extinction coefficient,  $s$  the distance between the waveguides,  $W$  the width of the guides and  $\beta_y^2$  and  $\beta_z^2$  the propagation constants in the  $y$  and  $z$  directions respectively [31].

However, in real couplers, the two waveguides may not be exactly identical, and thus there may exist a small discrepancy in the propagation constant,  $\Delta\beta_z$ . The amended coupling constant is then given by:

$$K_a^2 = K^2 + \left( \frac{\Delta\beta_z}{2} \right)^2. \quad (2.60)$$

In more complex structures than coupled slab waveguides, the numerical solution becomes more arduous. In this case a 3-D BPM simulation may be used in order to analyse the couplers. The 100% coupling length versus the coupler gap width was simulated for single-mode waveguides in the AlGaInAs MWQ material, with the results shown in Fig. 2.33.

From the plot it is evident that for strong coupling with small coupling lengths, the gap width has to be very small. This is fine in theory, however, may cause fabrication issues due to such phenomena as reactive ion etching (RIE) lag, which shall be discussed in Chapter 3. To this end, an 800 nm gap width was chosen, giving 100% coupling at a length of  $560\mu\text{m}$ . However, as coupling 100% of the

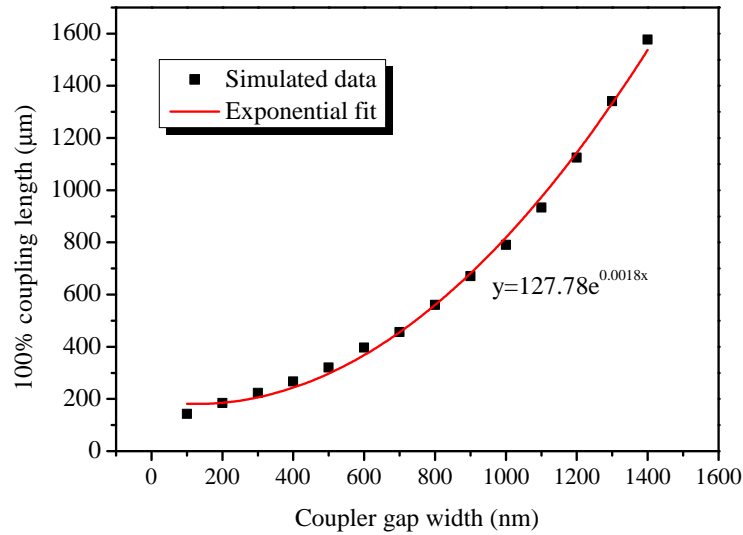


FIGURE 2.33: 100% coupling length versus gap width for  $2\ \mu\text{m}$  wide,  $1920\ \text{nm}$  deep waveguides.

light from the ring would not allow for lasing, a coupler length of  $300\ \mu\text{m}$  is chosen, giving a relatively strong outcoupling value of around 50%, as shown in Fig. 2.34.

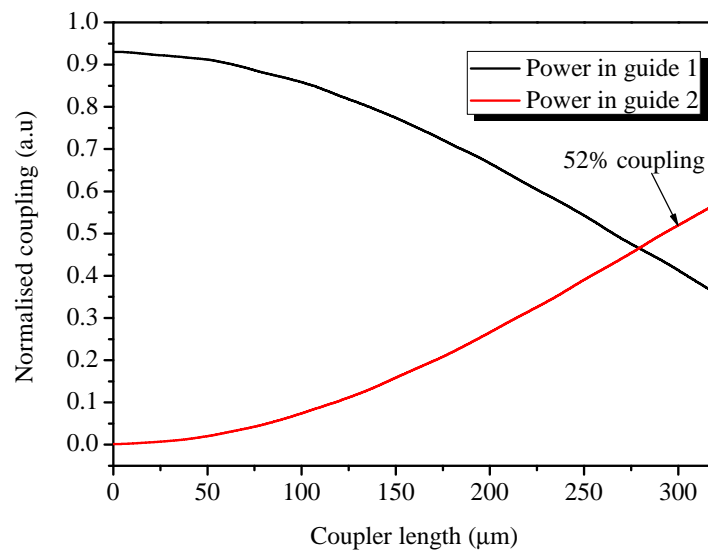


FIGURE 2.34: 3-D BPM simulation of  $300\ \mu\text{m}$  long coupler with  $800\ \text{nm}$  gap width between the guides.

### 2.7.4.2 Mode-Locking in Semiconductor Ring Lasers

Mode-locking can also be applied to SRLs, with the first experimental demonstration of passive mode-locking by Hohimer in 1993 producing 1.3 ps, transform limited pulses at a repetition rate of 86 GHz [120]. Here, a rib waveguide ring of radius  $150\mu\text{m}$  was formed in a single QW, 874 nm GaAs-AlGaAs structure employing a  $50\mu\text{m}$  SA as the mode-locking element, with a Y-junction coupler used to extract the light from the cavity. Unfortunately no RF measurements were made on the device. Later, a thorough experimental and theoretical study of “large” ring lasers was undertaken in 1998 by Yu et al. at the University of Glasgow [26]. It became clear that as the device is inherently a CPM structure, the interaction between the counter propagating pulses, the relative positions of the gain section, the SA and the output coupler(s) play a major part in the mode-locking performance of the laser. For example, the effect of enforcing pulse collisions in the absorber and not in the gain section is that the peak pulse power required to saturate the absorber decreases, therefore the process is more efficient and the pulse energy loss is minimised. This may be understood by the description of Koumans and van Roijen, where it is predicted that the coherent interaction of the pulses in the absorber leads to a transient standing wave pattern in the optical field and causes a periodic saturation modulation in the absorber. Carrier generation is high at the peak of the standing wave and low at the nulls, thus forming an effective absorption grating. It is proposed that the grating becomes more transparent as the pulses collide, leading to a reduction in the absorber saturation power. It has also been noted that the symmetry of the cavity is vital as any asymmetry in the gain for the two paths leads to different pulse energies and strongly reduces the stability of the CPM [97, 112]. Yu also predicted, through theoretical modeling, that devices with dual absorbers should lead to a larger, more stable mode-locking region with shorter pulses as a result of the double pulse narrowing effect, and the complete symmetry of the device, i.e. no pulse collisions in the gain section.

Further investigations in passively mode-locked ring lasers were undertaken by Barbarin et al., who demonstrated 1 ps pulses at 27 GHz from an extended cavity devices fabricated using the butt-joint coupling active/passive integration technique (described in the following chapter) [121]. However, it was found that the mode-locking region was very small, mainly attributed to intracavity reflections from the aforementioned active/passive interfaces. The same author also presented the characterisation of 15 GHz bulk GaInAsP devices operating at 1530 nm

[122, 123]. The design included a  $200\mu\text{m}$  long evanescent field coupler and a single SA varying in length from  $30\text{-}60\mu\text{m}$ . A stable mode-locking regime was reported, but the pulse widths were rather wide (4-7 ps), thought to be due to either the inherent dispersion of the fibres employed in the set-up and/or chirp in the pulses from the device itself. The most recent work in passively mode-locked rings was by Heck et al. in the realisation of 5 GHz quantum-dot rings [124]. The main findings here were a reduction in the 3 dB RF linewidth and timing jitter, as well as an increase in the RF stability when compared to FP devices fabricated on the same material. It is thought that these benefits are attributed to the relatively weak out coupling from the ring and/or the fact that the device is inherently operating in the colliding pulse regime. Also, it was observed that each of the propagation directions emit at a slightly different wavelength, a unique consequence of the quantum-dots. The measured pulse duration was rather long however, around 55 ps.

In this research work, 36 GHz devices were designed for use in optical telecommunications systems. Nominally, the repetition frequency would be designed for 40 GHz operation, however, due to the bandwidth limitation of the available RF spectrum analyser, the frequency is lowered slightly such that it can be clearly measured. Nevertheless, variations in repetition frequency are readily obtainable with slight modifications in the cavity length design. As the evanescent couplers require a straight waveguide section, the lasers are designed in a racetrack type cavity with dual SAs and dual couplers allowing for multiple laser outputs. The chosen SA lengths are 1% and 2.5% of the total cavity length, with  $20\mu\text{m}$  separation regions between them and the gain section contact for electrical isolation. The lengths were chosen as a result of theoretical simulations by the author's colleague using the traveling wave model as defined in [125]. This allows for the assessment of 1%, 2%, 2.5% and 5% total absorber lengths, depending on the biasing conditions, as well as a comparison between single and dual absorbers. In the case when only a single absorber is biased, the other is forward biased in line with the rest of the gain section.

As the FSR of a ring cavity is equal to:

$$\Delta f = \frac{c}{n_g L}, \quad (2.61)$$

the total cavity length for 36 GHz is designed to be  $2297\mu\text{m}$  long, using a group index,  $n_g$ , value of 3.55. The curved sections are of radius  $250\mu\text{m}$  in order to maintain a balance between low curved waveguide radiation losses and device size. To decrease any possible optical feedback from the cleaved facets, the output waveguides are inclined at  $10^\circ$  to the cleaved mirror edge. To ease fibre coupling the waveguides are linearly up-tapered from  $2\mu\text{m}$  to  $12\mu\text{m}$ . Each output waveguide also has a p-type contact acting as either an integrated photodetector or amplifier, or to provide further reductions in back reflections, if required, when reverse biased. Fig. 2.35 details the device configuration.

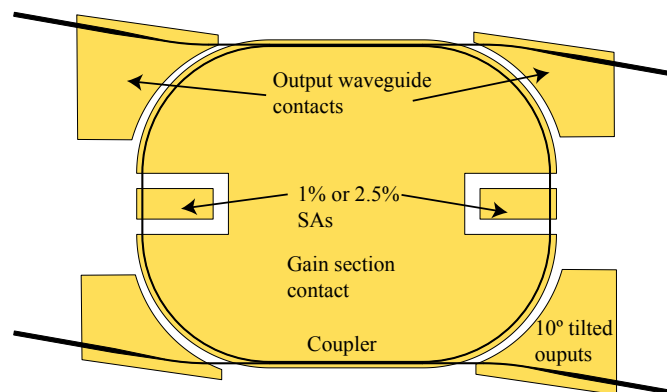


FIGURE 2.35: Schematic illustration of the mode-locked devices.

## 2.8 Integrated Devices

Photonic integrated circuits may address the issue of expensive OEO conversions between components in optical networks, thus leading to reductions in cost and power consumption, and improvements in reliability. In this work, we report on the investigation of integrating mode-locked SRLs with MZIs in order to perform some functionality typically delivered only by discrete components.

### 2.8.1 Monolithically Integrated OCDMA Transmitter

This device sees the integration of a 36 GHz mode-locked SRL with an AMZI. Here, the laser acts as a data source for a demonstrator chip for OCDMA applications. In order to reduce direct band-gap absorption in the phase shifting sections they must

be band-gap shifted from the as-grown wavelength, as will be discussed further in great detail in Chapter 3.

## 2.9 Chapter Summary

In this chapter the basic background theory and design of components constituting the photonic integrated circuits in this thesis were considered. The chapter began by introducing the AlGaInAs MQW material system, suitable for use in optical telecommunications network devices operating at 1550 nm, highlighting some advantages over the more mature GaInAsP system, such as improved gain and temperature performance. Next, the electro-optic properties of such materials were reviewed in order to fully understand the mechanisms involved in the functionality of many integrated optical devices. Effects based on both applied electric field and carrier injection were discussed, focusing mainly on the carrier induced effects as they are of most relevance to the devices in this thesis. A figure of merit was then introduced, the chirp parameter,  $\rho$ , allowing for the efficient design of electro-optic based devices by minimising losses and maximising phase shift efficiency.

Some general theory on the physical geometrical structures employed in the devices was then presented. BPM and mode solver simulations were performed in order to design both straight and curved low loss single-mode waveguides, where it was found that a  $2\ \mu\text{m}$  wide, 1920 nm deep guide of minimum bend radius  $200\ \mu\text{m}$  incurred negligible radiation losses. MMI couplers were then covered as they are essential components in the realisation of MZIs, one of the main constituents of this research work. The operating principles and theoretical analysis of these interferometric devices were then discussed and designs implemented in order to apply them to several optical multiple access schemes, namely OTDM, DWDM and OCDMA.

An ultrashort optical pulse generation technique, vital for high speed optical telecommunications, was then reviewed: mode-locking. Some elemental theory and methods were presented in terms of FP semiconductor lasers, moving onto an interesting breed of devices based on ring cavities. Such devices are attractive for monolithic integration purposes as they do not require cleaved mirrored facets.

Also, as the cavity length, and thus the repetition frequency, is defined lithographically, precise cleaving requirements for accurate pulse rates are negated. Finally, a completely monolithically integrated device was discussed i.e. a mode-locked semiconductor ring lasers and asymmetric MZIs for use as an OCDMA transmitter.

# Chapter 3

## Fabrication Technology and Material Characterisation

### 3.1 Introduction

In this chapter, the fabrication technology and material characterisation techniques are considered in order to assess and validate them in terms of realising the devices detailed in the previous chapter. It begins by introducing a vital technological requirement in the fabrication of monolithically integrated photonic circuits: active/passive integration, discussing the advantages and disadvantages of several available platforms.

Next, the key steps used in the fabrication process are presented, with specific emphasis on the critical processes where development work was undertaken, for example, dry etching. Subsequent sections focus on basic characterisation of the AlGaInAs material, such as the electro-optic effects, as well as the fabrication of simple devices enabling confirmation of the quality of the material itself and the fabrication processes.

The chapter concludes by detailing the activity undertaken in the development of antireflection coatings for use in the fabricated devices.

## 3.2 Active/Passive Integration

In order to produce highly functional, monolithically integrated photonic circuits, both active and passive elements must be realised on the same chip. For example, if a laser is to be integrated with a waveguide coupler leading to another device, then in most cases the waveguide losses in the coupler would be so high, due to direct band-gap absorption, that the photonic circuit would not perform. Ideally, to realise low losses, the band-gap of the coupler would be higher than that of the laser such that absorption losses would become negligible, leading to a reduction in waveguide losses in the coupler section (ideally  $<1 \text{ dBcm}^{-1}$ , but in some cases  $<10 \text{ dBcm}^{-1}$  is acceptable) [126].

This necessity poses several issues as active and passive material structures are inherently different, making it difficult to combine them on a single substrate without compromising their individual performance. Nevertheless, several techniques have been developed in order to circumvent this issue. One of these, the butt-joint coupling technique, employs the selective removal of waveguide material followed by the regrowth of a different waveguide material in order to combine them both on the same wafer [127]. A drawback of this technology is that precise material etching is required, as well as the need for a second expensive epitaxial growth stage that has tight tolerances on composition and thickness. Also, at the active/passive interfaces, losses and reflections are likely, leading to potential limitations in device performance.

Another process involves the selective area growth (SAG) of the epilayers by use of a pre-defined mask on the substrate. Here, the layers only grow where the mask pattern defines, allowing for a variation in the band-gap structure across the substrate [128]. However, as the growth rate varies as a function of the patterning geometry across the substrate, problems may arise in the optimisation of the optical confinement at certain regions, leading to compromises in chip functionality [28].

Offset QWs have also been used as an integration platform, wherein the well layers are grown above the waveguiding layers and selectively etched in order to form active/passive interfaces [129]. A limitation of this technique is the scope for only two band-gap regimes, restricting the diversity of devices readily achievable.

The asymmetric twin waveguide approach entails the growth of two vertically stacked, strongly coupled waveguides separated by a cladding layer. The asymmetry emanates from the refractive index difference between the active and passive waveguides, leading to an asymmetry between the two super modes [130]. This technique has been employed to promising effect, for example, in the monolithically integrated MZI device detailed previously [78]. However, as with offset QWs, chip complexity is limited by only two available band-gap regions. Also, complex taper designs and fabrication steps are required in order to couple light between the active and passive waveguides.

### 3.2.1 Quantum-Well Intermixing

An alternative approach to the aforementioned active/passive integration platforms is quantum-well intermixing (QWI), a post growth technique wherein, as the name suggests, the atoms of the well material are intermixed with those of the surrounding barrier material, such that a spatial modification of the band-gap energy transpires [126]. The process allows for greater flexibility on pattern shapes and number of band-gaps compared to the methods described previously, and also has associated cost and simplicity benefits due to the requirement of only one epitaxial growth stage. However, disadvantages of this technology include reliability issues, doping in the material and limited spatial resolution. Several variations in QWI processing techniques exist and have been successfully applied in the realisation of many photonic devices.

#### 3.2.1.1 Impurity Induced Vacancy Disordering

One approach, impurity induced vacancy disordering, introduces impurities into the QW structure such that, upon thermal excitation, interdiffusion occurs leading to an alteration of the band-gap energy [131]. It is believed that the role of the impurities in the disordering process is the generation of free carriers, increasing the equilibrium number of vacancies at the annealing temperature. However, as the impurity species employed are typically electrically active (for example Si or Zn), the electrical performance of the device may be compromised and there may also be an increase in waveguide propagation losses, mainly due to free carrier absorption mechanisms [126].

### 3.2.1.2 Photo Absorption Induced Disorder

By irradiating the active region of QW structures with a suitably high powered continuous wave laser, the local carrier density can be dramatically increased through band to band absorption of the photons. Subsequent carrier cooling and non-radiative recombination result in the generation of phonons in the crystal lattice, i.e. heat, causing thermal interdiffusion of atoms between the well and barrier materials. This technique is known as photo absorption induced disorder (PAID) and has been used to successfully achieve selective intermixing in several photonic devices [132, 133]. However, as the technique is based entirely on thermal diffusion, the spatial resolution performance tends to be rather poor.

### 3.2.1.3 Sputtering Induced Vacancy Disorder

The technique of choice in this research work is based on the approach detailed by Marsh [126] and further developed by Kowalski et al. at the University of Glasgow [134]. Sputtering (described in more detail later) induced vacancy disordering relies upon the generation of point defects in the crystal lattice. Intermixing is also induced by means of the out diffusion of Ga atoms from the III-V material into a dielectric film, particularly SiO<sub>2</sub>, deposited on the sample surface. For monolithic integration, spatial control over the band-gap shift is required in order to realise passive components, thus this method employs dielectric layers that both enhance the Ga out diffusion process, and films that suppress it (depending on the deposition method). Upon exposure to high temperature annealing for QWI enhancing films, there is an increase in Ga vacancies close to the semiconductor surface, which then thermally diffuse into the active region during the anneal stage and promote interdiffusion between the well and barrier atoms. This in turn leads to a change in the energy band profiles of the wells and barriers as shown in Fig. 3.1. In this case, QWI enhancement is achieved through use of a 200 nm thick layer of sputtered SiO<sub>2</sub> deposited on the sample surface along with minute amounts of Cu, which were found to improve the band-gap shift achievable [135]. Cu is known to diffuse interstitially and move onto group III lattice sites through the “kick out” mechanism. Because of its faster diffusion, Cu is much more efficient than many other impurities in generating point defects, and thus enhances QWI. To preserve the as-grown band-gap profile, a layer of PECVD SiO<sub>2</sub> is deposited,

which suppresses the out diffusion of Ga atoms and thus limits the QWI shift in the underlying semiconductor.

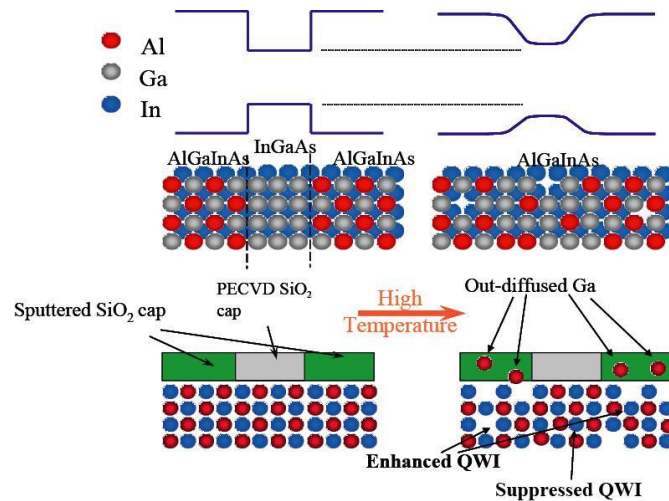


FIGURE 3.1: Schematic representation of the physical interactions occurring in sputtering induced vacancy disordering quantum-well intermixing.

In order to assess the effects of intermixing on the AlGaInAs material, samples were patterned using electron-beam lithography (EBL) (described in section 3.3 to define the active and passive regions. A 200 nm thick sputtered SiO<sub>2</sub> film was then deposited on the samples with the unwanted SiO<sub>2</sub> being lifted off by immersing the sample in hot Acetone at 40 °C. After further cleaning in Acetone and Isopropyl alcohol, the samples were coated with a further 200 nm of PECVD deposited SiO<sub>2</sub>. Annealing at temperatures in the range from 625-675 °C for 60 s in a rapid thermal annealer (RTA), wherein the samples were placed between two Si substrates to prevent desorption of the group V elements (As, P), completed the processing.

The induced band-gap (wavelength) shifts of both the sputtered and PECVD capped samples were measured using photoluminescence spectroscopy (PL). Here, the sample is irradiated with laser light at a lower wavelength (wider band-gap) than that of the QW material such that direct band-gap absorption occurs, exciting electrons from the valence to the conduction band. Some of these electrons are trapped by the QWs in the conduction band, as are the holes in the valence band. These carriers then relax to the band edge to recombine, emitting photons of energy equal to that of the effective band-gap of the QWs [43]. The PL set-up used, consisting of a 1064 nm Nd:YAG laser, a 20 X objective lens, an optical fibre coupler and an optical spectrum analyser (OSA), is detailed schematically in Fig. 3.2. The measurements were taken at 77 K using liquid N<sub>2</sub> in order to lower

the rate of non-radiative recombination, allowing for more efficient emission and thus clearer spectra.

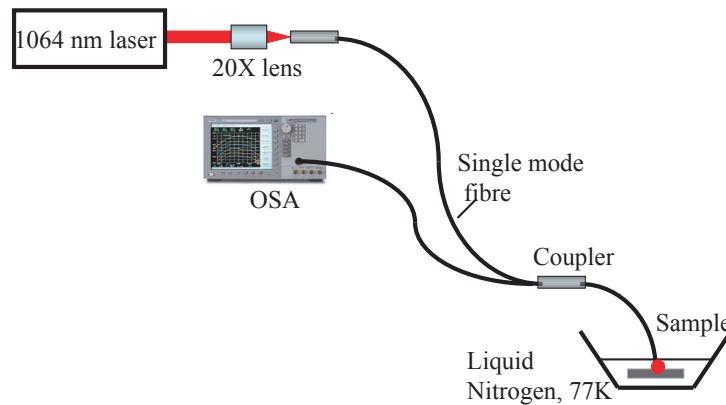


FIGURE 3.2: Schematic of the PL set-up as used in the measurements of the induced band-gap shifts of the AlGaInAs MQW material.

Fig. 3.3 shows the measured PL spectra as a function of anneal temperature for the sputtered silica capped samples. As expected, when the anneal temperature increases, so too does the blue shift in wavelength. Note that the PL intensity also decreases as the anneal temperature increases. It is postulated that this is caused by a combination of effects, the largest being thought to be the presence of a higher density of defects in the active region, providing additional non-radiative recombination centres. A smaller effect may be caused by the change in energy (shape of the QW) and compositional profile of the QW, i.e. the well will be more shallow and less able to trap carriers, so it is more likely that the carriers will recombine non-radiatively and in different layers. The 77 K PL wavelength of the as-grown material is much lower than that of the room temperature emission wavelength of the wells. This is due to the fact that the band-gap decreases with increasing temperature, basically the crystal expands slightly, therefore the atoms are (on average) further apart and thus their interaction (which leads to the band-gap energy) is reduced.

In order to clearly assess the actual wavelength shift values, the spectra in Fig. 3.3 were normalised to that of the as-grown spectrum. The results are shown in Fig. 3.4. Another way of viewing the results is to plot the actual wavelength shift from the as-grown PL peak as a function of anneal temperature, as in Fig. 3.5, for both the sputtered and PECVD capped samples. From this plot it can be seen that there are negligible wavelength shifts for the samples covered with PECVD SiO<sub>2</sub>. These results show that the technique is suitable for photonic integration

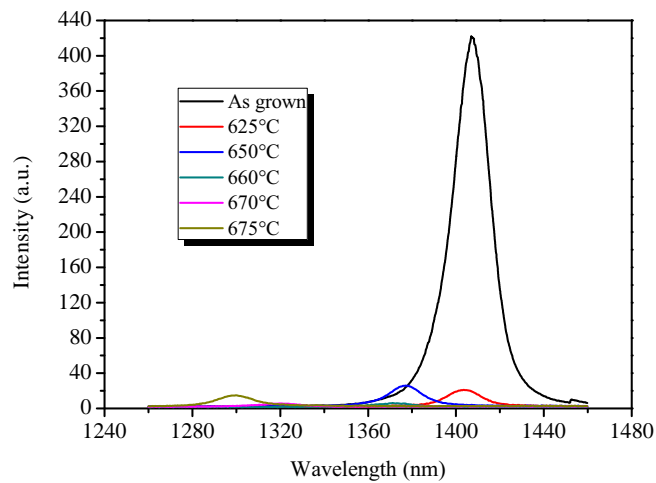


FIGURE 3.3: Measured PL spectra versus anneal temperature.

where passive sections may be realised by simply increasing the band-gap energy in that region.

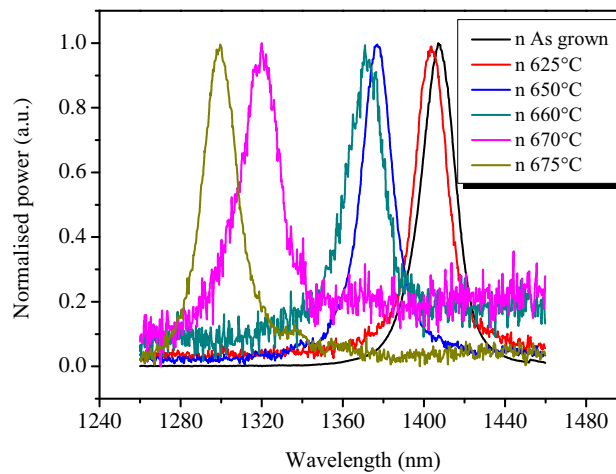


FIGURE 3.4: Measured PL spectra versus anneal temperature (n denotes normalised).

#### 3.2.1.4 Selected Intermixing in Selected Areas

The intermixing technique described above demonstrates the basic ability to define both active and passive sections on a single chip, i.e. a dual band-gap process. However, more complex monolithically integrated chips may consist of multiple

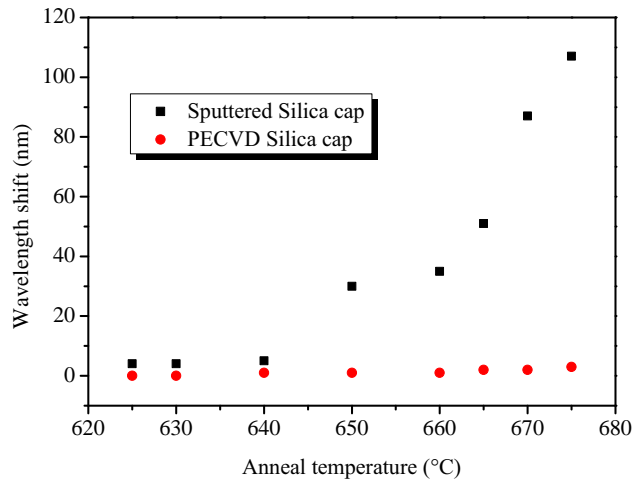


FIGURE 3.5: Measured PL peak wavelength shifts as a function of anneal temperature.

elements requiring several band-gap shifts. For example, passive waveguide interconnects would require a large shift to minimise losses, whilst phase shifters and tunable DBRs usually require a smaller band-gap shift in order to preserve the electro-optic effects. A technique known as selected intermixing in selected areas (SISA) allows for varying degrees of band-gap energy shift to transpire spatially across the substrate [136]. In this technique, lithography (EBL or optical) combined with lift-off processing is used to define various fill factor ratios of sputtered  $\text{SiO}_2$  to PECVD  $\text{SiO}_2$  in order to achieve varying degrees of intermixing and suppression using a single high temperature anneal step. To assess this method, a sample of the AlGaInAs material was patterned with lines and spaces using EBL in order to define SISA features. The chosen sputtered  $\text{SiO}_2$  linewidth was  $3\ \mu\text{m}$  to facilitate ease of lift-off, with the period between each line being varied in order to alter the fill factor ratio from 0 to 100%. The sample was then annealed at  $675\ ^\circ\text{C}$  and the wavelength blue shifts measured using the PL procedure described previously. The measured shifts as a function of sputtered silica fill factor are presented in Fig. 3.6.

It is evident from the measured PL data that using only a single anneal step, several band-gap energy values may be realised on a single chip. For the work described here, the SISA process is vital in order to realise active devices, such as the mode-locked ring lasers, passive devices, such as the low loss interconnects and intermediate band-gap devices, such as the phase shifters.

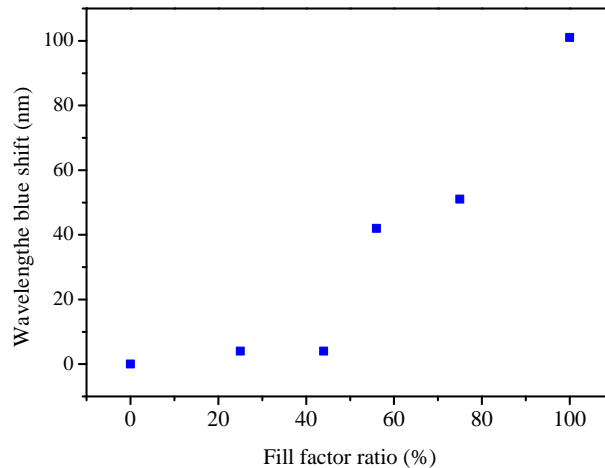


FIGURE 3.6: SISA PL wavelength shifts as a function of sputtered SiO<sub>2</sub> fill factor, annealed at 675 °C.

### 3.3 Patterning using Electron Beam Lithography

A vital step in any semiconductor micro/nano semiconductor fabrication process is the patterning of the chip, ready for further processing. A mainstay of such processing in industry, mainly due to its massive wafer throughput ability, is photolithography using optical steppers. However, this technique has limitations in the writable feature sizes due to the wavelength of the light used, which is typically in the wavelength range of 200-500 nm. Many research activities are focused on how to improve the critical dimensions achievable using optical lithography by means of complex lenses and different light sources. However, for high levels of pattern flexibility, required for device research and prototyping, other forms of lithography are required. EBL is currently the main form of non-optical lithography used in nanotechnology applications and is the technique of choice in this current research work. In EBL, a beam of highly focused electrons is directed onto the surface of a substrate, pre-coated with an electron sensitive polymer, in order to define the required masking area. The electron-beam (*e-beam*) is controlled via a multitude of electro-magnets, which are in turn computer controlled [137]. The EBL tool used in this work is a state of the art Vistec VB6-UHR-EWF 100 keV machine, capable of producing a minimum spot size of around 4 nm and resolution of 0.5 nm in a writable field size of  $1.2 \times 1.2$  mm [138].

### 3.3.1 Electron Beam Lithography Resists

One of the most commonly used resists in EBL is polymethyl methacrylate (PMMA), which is applied uniformly on the sample by spinning at speeds between 2-6 krpm. The thin film of resist is then baked at 180 °C for 90 minutes in order to remove any solvents from the film, essentially setting the resist. After exposure to the beam of electrons, the sample is developed in a mixture of methyl isobutyl ketone (MIBK):isopropyl alcohol (IPA) in order to unveil the pattern. The pattern development is typically followed by either a film deposition and lift-off, or an etch process. Another available resist, Hydrogen silsesquioxane (HSQ), which is nominally a spin-on-glass material developed in the microelectronics industry for passivation, can also be employed as a negative tone (as opposed to the positive tone PMMA) EBL resist. The benefit of using this resist is that once developed, it actually forms a SiO<sub>2</sub> pattern that may be used as a hard mask for subsequent etching. Apart from resolution benefits due to direct writing of the mask, this also avoids the requirement of an etch mask deposition, lithography, etch and further resist removal [139]. Major investigation and development of the HSQ lithography process was conducted by the author's colleague, Gabor Mezösi, resulting in a reliable and stable technique for use in photonic device fabrication [140]. All of the lithography steps in this work used PMMA, except for the waveguide definition, which used HSQ. Fig. 3.7 shows a scanning electron microscope (SEM) image of an 800 nm gap width coupler written in HSQ, detailing the levels of precision obtainable using this technique.

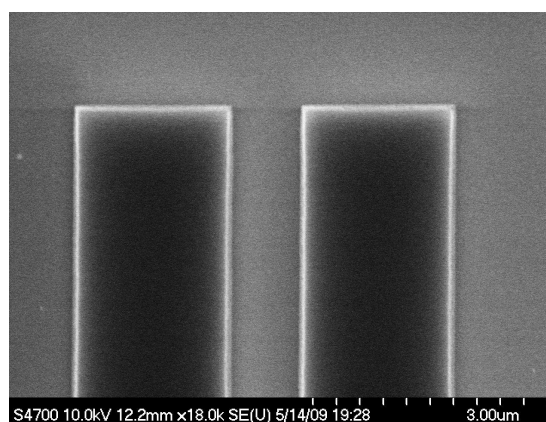


FIGURE 3.7: SEM image of an 800 nm gap width coupler written in HSQ.

### 3.4 Reactive Ion Etching

Dry etching techniques are those that primarily use the chemical and physical interactions in plasma discharges (a highly ionized gas containing positive ions and free electrons) to remove the desired material, as opposed to wet etching that employs liquid based etchants [141]. Dry etching holds several advantages over wet etching, including greater repeatability, anisotropy and less mask undercutting, allowing for the realisation of smaller critical dimensions. The method of dry etching used in this work for waveguide formation is RIE using an Electrotech SRS Plasmafab 340 machine. Typically, a RIE machine consists of a vacuum chamber containing two parallel electrodes, of which the lower one holds the sample to be etched, as shown in Fig. 3.8. The lower electrode is usually smaller in area than the top electrode, which often actually comprises the rest of the entire chamber. RF power is capacitively coupled to the lower electrode, whilst the upper is grounded. The aforementioned asymmetry in the electrode sizes causes most of the voltage drop between the electrodes to appear across the plasma sheath or dark space at the lower, smaller electrode. This voltage drop is known as the direct current (DC) self bias and is proportional to the amplitude of the RF signal and also the ratio of electrode areas. Directionality in RIE is enhanced through the use of low chamber process pressures (typically 5-100 mtorr), lowering the scattering effects of the ions within the plasma (also known as the mean free path). As a simple guide, the basic processes involved in RIE are as follows [137]:

- Generation of a plasma containing the reactive species.
- Transportation of the reactant to the substrate surface via diffusion.
- Absorption of the reactant on the substrate surface.
- Chemical reaction between the reactant and the substrate material to form volatile compounds, as well as physical effects such as ion bombardment.
- Desorption of the by-product compounds from the surface in order to be pumped away by the system.

Chlorine based chemistries have shown to be ideally suited for the more mature GaAs system, however, for InP, high substrate temperatures ( $>150^{\circ}\text{C}$ ) are required to promote the desorption of  $\text{InCl}_3$  in order to maintain a smooth surface

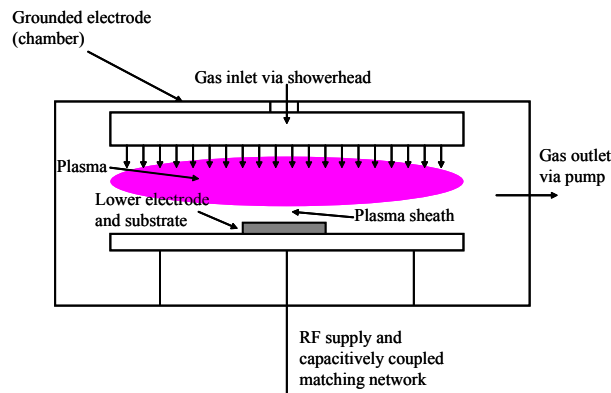


FIGURE 3.8: Typical configuration of a parallel plate RIE system.

after etching. Methane hydrogen ( $\text{CH}_4/\text{H}_2$ ) was first proposed for RIE processing of indium based compound semiconductors, as a good alternative to the chlorine based chemistry, in 1989 by Hayes et al. [142]. Operated at room temperature, hydrocarbon based plasmas provide anisotropic profiles, smooth surfaces and etch rates of a few tens of nm/min. For this type of etching, it has been shown that  $\text{PH}_3$  is the primary phosphorus containing volatile product and that  $\text{In}(\text{CH}_3)_3$  is the indium containing compound. The following details the chemical dissociation processes occurring during the reactive etching of InP with  $\text{CH}_4/\text{H}_2$ :

- $\text{CH}_4 \xrightarrow{e^-} \text{CH}_3 + \text{H}$
- $\text{H}_2 \xrightarrow{e^-} 2\text{H}$
- $3\text{CH}_3 + 3\text{H} + \text{InP} \xrightarrow{e^-} \text{In}(\text{CH}_3)_3 + \text{PH}_3$

An issue with this type of etching, however, is the formation of hydrocarbon polymers on inert surfaces that may compromise etching performance in terms of etch rate and surface roughness. The addition of  $\text{O}_2$ , a known remover of hydrocarbon based polymers through dissociation, may mitigate polymer deposition, and thus also help produce vertical etched sidewalls, as reported in [143, 144], where very promising results were achieved. Normally, the addition of  $\text{O}_2$  in terms of Al-GaInAs etching is problematic in that aluminium oxidises readily, forming  $\text{Al}_2\text{O}_3$ , which is notoriously difficult to etch. Nevertheless, this is used as an advantage here, as it is required that etching is ceased at the depth corresponding to the first aluminium containing layer, i.e. 1920 nm. Etch test samples were prepared using the HSQ EBL process in order to optimise the  $\text{O}_2$  gas flow for waveguide etching,

as excessive amounts may cause undesirable micromasking (as shown in Fig. 3.9) and insufficient  $O_2$  may not oxidise the aluminium enough or remove polymer build up. The optimum recipe for etching was found to be as follows:

- RF platen power=50 W.
- Chamber pressure=30 mtorr.
- Gas flow rates= $CH_4/H_2/O_2$  (6/54/0.16 sccm).
- DC self bias $\approx$ 550 V.
- Table temperature=30 °C.

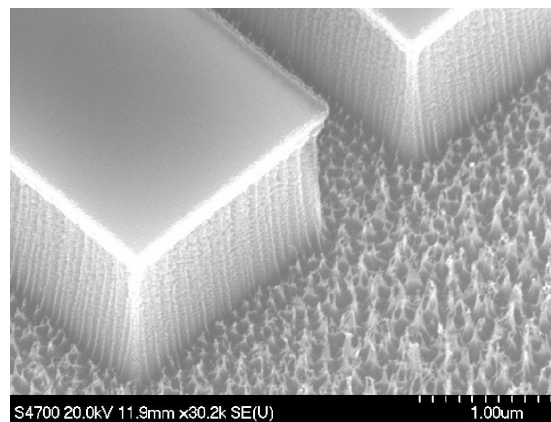


FIGURE 3.9: SEM image of AlGaInAs etched in  $CH_4/H_2/O_2$  where the  $O_2$  content is excessive such that micromasking prevails.

These parameters give an average etch rate of approximately 33 nm/min, therefore in order to etch down 1920 nm, an etch time of 59 min is required. The etch rate of the first aluminium containing layer is around 1 nm/min, giving an etch selectivity of greater than 30:1. Fig. 3.10 shows an SEM image of a waveguide etched in this manner.

### 3.4.1 The Effects of RIE Lag

An important issue to consider when etching small features using RIE is the effect of lag, which transpires when the dimensions of the areas to be etched are sufficiently small such that the etch rate decreases dramatically therein. This is mainly due to restrictions in the angular trajectories of the incident ions, such that, as

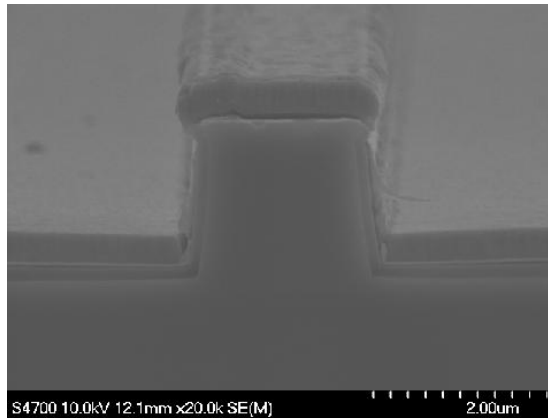


FIGURE 3.10: SEM image of a waveguide etched in the AlGaInAs material using  $\text{CH}_4/\text{H}_2/\text{O}_2$  as described in the text.

the size of the feature to be etched decreases, so too does the number of incident ions impacting upon it, thus decreasing the etch rate. The SEM image in Fig. 3.11 illustrates this effect, which is particularly important in the case of evanescent field couplers where the coupling efficiency is highly dependant on the gap width and depth. Here we wish to etch down to the first aluminium containing layer between the gaps and also outside them, however, due to the differences in etch rates this could prove problematic. The aluminium containing layers are employed as part of electron confinement layers, therefore it would be undesirable to breach them outside the coupler during the etching of the gaps.

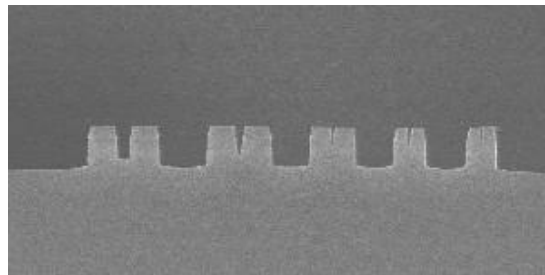


FIGURE 3.11: SEM image of varying widths of coupler gaps etched for a fixed time, demonstrating the effect of RIE lag.

In order to fully assess the effect of RIE lag on the AlGaInAs material, several test runs were carried out to observe the variability in etch rate as a function of gap width and time. The results of this study are shown in Fig. 3.12, where it is evident that for gap widths around 800 nm and above, the effect of RIE lag is not so pronounced. As the designed gaps for the evanescent field couplers are 800 nm, the desired etch depth should still be achievable using 59 min.

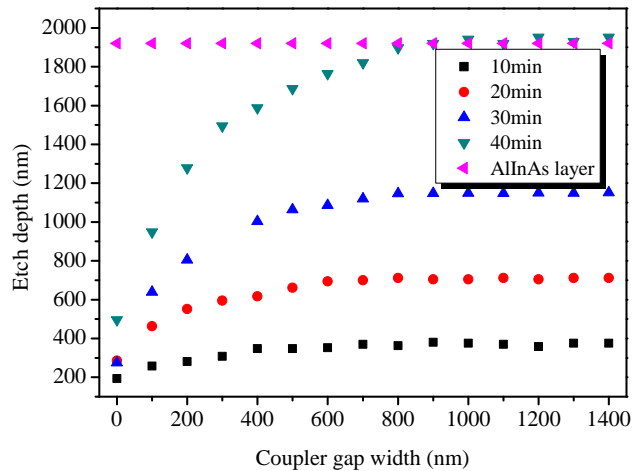


FIGURE 3.12: Effect of RIE lag on etch depth as a function of time and coupler gap width.

### 3.5 Ohmic Contacts

An important feature of most semiconductor devices are ohmic contacts, which allow current to flow into and out of the chip. The term ohmic stems from the fact that the contact should be resistor like in behaviour in so much as it should exhibit a quasi linear I-V relationship, ideally with as low resistivity as possible. However, in practice, problems may occur as simply placing a metal in direct contact with a wide band-gap III-V semiconductor, such as InP, generally results in a rectifying (Schottky) contact rather than an ohmic one, as shown in Fig. 3.13 (a). This is due to the fact that when a metal is placed on a semiconductor, the conduction and valence bands in the semiconductor bend in order to maintain equilibrium in the Fermi-levels between the metal and the semiconductor due to the differences between their work functions  $\phi_m$  and  $\phi_s$ . The work function is defined as being the minimum energy required to raise an electron from the Fermi-level to the vacuum level, thus creating a free space electron. The resulting large potential barrier leads to an asymmetric flow of carriers, giving rise to a non-linear I-V relationship. However, if the doping level in the semiconductor is increased sufficiently, then the depletion region becomes narrower, allowing for electrons to traverse the barrier predominantly via field emission (quantum mechanical tunneling), as shown in Fig. 3.13 (b) [145, 146].

In this work, for the p-type contact, a 200 nm highly Zn doped ( $1.5 \times 10^{19} \text{cm}^{-3}$ ) GaInAs layer, is used for this purpose. For the n-type contact, the InP is doped

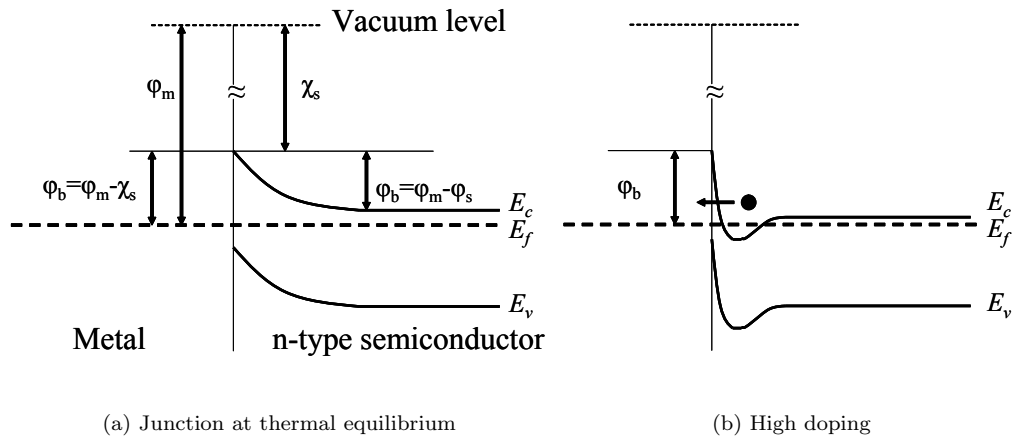


FIGURE 3.13: (a) Energy band diagram of a metal-semiconductor (n-type) junction with  $\phi_m > \phi_s$ , at thermal equilibrium, and (b) with sufficiently high doping such that the tunneling current dominates.

with Si to a level of  $3 \times 10^{18} \text{cm}^{-3}$ . In order to further enhance the performance of the contacts, eutectic alloying may also be employed. For n-type InP a Au/Ge alloy may be used because, as Ge is a group IV element, it may be used to dope the InP. Upon annealing, the Ge diffuses into the region under the contact and dopes the InP degeneratively n-type. Usually, a layer of Ni is also included to improve surface morphology post annealing as it does not form a eutectic with the contact metals at temperatures below the alloying temperature.

### 3.5.1 Metallisation

Various methods exist for the deposition of metal layers to semiconductors, however, as the devices in this work are ridge waveguide based, one must employ sputter deposition (see section 3.12.4.1), at least for the p-type contact, in order to conform to the device topography. For the p-type contact, Ti, Pt and Au layers are used. The Ti is used as an adhesion layer as it is a reactive metal and oxidises readily, adhering well to the dielectric layer ( $\text{SiO}_2$ ) used for isolation. However, as the sheet conductivity of Ti is not exceptional (as compared to Au), only a 33 nm thin layer is deposited. The 66 nm Pt layer is used as a diffusion barrier preventing the Au from penetrating into the semiconductor material. A 340 nm thick top Au layer is used to enhance sheet conductivity allowing for the device to be tested reliably. As for the n-type metallisation, a layer structure of Au/Ge/Au/Ni/Au of thicknesses 14/14/14/11/240 nm is deposited onto the n-type InP, this time using evaporation. The contacts are then alloyed using a RTA for a pre-determined time

at a fixed temperature. The high temperature anneal also breaks down any native surface oxides between the semiconductor and the metals.

### 3.5.2 p-type Ohmic Contact Performance Analysis Using the Transfer Length Method

In order to assess the performance of the p-type ohmic contacts, various methods are available, such as the resistor network model or the differential model. However, the most commonly used technique tends to be the transfer length method (TLM). Here, a patterned test structure consisting of several ohmic contact pads, separated by varying gap widths, is formed on the highly doped semiconductor surface as shown in Fig. 3.14. After annealing, the total resistance between two consecutive pads is measured as a function of distance between the pads using a 4-probe technique, where current is flowed across the gap with the potential difference measured, as shown in Fig. 3.14. The 4-probe technique is used to provide more accurate measurements as it eliminates the parasitic resistance introduced by the probes and connecting wires. This resistance,  $R$ , as a function of gap width  $x$  is given by:

$$R = 2R_c + \frac{R_{sh}}{W}x, \quad (3.1)$$

where  $R_c$  is the contact resistance,  $R_{sh}$  the semiconductor sheet resistance (assumed to be the same both between and under the pads) and  $W$  is the width of the square contacts [141]. By plotting  $R$  as a function of  $x$ , one can then infer the value of the contact resistance,  $R_c$ , by linearly extrapolating the data to the intercept with the  $R$  axis. The slope of the line is equal to  $R_{sh}/W$ , therefore one may also determine the sheet resistivity. Another important quantity, related to the lateral distance necessary for the flow of current into and out of the device, is the transfer length,  $L_t$ , and is equal to  $\sqrt{r_c/R_{sh}}$ , where  $r_c$  is an important parameter known as the specific contact resistance, measured in  $\Omega.mm^2$ . The specific contact resistance may also be expressed as  $r_c=R_cL_tW$  for  $W>1.5L_t$  [31].

TLM patterns were fabricated on the highly doped p-type GaInAs contact layer, then annealed at 380 °C for 60 s. After annealing, the resistance values were measured using a semiconductor parameter analyser, with the results being plotted

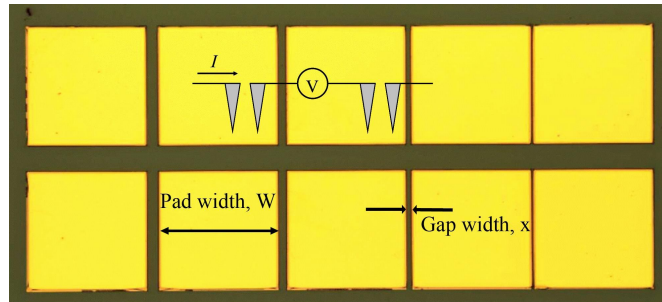


FIGURE 3.14: Optical image of two fabricated TLM test structures for measuring contact resistance. The pad width,  $W$ , is  $194\ \mu\text{m}$  and the distance between pads,  $x$ , varies from  $10\text{--}25\ \mu\text{m}$  in  $5\ \mu\text{m}$  steps.

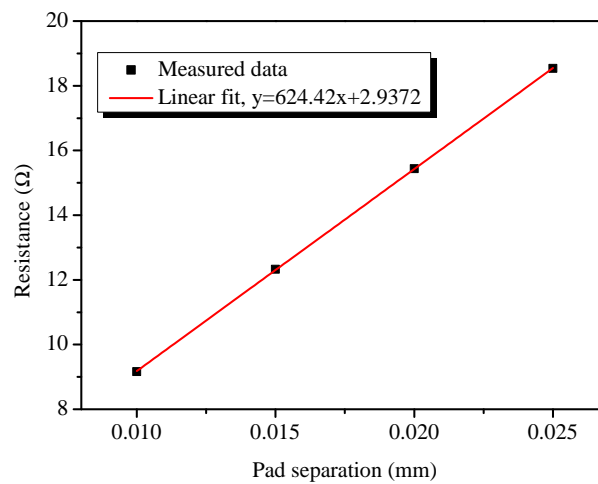


FIGURE 3.15: Results of TLM measurement on highly doped p-type GaInAs contact layer, annealed at  $380\ ^\circ\text{C}$  for 60 s.

in Fig. 3.15. The linear extrapolation of the data points intersects the  $R$  axis at  $2.94\ \Omega$ , indicating a contact resistance value of  $R_c=1.47\ \Omega$ . Here  $L_t=2.35 \times 10^{-3}\ \text{mm}$ ,  $R_{sh}=1.21 \times 10^2\ \Omega/\text{sqr}$  and  $r_c=6.70 \times 10^{-4}\ \Omega.\text{mm}^2$ . These results show that the p-type ohmic contacts are suitable for the devices in this research (typical values required lie between  $r_c=0.8$  to  $8 \times 10^{-4}\ \Omega.\text{mm}^2$  [141]).

### 3.6 Waveguide Loss Measurements

Characterisation and optimisation of the propagation losses in passive waveguide interconnects is vital in the design of photonic integrated circuits. In this work, the waveguides are blue shifted by  $>100\ \text{nm}$ , as detailed in section 3.2.1.3, in order to minimise direct band-gap absorption. Several techniques exist for measuring

the propagation losses, however, the FP resonance method is used here due to its simplicity, accuracy and reproducibility [147]. In this measurement, the ratio of the resonant and anti-resonant transmission is measured, from which the propagation loss can then be deduced. This allows the technique to be less sensitive to coupling efficiency, unlike other methods such as the cut back technique. The transmitted optical intensity through a FP cavity,  $I_T$ , is related to the incident intensity,  $I_I$ , via:

$$\frac{I_T}{I_I} = \left( \frac{(1 - R)^2 \exp^{-\alpha L}}{1 - 2R \exp^{-\alpha L} \cos 2kL + R^2 \exp^{-2\alpha L}} \right), \quad (3.2)$$

with  $R$  being the mean facet reflectivity,  $\alpha$  the propagation loss,  $L$  the cavity length,  $n$  the effective index of the propagating mode and  $k$  the angular wave number, equal to  $2\pi n/\lambda$ .

The mean facet reflectivity is equal to  $\sqrt{r_1 r_2}$ , where the single facet reflectivity is defined, using the Fresnel equations, as [31]:

$$r = \left( \frac{n_{eff} - n_0}{n_{eff} + n_0} \right)^2. \quad (3.3)$$

Maxima and minima of  $I_T/I_I$  occur when  $2kL=0$  and  $2kL=\pi$  respectively, thus the propagation loss can then be calculated using:

$$\alpha = -\frac{1}{L} \ln \left( \frac{\sqrt{C_r} - 1}{R(\sqrt{C_r} + 1)} \right), \quad (3.4)$$

where  $C_r$  is the maximum to minimum ratio of the transmitted FP fringes, given by:

$$C_r = \frac{I_{T(max)}}{I_{T(min)}}. \quad (3.5)$$

The experimental set-up used for determining the waveguide propagation losses is shown in Fig. 3.16. A tunable laser was used as the light source, which was mechanically chopped at a low frequency in order to synchronise it with the lock-in amplifier for signal to noise ratio enhancement. A polarising beam splitting cube was used to select the desired polarisation state of the input light signal. The light

was coupled into and out of the waveguide via microscope objective lenses, with an iris being placed after the output lens in order to allow the Ge photodetector to capture only the light from the coupled waveguide mode. For alignment, the photodetector was replaced with an infra-red camera. All measurements were controlled and acquired using a PC via LabView. Passive waveguides were realised using the fabrication techniques described previously and measured, with Fig. 3.17 showing a typical FP resonance curve obtained in the wavelength range of 1560-1561 nm for the TE polarisation state.

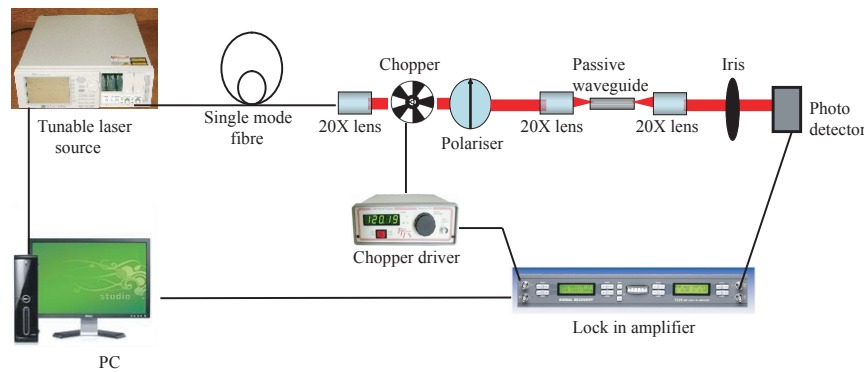


FIGURE 3.16: Experimental set-up for the FP waveguide propagation loss measurements.

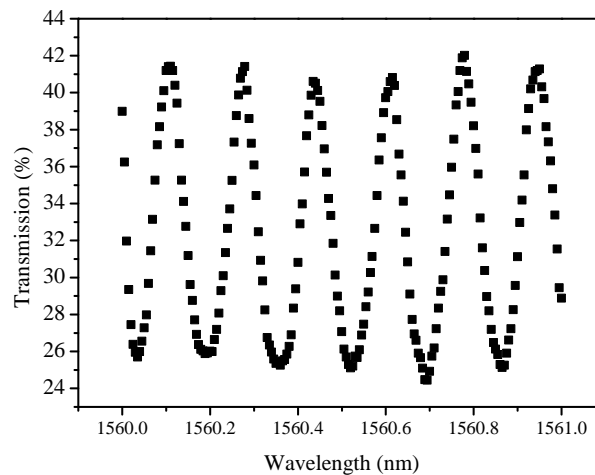


FIGURE 3.17: Transmitted FP optical intensity from an intermixed passive waveguide (>100 nm blue shift) for the TE polarisation state.

The measured FSR of the cavity corresponds to a wavelength spacing of around 0.156 nm, indicating a cavity length of around 2.2 mm, as designed. Now, by using equations 3.4 and 3.5, the data in Fig. 3.17 and the indices  $n_{eff}=3.201$  and  $n_0=1$  inserted into equation 3.3, the propagation loss can be calculated. The calculated

loss at this wavelength and polarisation state is  $4.25 \text{ cm}^{-1}$ . Similar scans were taken for various wavelengths, with the results being shown in Fig. 3.18. The waveguide propagation losses obtained using this intermixing technique are suitable for low loss passive waveguide interconnects in prototype devices.

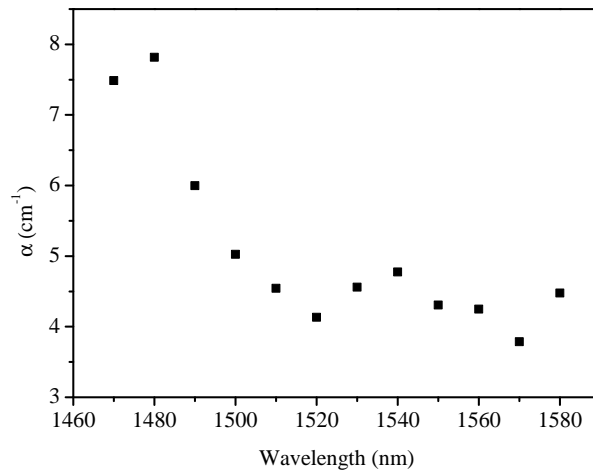


FIGURE 3.18: Passive waveguide propagation loss as a function of input wavelength for the TE polarisation state.

### 3.7 Broad Area Laser Results

Gain guided lasers are a type of broad area laser (BAL) that utilise a contact stripe along the cavity in order to achieve lasing. However, as there is no lateral carrier confinement, injected carriers can diffuse laterally, decreasing the lasing efficiency. Also, as there is no lateral index change to confine photons along the cavity, optical losses tend to be high [34]. Nevertheless, they are very simple to fabricate and are thus useful as a fast and inexpensive way of characterising laser material. The stripe width may be chosen such that it allows the neglect the current spreading effect in the upper cladding of the material. The current spreading makes the effective current injection area larger than the actual area of the stripe structure, which introduces errors in the determination of current densities [34]. The gain guiding structure is also free from extra losses (mainly scattering) that could be introduced by an index guided ridge, for example. It has been shown that the threshold current density of a QW laser of length  $L$  is approximately given by [104]:

$$J_{th} \simeq J_{\infty} \exp\left(\frac{L_0}{L}\right), \quad (3.6)$$

where  $J_{\infty}$  is the threshold current density in a laser of infinite cavity length, given by:

$$J_{\infty} = \frac{n_w J_t}{\eta_i} \exp\left(\frac{\alpha}{g_0 n_w \Gamma}\right), \quad (3.7)$$

with

$$L_0 \simeq \frac{\ln(1/R)}{g_0 n_w \Gamma}. \quad (3.8)$$

In the above equations,  $L_0$  is the optimum cavity length at which  $I_{th}$  is minimised for the number of wells,  $n_w$ . The parameter  $J_t$  is the transparency current density per well,  $\eta_i$  is the internal quantum efficiency (representing the fraction of carriers recombining radiatively),  $\alpha$  is the material loss and  $\Gamma$  is the optical confinement factor per QW.  $R$  is the mean reflectivity of the mirrored facets. Inserting equations 3.7 and 3.8 into equation 3.6 and rearranging we obtain:

$$\ln(J_{th}) \simeq \ln(J_{\infty}) + \frac{L_0}{L}. \quad (3.9)$$

Thus by plotting  $\ln(J_{th})$  versus  $1/L$ , we can infer both  $L_0$  (and hence  $g_0$ ) and  $J_{\infty}$  from the slope and intercept of the linear extrapolation of the data values.

Various cavity lengths of gain guided BALs with a  $75 \mu\text{m}$  current injection stripe were fabricated on the MQW material, and then tested under pulsed conditions in order to obtain optical power versus injected current (L-I) plots. From these plots, the threshold current,  $I_{th}$ , and thus  $J_{th}$  can be extracted allowing  $\ln(J_{th})$  versus  $1/L$  to be plotted, as shown in Fig. 3.19.

Analysis of the data results in a  $J_{\infty}$  value of  $260.5 \text{ Acm}^{-2}$  and  $L_0=0.0411 \text{ cm}$ . Knowing there are five wells and that the confinement factor per well,  $\Gamma=0.01$ , it follows that  $g_0=629 \text{ cm}^{-1}$ . These values compare well with other measurements made on the aluminium quaternary, and indicate that the material is of high quality [70].

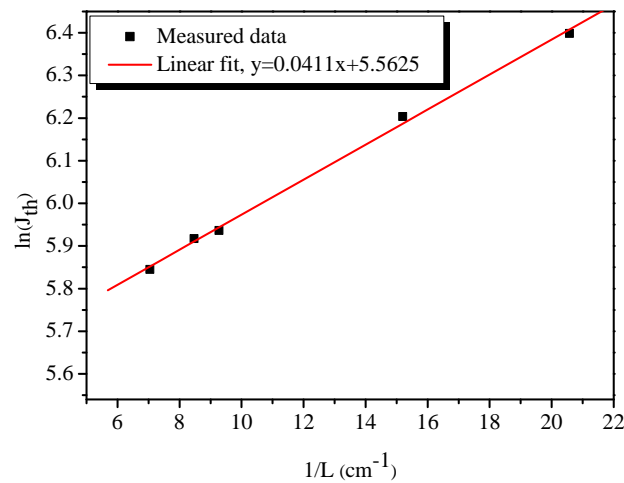


FIGURE 3.19: Plot of  $\ln(J_{th})$  as a function of inverse length for BALs fabricated on the AlGaInAs material.

### 3.8 Ridge Waveguide Laser Results

The use of a ridge waveguide greatly increases the efficiency of the laser device, mainly due to an added degree of current and photon confinement created by etching a ridge into the material, and opening up a narrow current injection window on top of it. The ridge width and etch depth are chosen to ensure single-mode operation, as described previously. These devices allow more accurate evaluations of parameters such as the characteristic temperature of the material,  $T_0$ , which describes the temperature dependence of the threshold current. Ridge waveguide laser (RWGL)s were fabricated using the processing techniques, as described previously, then were thinned, cleaved and mounted to a copper mount using conductive epoxy ready for testing. The measurements were carried out using a thermoelectric controller (TEC) module, a current source and a GaInAs photodetector. In order to assess  $T_0$ , a device of cavity length 1.667 mm was measured as a function of TEC temperature, with the results shown in Fig. 3.20.

It is evident from the data that the threshold current of the laser increases with increasing temperature. The degree of temperature dependence relies upon the value of  $T_0$ , which is in turn related to the material and device structure. This is due to the fact that as the temperature rises, so too does the transparency carrier density and thus the gain decreases as the injected carriers spread over a larger range in energy [34]. The losses also increase with temperature due to the

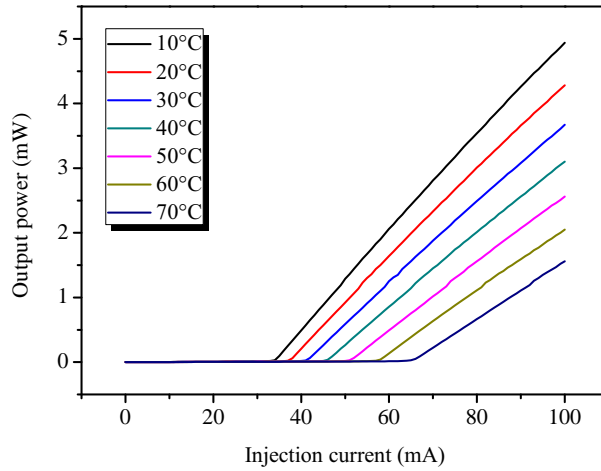


FIGURE 3.20: Measured L-I curves of a 1.667 mm long RWGL for varying TEC temperature values.

higher carrier densities required for threshold. The relationship between threshold current and  $T_0$  is described by the empirical equation [31, 148]:

$$I_{th} = I_{th0} \exp\left(\frac{T}{T_0}\right), \quad (3.10)$$

where  $I_{th}$  is the threshold current,  $I_{th0}$  is the extrapolated threshold current at 0 K, known as the characteristic current, and  $T$  is the temperature in Kelvin. From the measured data plotted in Fig. 3.20, the value of  $T_0$  can be evaluated by plotting the natural log of the threshold current versus the operating temperature, as shown in Fig. 3.21. The linear fit of the measured data yields a  $T_0$  value of around 94 K, which is amongst the highest ever reported values for the AlGaInAs system. Measured values tend to range from 50-70 K [34].

### 3.9 Intermixed Ridge Waveguide Laser Results

The spatial resolution of the intermixing process in the AlGaInAs material, in terms of the band-gap grading occurring at intermixed/non-intermixed interfaces, is a vital property that has to be assessed. Also, the accompanying grading occurring in other material parameters, for example, slope efficiency and threshold current (related to the internal quantum efficiency), and the electrical properties (related to the doping and other material parameters), require to be obtained.

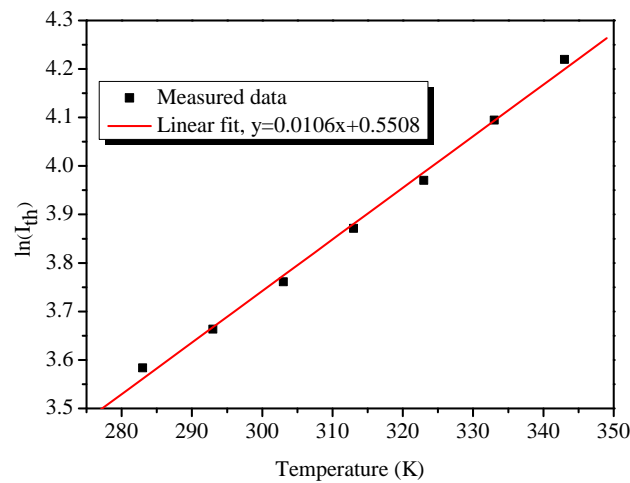


FIGURE 3.21: Plot of the natural log of  $I_{th}$  versus  $T$  for a 1.667 mm long RWGL.

Such knowledge of the distance and extent to which these parameters are graded at the intermixed/non-intermixed interface is important in the design of photonic integrated circuits comprising both active and passive sections. Prior to laser fabrication, a sample was selectively intermixed using the QWI process, as detailed in section 3.2.1.3, such that bands of intermixed material were defined running parallel to the individual laser cavities, which were spaced  $100\ \mu\text{m}$  apart. This produced bars of lasers in which a number of devices were intermixed to varying extents depending upon their proximity to the intermixed bands running up and down the chip, as shown in Fig. 3.22.

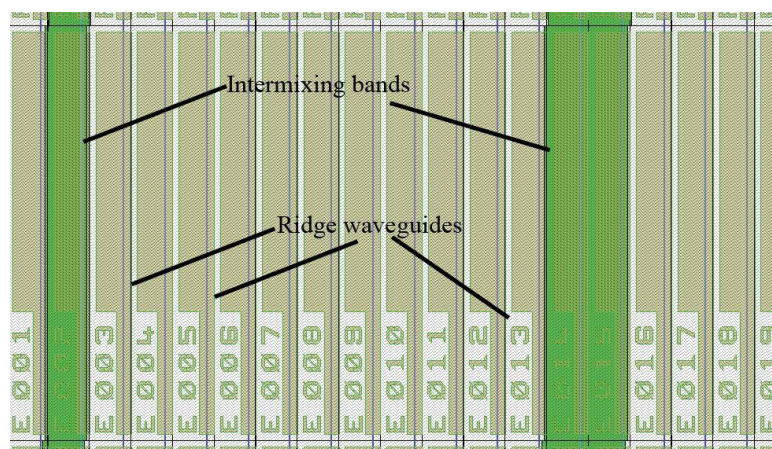


FIGURE 3.22: Chip design for intermixing experiments, showing bands of intermixed material defined to run parallel to the laser cavities.

Optical power/voltage versus injected current (L-I-V) curves were measured for a full bar of 30 devices, with the slope efficiency and threshold current values being

plotted in Fig. 3.23. It is shown, as expected, that the slope efficiency degrades inside, or near to, the intermixed regions, with the threshold current showing a similar trend. There are three distinct regimes visible, the nominal values where the devices are far from the intermixing band, moderately degraded values where the devices are in close proximity to the bands (within  $60\ \mu\text{m}$ ), and extremely degraded values where the device is located directly within the intermixing band. This would imply that in order to maintain the optical properties of any active devices, they must be located at least  $60\ \mu\text{m}$  away from any intermixing sections.

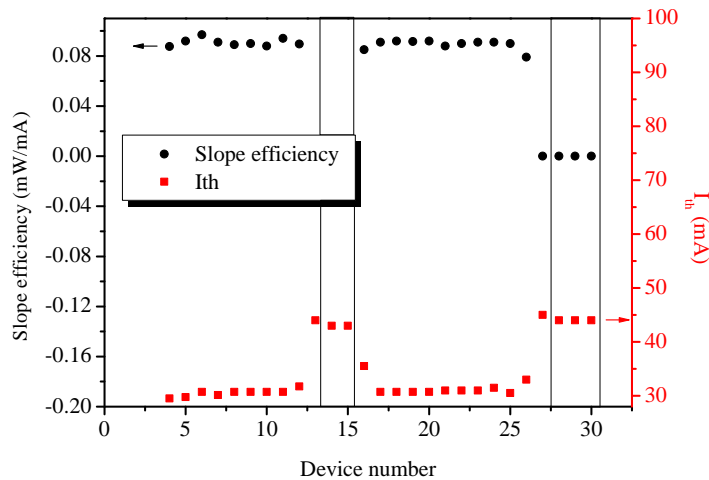


FIGURE 3.23: Measured slope efficiency and threshold current as a function of device number on the bar. The black outlined regions indicate where intermixing boundaries were defined.

Fig. 3.24 shows a similar plot, this time for the voltage drop at 10 mA injection current and the device series resistance,  $R_s$ , defined as being the slope of the V-I curve above the turn on voltage. A similar pattern as before is observed, showing degradation in the parameters as the emitter cavity nears the intermixing band and complete degradation once within it. As with the optical properties, in order to maintain full electrical performance, any active devices should be placed at least  $60\ \mu\text{m}$  from sections that have been intermixed.

TLM patterns were also fabricated directly within an intermixed region to assess the extent of the deterioration in contact resistance and related parameters as a result of intermixing. The parameters obtained were  $R_c=3.34\ \Omega$ ,  $L_t=2.44 \times 10^{-3}\ \text{mm}$ ,  $R_{sh}=2.65 \times 10^2\ \Omega/\text{sqr}$  and  $r_c=1.58 \times 10^{-3}\ \Omega \cdot \text{mm}^2$ . It is evident that there is an order of magnitude increase in the specific contact resistance as compared to the non-intermixed case. It is thought that the mechanism contributing to the

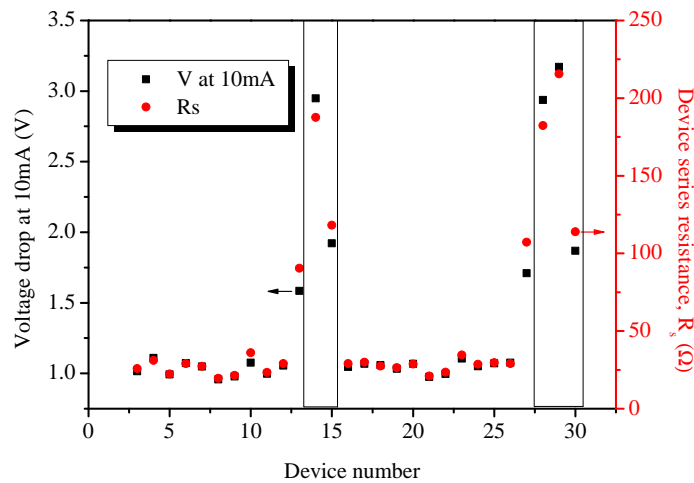


FIGURE 3.24: Measured voltage drop at 10 mA and calculated series resistances a function of device number on the bar. The black outlined regions again indicate where intermixing boundaries were defined.

increase in resistance is the abundance of vacancies leading to carrier traps, i.e. non-radiative recombination centres, thus increased resistance.

### 3.10 Experimental Characterisation of Electro-Optic Effects

A multi-section technique for measuring the spectral loss and/or gain of semiconductor material has been successfully employed in the past [149, 150]. Here, a similar structure/technique was used to characterise the absorption properties of the AlGaInAs material, then through the Kramers-Kronig relations, the refractive index change,  $\Delta n$ . Fig. 3.25 shows the device design consisting of a ridge waveguide laser with three independent biasing sections, each 500  $\mu\text{m}$  long with 20  $\mu\text{m}$  isolation gaps between each section. The facet at section 3 was scribed not cleaved to ensure single pass measurements.

The experimental set-up used for the measurements is shown in Fig. 3.26. Section 2 is biased with with a constant current,  $I_{source}$ , to act as a source of spontaneous emission, then various values of current,  $I_{probe}$ , are applied to section 1, allowing the output spectra to be collected, via objective lenses and a polariser, by an OSA. The current source and OSA are controlled via a PC using LabView. The

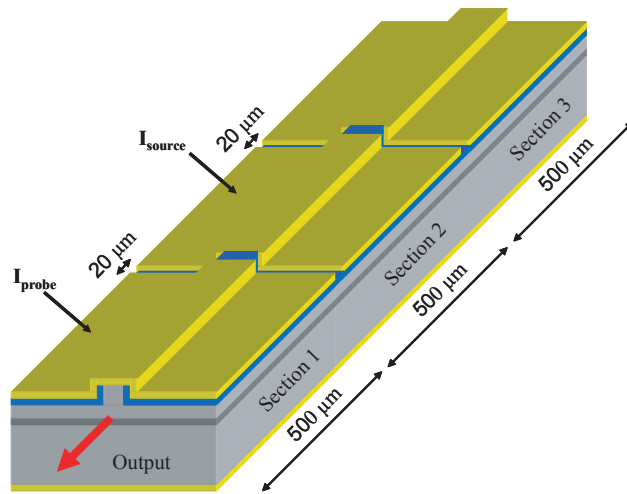


FIGURE 3.25: Schematic illustration of the three section device for the gain/loss measurements. The facet at section 3 is scribed not cleaved to ensure single pass measurements.

light produced in a pumped section will propagate along the guide with the power decreasing exponentially according to the following equation:

$$P_{\alpha} = P_{source} \exp(-\alpha L), \quad (3.11)$$

where  $P_{\alpha}$  is the transmitted light power measured at the end of the waveguide,  $P_{source}$  is the light produced in the pumped section,  $L$  is the length of the section and  $\alpha$  is the loss factor.

For differing values of  $I_{probe}$ , the absorption coefficient spectrum of the material, as a function of wavelength and current, can be calculated from the output spectrum by rearranging equation 3.11 such that:

$$\alpha(\lambda, I) = -\frac{1}{L} \ln \left( \frac{P_{\alpha}(\lambda, I)}{P_{source}(\lambda)} \right). \quad (3.12)$$

The polariser was set to allow only TE polarised light to pass and the source current,  $I_{source}$ , was set at 100 mA on section 1 in order to collect the spectrum. It was then applied to section 2 for the rest of the measurements. Fig. 3.27 shows the measured TE polarised spectra when  $I_{probe}$  was varied from 0 to 40 mA (0 to  $8.0 \text{ kAcm}^{-2}$ ) on section 1.

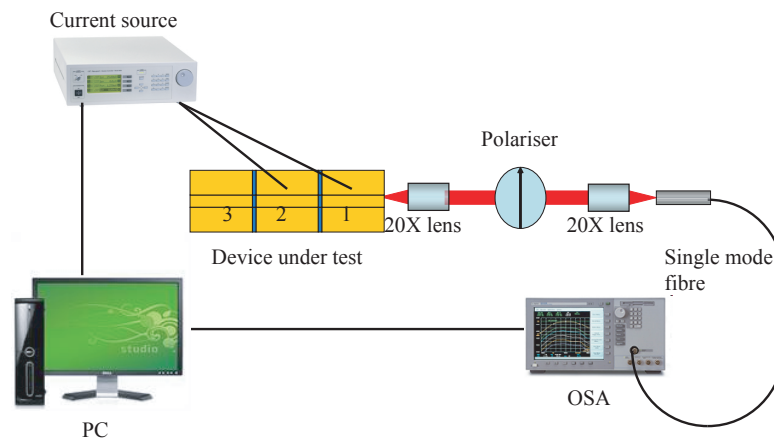


FIGURE 3.26: Experimental set-up for the gain/loss measurements showing the device under test.

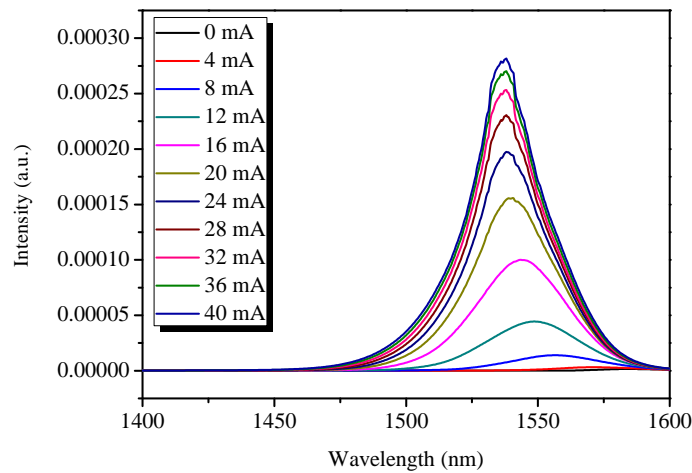


FIGURE 3.27: Measured TE polarised optical spectra for  $I_{probe}$  varied from 0 to 40 mA on section 1.

As expected, with increasing values of current injection the intensity of the output spectra increases. Using the spectra from Fig. 3.27 and equation 3.12, the absorption spectra was then calculated, with the results being shown in Fig. 3.28.

As the applied current density increases, a blue shift in the absorption band edge is observed. There is also a reduction of the peak absorption value, as well as increase of the absorption band edge slope. These factors are as expected from the theory of carrier induced effects. The internal modal loss,  $\alpha_i$ , may also be deduced from the region of the spectra below the band-gap, where the losses are independent of wavelength and due only to free carrier absorption and scattering losses [149, 151]. From the plot, a value of around  $22 \pm 2 \text{ cm}^{-1}$  is obtained.

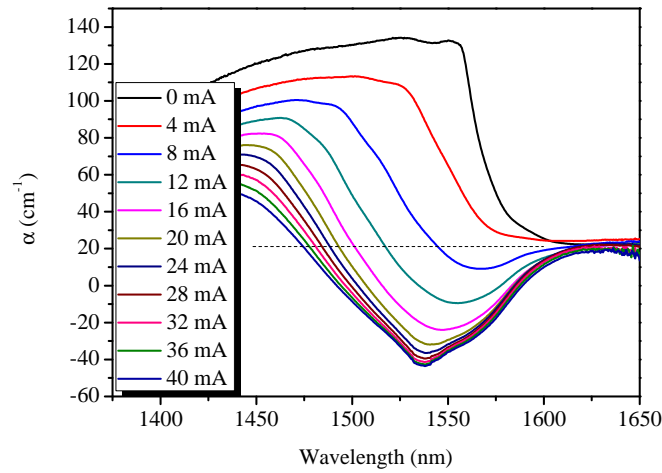


FIGURE 3.28: Measured TE polarised absorption coefficient spectra for  $I_{probe}$  varied from 0 to 40 mA on section 1. The dashed line shows the internal modal loss,  $\alpha_i$ , due only to scattering and free carrier absorption.

The change in absorption coefficient,  $\Delta\alpha$ , is calculated by subtracting the absorption values with no carrier injection from the values with injection, i.e.:

$$\Delta\alpha(\lambda, I) = \alpha(\lambda, I) - \alpha(\lambda, 0). \quad (3.13)$$

As  $\alpha$  decreases with increasing current injection, so too should  $|\Delta\alpha|$ . Fig. 3.29 shows a plot of the TE polarised  $\Delta\alpha$  spectra, confirming the increase in  $|\Delta\alpha|$  with increased current injection.

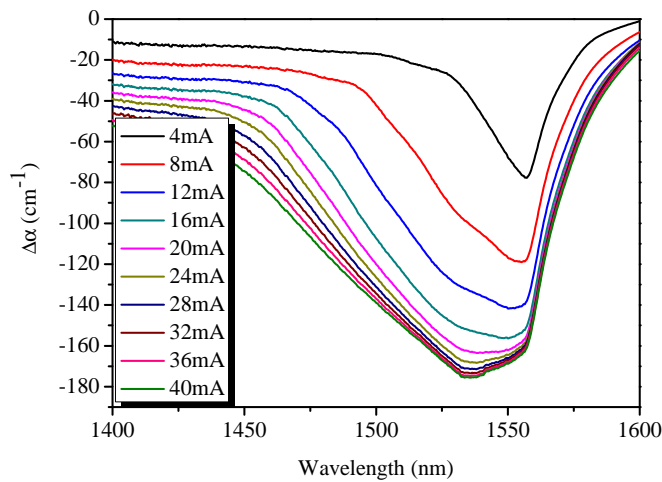


FIGURE 3.29: Change in TE polarised absorption coefficient,  $\Delta\alpha$ , versus wavelength for  $I_{probe}$  varied from 0 to 40 mA on section 1.

One can now determine the change in refractive index,  $\Delta n$ , as a function of the photon energy (or wavelength) and injection current from the  $\Delta\alpha$  spectra using the Kramers-Kronig relation, defined as follows [46]:

$$\Delta n(E, I) = \frac{c\hbar}{\pi} \int_0^\infty \frac{\Delta\alpha(E', I)}{E'^2 - E^2} dE', \quad (3.14)$$

where  $E$  is the photon energy and  $\hbar$  is the reduced Planck's constant. According to the Kramers-Kronig integral, the change in absorption should be calculated over the range from 0 to  $\infty$ . However,  $\Delta\alpha$  values can only be measured over a finite wavelength span, thus to increase the accuracy of the integral, an additional data interpolation process was undertaken to extend the wavelength range. A commonly used practice is to linearly extrapolate the  $\Delta\alpha$  values to zero outside the measured wavelength range. Here, it is assumed that far above and below the band-gap, the changes in absorption are negligible [152]. To this effect, the upper and lower wavelength (energy) values for the integral were chosen to be 2000 and 1000 nm respectively.

The resulting  $\Delta n$  spectra, as calculated using equation 3.14, are shown in Fig. 3.30. As predicted from theory, maximum values of  $\Delta n$  occur just above the band-gap of the material, with the value of  $\Delta n$  being negative for wavelengths above the nominal band-gap and decreasing as the wavelength is detuned from the nominal.

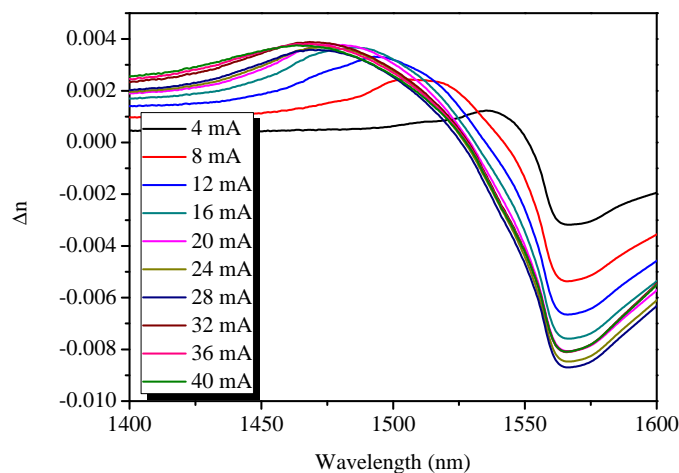


FIGURE 3.30: Change in refractive index,  $\Delta n$ , versus wavelength for  $I_{probe}$  varied from 0 to 40 mA on section 1.

As detailed previously, an important factor in the design of electro-optic based devices is the chirp parameter,  $\rho$ . From the data in 3.29 and 3.30,  $\rho$  can be

calculated as a function of wavelength and injected current. These values are presented in Fig. 3.31. The operational wavelength of such electro-optic phase shifting devices must be chosen carefully, as the proximity of it to the absorption band edge is limited by direct band-gap absorption losses, however, detuning too far away may compromise the electro-refraction strength. A general rule of thumb is to attain a chirp parameter of 10 or above [34]. This value is also shown on the plot. In order to obtain a value of 10 or above here, an operating wavelength of above 1573 nm should be used.

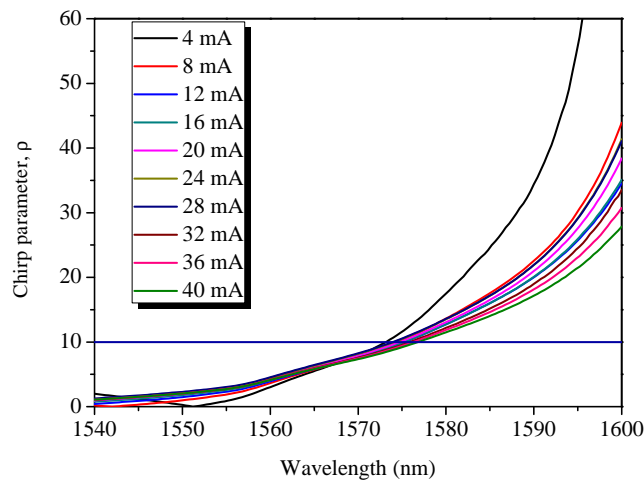


FIGURE 3.31: Chirp parameter as a function of wavelength and applied current injection.

### 3.10.1 Impact of SISA on Electro-Optic Effects

By implementing SISA in the three section devices, the electro-optic effects of the band-gap shifted material can also be assessed. This analysis is vital for the successful operation of the monolithically integrated OCDMA device as the active ring laser material has the same band-gap as the phase shifting sections, therefore signals would incur direct band-gap absorption as they traverse these sections. By carefully detuning the absorption band edge of the phase shifting sections using SISA, the losses can be minimised whilst still maintaining the required electro-refractive effect.

From previously, it is known that SISA with a 20% fill factor gives a wavelength blue shift of 13 nm, and a 38 nm shift with a 30% fill factor. These values are within the range where optimum detuning would occur, therefore were applied to

the three section devices. However, from the TLM results of section 3.9, it is also known that intermixing directly beneath a contact increases the specific contact resistance significantly and thus, through resistive heating, may lead to early device failure. To circumvent this issue, the SISA patterns were placed in close proximity to the waveguide, as shown in Fig. 3.32, so as not to fully compromise the electrical performance of the phase shifting sections. The distance between the intermixing region and the waveguide,  $x$ , was varied between 0.5 and 8  $\mu\text{m}$ .

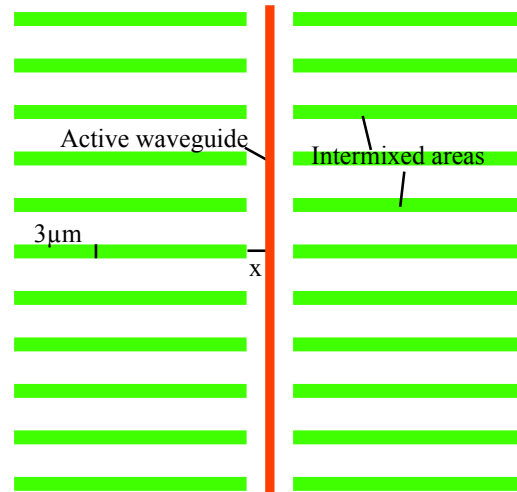


FIGURE 3.32: Schematic layout of the three section SISA devices.

Using the same experimental procedures described previously for the non-intermixed three section devices, the electro-optic effects of the SISA devices were assessed. Fig. 3.33 shows examples of TE polarised absorption spectra for a device with a 30% SISA fill factor placed 4  $\mu\text{m}$  from either side of the waveguide.

From the  $\alpha$  plots, the absorption band edge for the SISA based devices were obtained and are shown, as a function of the distance from the waveguide, in Fig. 3.34.

As expected, the absorption band edge blue shifts as the SISA pattern moves closer to the waveguide. Also apparent is that the more dense fill factor leads to a greater wavelength shift. As the gain peak of the material is known to be around 1552 nm, it is vital to assess the losses at this wavelength from the absorption plots. The losses at 1552 nm as a function of distance from waveguide and SISA are shown in Fig. 3.35. The losses decrease as the intermixing pattern is placed in close proximity to the waveguide. Using 30% SISA at a distance of 4  $\mu\text{m}$  from the waveguide gives a reduction in the losses at 1552 nm from 132  $\text{cm}^{-1}$  to

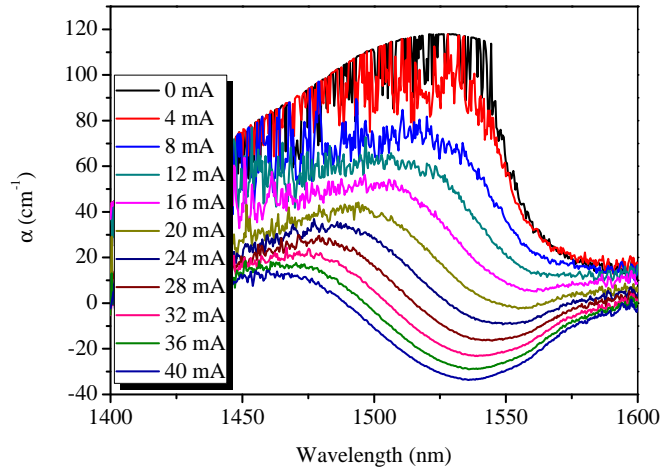


FIGURE 3.33: Measured TE polarised absorption coefficient spectra for  $I_{probe}$  varied from 0 to 40 mA on section 1 for a three section device with 30% SISA fill factor placed  $4 \mu\text{m}$  from the waveguide.

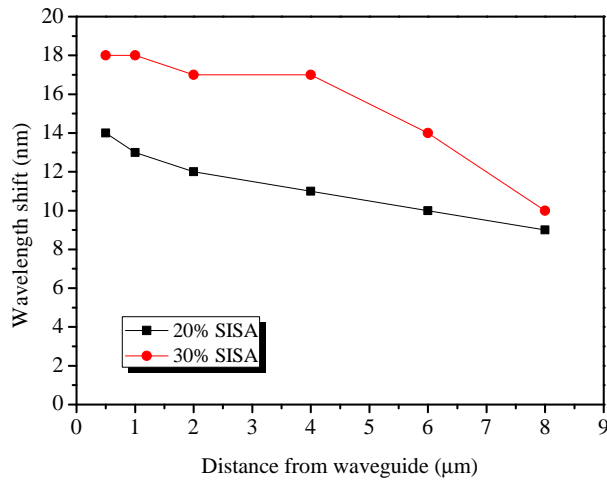


FIGURE 3.34: Shift in absorption band edge wavelength versus distance from waveguide.

$55 \text{ cm}^{-1}$ . This distance from the waveguide also gives a safe margin in order not to severely compromise the electrical performance of the phase shifting sections. Using equations 3.13 and 3.14, the electro-refraction effects of this geometry were calculated. The results are plotted in Fig. 3.36. Comparing these results with the non-intermixed case, as in Fig. 3.30, there is a blue shift in the wavelength where the maximum value of  $\Delta n$  occurs at a wavelength shift of 17 nm, agreeing well with the absorption band edge shift, as detailed in Fig. 3.34.

As with the non-intermixed three section devices, the chirp parameter was assessed

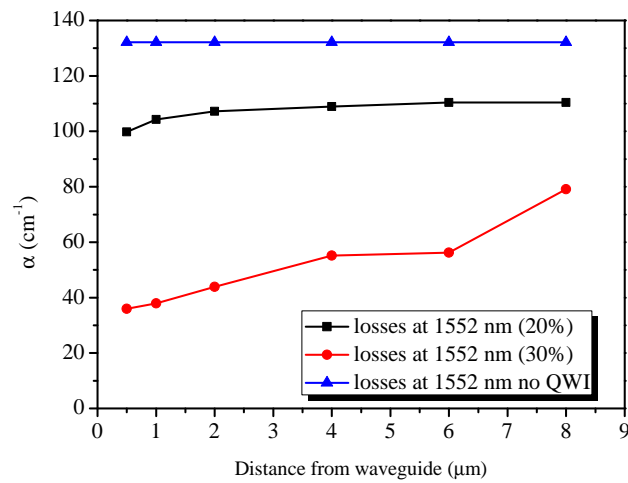


FIGURE 3.35: Losses at 1552 nm as a function of intermixing and distance from the waveguide.

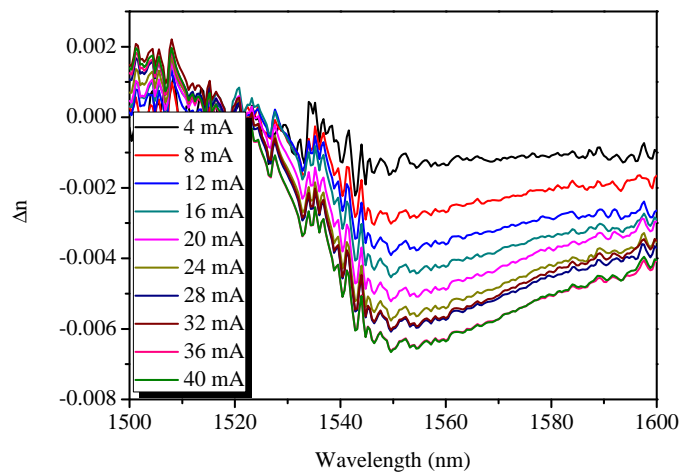


FIGURE 3.36: Change in refractive index  $\Delta n$  versus wavelength for three section device with 30% SISA at a distance of  $4 \mu\text{m}$  from the waveguide.

for this design geometry. It was found that at 1552 nm, the chirp parameter varied from 10 at 4 mA to 6 at 40 mA. These results are shown in Fig. 3.37. Although not the greatest, these values are quite acceptable, therefore were used in the OCDMA AMZI device design.

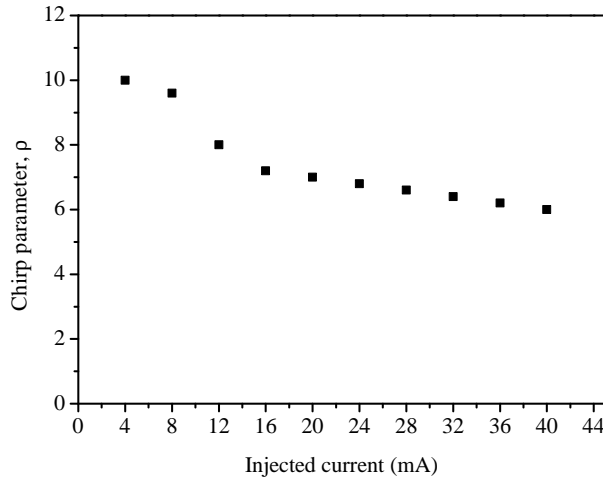


FIGURE 3.37: Chirp parameter for the 30% SISA, 4  $\mu\text{m}$  device, as a function of injected current at an operating wavelength of 1552 nm.

### 3.11 Relaxation Oscillation Frequency Measurements

The mutually coupled oscillations between the photon and carrier densities in lasers lead to a natural resonance within the cavity, known as the relaxation resonance frequency,  $f_r$  [34]. The term relaxation stems from the fact that the photons and carriers attempt to relax back to their steady state values. Knowledge of this frequency is important for determining a number of fundamental laser variables enabling predictions of how the device should perform given certain operating conditions, for example, how fast the device can be modulated.

It has been shown from, the laser rate equations, that the relaxation oscillation frequency is proportional to the square root of the difference between the injection current and the threshold current, such that a linear relationship should be observed, thus [153]:

$$f_r = \frac{1}{2\pi} \sqrt{\left(\frac{dg}{dN_g}\right) \frac{I - I_{th}}{eV} \frac{1}{\tau_p}}, \quad (3.15)$$

where  $\frac{dg}{dN_g}$  is the differential gain,  $I$  is the injected current,  $I_{th}$  is the threshold current, and  $\tau_p$  is the photon lifetime. To confirm this,  $f_r$  was measured for a 1 mm long device, using an RF spectrum analyser, as a function of injected current, with

the results being shown in Fig. 3.38. The dependance on the square root of the difference in injection levels is indeed linear, as expected.

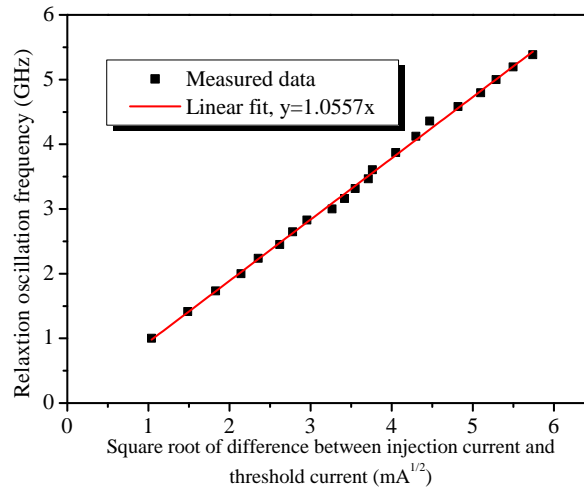


FIGURE 3.38: Relaxation oscillation frequency versus square root of injection current minus threshold current, as determined from direct measurement using an RF spectrum analyser.

An important parameter that may now be deduced knowing the dependance of  $f_r$  on injected current is the carrier lifetime,  $\tau_s$ , i.e. the average time it takes excess minority carriers to recombine. It has been shown that the carrier lifetime may be approximated using [154]:

$$\tau_s = \frac{I/I_{th} - 1}{\tau_p(2\pi f_r)^2}, \quad (3.16)$$

where the only unknown value is the photon lifetime in the cavity,  $\tau_p$ . However, this may be obtained easily as it is known that the photon decay rate is equal to:

$$1/\tau_p = \nu_g(|\alpha_i| + \alpha_m), \quad (3.17)$$

where  $\nu_g$  is the group velocity:

$$\nu_g = c/n_g, \quad (3.18)$$

$|\alpha_i|$  is the internal modal loss= $22 \pm 2\text{cm}^{-1}$ , and  $\alpha_m$  is the mirror loss equal to:

$$\alpha_m = (1/L) \ln(1/R), \quad (3.19)$$

which is equal to  $26 \text{ cm}^{-1}$  for a 1 mm long cavity [34]. Entering all of the values yields a carrier lifetime value of around  $273 \pm 16 \text{ ps}$  for this material. Comparing this result with values of 550-800 ps obtained for  $1.3 \mu\text{m}$  AlGaInAs MQW lasers [155], shows that the material is of good quality and suitable for high speed operation.

## 3.12 Antireflection Coatings

A commonly used technology in the fabrication of optical devices is the application of antireflection (AR) coatings. As the name suggests, such optical coatings are employed in order to reduce any undesired reflections from device interfaces back into the optical system by means of constructive and destructive interference. For example, in SOAs, AR coatings with reflectance values in the range of  $r=10^{-4}$  are applied to the cleaved facets in order to suppress the FP spectral gain ripple [156]. However, it is believed that coatings in the order of  $r=10^{-3}$  are sufficient for the devices in this thesis.

### 3.12.1 Single-layer Coatings

The simplest form of thin film AR coatings are single-layer. In this case, the thickness of the film is chosen to be equal to  $\lambda_0/4n_f$ , where  $\lambda_0$  is the free space wavelength of the light at normal incidence and  $n_f$  is the refractive index of the non-absorbing coating film. Low reflectance values can be obtained if  $n_f$  is chosen such that its index is equal to the square root of the substrate index,  $n_s$ , multiplied by the index of the incident medium,  $n_0$ , as shown in the following equation [157]:

$$n_f = \sqrt{n_s \cdot n_0}. \quad (3.20)$$

Since the surrounding medium tends to be air, i.e.  $n_0=1$ , the requirement for zero reflectance is that the chosen film has a refractive index equal to the square root of the substrate index. In the case of the material used in this work, the substrate

index is replaced by the effective refractive index of the ridge facet material, i.e.  $n_{eff}=3.201$ , therefore a suitable material would be required to have a refractive index in the region of  $n_f=1.789$  at 1550 nm. Practical candidates available in our department would be  $ZrO_2$  with  $n=2.111$  [158],  $TiO_2$  with  $n=2.460$  [159] and  $SiO_2$  with  $n=1.440$  [160]. Reflectance values of the order of  $10^{-3}$  have been reported using such single-layer films [161]. However, as the indices of these materials do not exactly match that of the index required, single-layer films with zero reflectance cannot be readily fabricated.

### 3.12.2 Multi-layer Coatings

By employing multi-layer films, it is possible to further minimise the reflectivity and also the bandwidth, thus they have driven many researchers to optimise coatings that can be sufficiently tailored to a particular application requirement. For double-layer coatings it can be shown, from transfer matrix theory, that at normal incidence with quarter-wavelength thick layers, the reflectance can be expressed as [157]:

$$r = \left( \frac{n_0 n_{f2}^2 - n_{eff} n_{f1}^2}{n_0 n_{f2}^2 + n_{eff} n_{f1}^2} \right)^2, \quad (3.21)$$

where  $n_{f1}$  and  $n_{f2}$  are the refractive indices of the upper and lower films respectively.

Using equation (3.21), zero reflectance can be obtained when  $n_0 n_{f2}^2 = n_{eff} n_{f1}^2$ , or

$$\frac{n_{f2}}{n_{f1}} = \sqrt{\frac{n_{eff}}{n_0}}. \quad (3.22)$$

Again assuming that the surrounding medium is air with  $n_0=1$ , then for zero reflectance, the ideal ratio of the two films is  $n_{f2}/n_{f1}=1.7930$ . Two films that may approximately satisfy this condition are  $TiO_2$  with  $n=2.460$  and  $SiO_2$  with  $n=1.440$ , giving a ratio of  $n_{f2}/n_{f1}=1.708$ , therefore these films were chosen as the layers to be used in this work.

### 3.12.3 TiO<sub>2</sub> and SiO<sub>2</sub> Double-layer Coating Design

A commercially available software package was used to optimise the design of the coatings as a function of parameters such as wavelength, refractive index and layer thickness. The first step in such a design was to define the substrate material index, in this case the effective refractive index of the facet material, i.e.  $n_{eff}=3.201$  at 1550 nm. Next, the first layer material parameters, i.e. TiO<sub>2</sub>, were entered as a function of the wavelength range of interest. Then the second layer material parameters, SiO<sub>2</sub>, were inserted. As a starting point, the quarter-wavelength thicknesses were entered. The software then performed a refinement of these thicknesses in order to give the desired reflectance at the wavelength of interest, i.e.  $r=0$  over the wavelength range of 1500 to 1600 nm. After several iterations, optimised thicknesses (for minimal  $r$ ) of TiO<sub>2</sub>=127 nm and SiO<sub>2</sub>=227 nm were obtained. The resultant theoretical reflectance curve is shown in Fig. 3.39

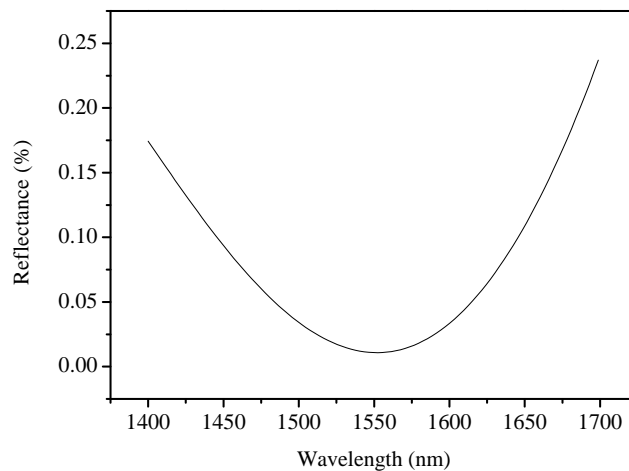


FIGURE 3.39: Simulated reflectance of a TiO<sub>2</sub>/SiO<sub>2</sub> double-layer film versus wavelength. Thicknesses are determined at 1550 nm, and are SiO<sub>2</sub>=227 nm and TiO<sub>2</sub>=127 nm.

From this curve, a theoretical minimum reflectance of  $r=0.011\%$  at 1552 nm is observed. It is known that the uncoated facet reflectivity is  $r=27.45\%$ , thus it is evident that such AR coatings would give a vast reduction in reflectance.

### 3.12.4 Thin Film Deposition Methods and Process Development

After the theoretical design had been completed, the next task was the application of the coatings. Various methods of depositing the coating materials currently exist, for example, e-beam evaporation and sputter deposition. In general, e-beam evaporation tends to be the favoured method of deposition with reflectance values of  $r < 10^{-4}$  having been reported for a  $\text{TiO}_2/\text{SiO}_2$  double-layer deposited on a GaInAs/AlGaInAs semiconductor laser amplifier [162]. However, more recent work has shown that magnetron sputtering may also produce high quality dielectric films at low substrate temperatures (around  $100^\circ\text{C}$ ) [163]. This is mainly due to greater control over the sputtering process, as well as associated adhesion and uniformity benefits. Due to the above reasons and machine availability, facet coatings employed in this work were deposited using magnetron sputtering.

#### 3.12.4.1 Basics of Sputter Deposition

Sputtering is a physical vapour deposition (PVD) technique of thin film application, in which material is removed from the surface of a pre-determined target and re-deposited onto a substrate to form a uniform coating. The atoms at the target surface are subjected to bombardment from ions of the inert gas used in the sputtering process, usually Argon. When these ions impact upon the target atoms, a transfer of energy takes place in which some of the target species are displaced from the surface and then travel within the chamber to condense on other surfaces, including the substrate.

The atoms that leave the target surface are able to travel to the substrate as both the target and the substrate are contained within a vacuum chamber where the pressure is very low. In order to achieve a high number of fast moving ions, the target is immersed within a plasma. A highly negative voltage is then applied to the target surface in order to attract the positive ions towards the target [164]. The mechanisms are similar to those of RIE, as described previously.

In magnetron sputtering, strong magnets are placed behind the target material in order to trap electrons close to the target surface and effectively increase their mean free path. These excess electrons lead to a more dense plasma and hence enable higher deposition rates at lower RF powers. This also allows the plasma

to be sustained at lower chamber pressures. As both the coating materials to be sputtered in this work are non-conducting, RF power is applied to the target electrode. The use of a reactive gas, such as oxygen, may also be used as well as the inert sputtering gas in order to improve the stoichiometry of the deposited film (mainly for  $\text{TiO}_2$ ). This technique is known as reactive sputtering with advantages including improved control over compositional, structural and optical characteristics [163]. It also allows for an increased resistance to water absorption, compared to films grown without oxygen.

#### 3.12.4.2 Sputter Deposition Process Development

In this work, a conventional RF magnetron sputter system was used to deposit  $\text{SiO}_2$  and  $\text{TiO}_2$  from 99.99% pure, 200 mm diameter targets. For initial film characterisation, small Si test pieces patterned with half of the area masked by S1818 photoresist were used. The reason for this was so that both ellipsometric and Dektak surface profiler measurements could be taken post deposition via lift-off processing. For the deposition runs, the process chamber was pumped down to a base pressure of below  $4 \times 10^{-6}$  mbar prior to processing. The sputtering gas mixture of Ar/ $\text{O}_2$  (with 10%  $\text{O}_2$ ) was then introduced to the chamber via a mass flow controller (MFC) at a constant flow rate of 35 sccm giving a chamber process pressure of 3 mtorr (2251 mbar). Firstly, the  $\text{SiO}_2$  film was deposited for varying times with 200 W being applied to the target. The samples were measured using both a Dektak surface profiler and a multi-angle ellipsometer with a laser emission wavelength of 632.8 nm. The measured film thickness results, with linear fitting, are shown in Fig. 3.40.

A linear fit to the data yields a deposition rate of around 3.6 nm/min. Therefore in order to deposit 227 nm, a deposition time of 63 min is required. The refractive index of the  $\text{SiO}_2$  was also measured as a function of deposition time and is plotted in Fig. 3.41. These values are within the acceptable limits for the refractive index of  $\text{SiO}_2$  taking into account any possible measurement errors.

Similar deposition runs were carried out for the  $\text{TiO}_2$  film, however, it was found that the deposition rate using 200 W was rather low at 0.6 nm/min. Therefore, the power was increased to 400 W, and from the linear fitting curve analysis a deposition rate of around 1.16 nm/min was obtained, as shown in Fig. 3.42. Again,

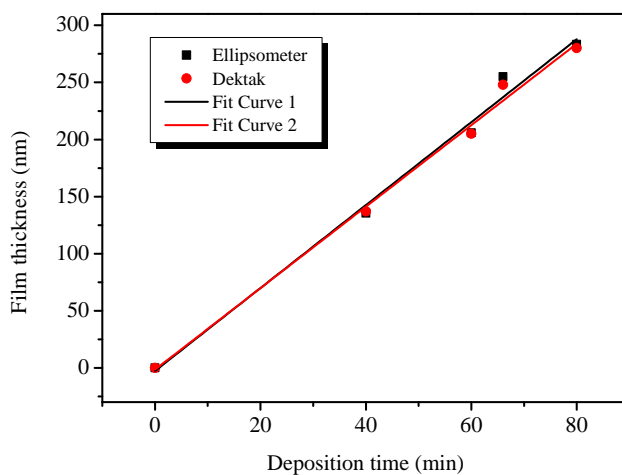


FIGURE 3.40: Thicknesses of  $\text{SiO}_2$  deposited on patterned Si test pieces as measured by Dektak surface profiling and ellipsometry. Also shown are the linear fitting curves to each data set, indicating a deposition rate of around 3.6 nm/min.

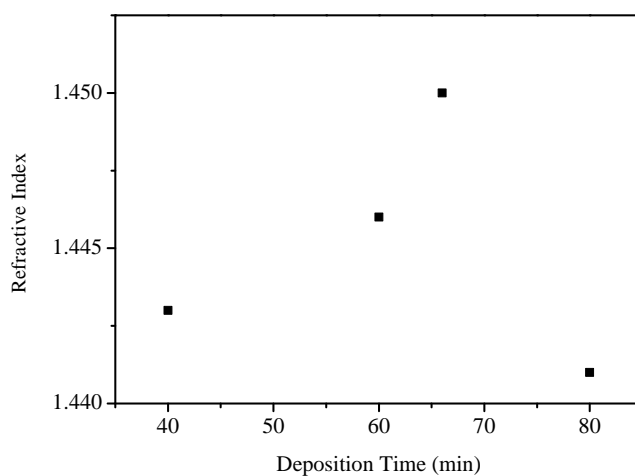


FIGURE 3.41: Refractive index of  $\text{SiO}_2$  deposited on patterned Si test pieces as measured by ellipsometry.

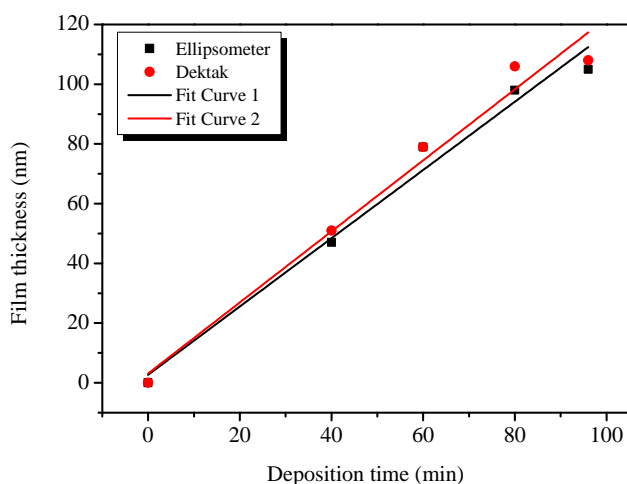


FIGURE 3.42: Thicknesses of  $\text{TiO}_2$  deposited on patterned Si test pieces as measured by Dektak surface profiling and ellipsometry. Also shown are the linear fitting curves to each data set, indicating a deposition rate of around 1.16 nm/min.

refractive index measurements were performed on the films and the results are plotted in Fig. 3.43.

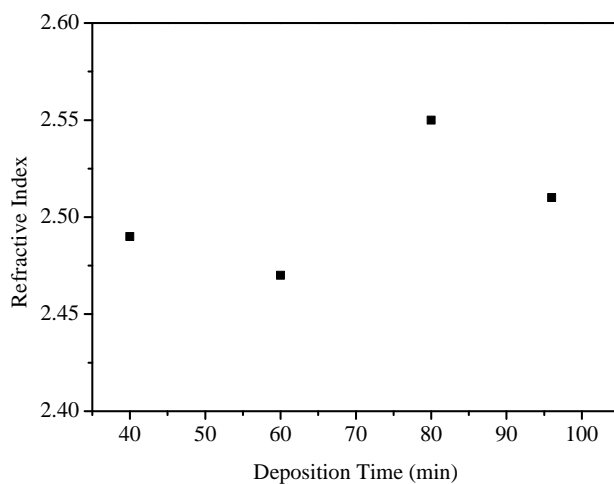


FIGURE 3.43: Refractive index of  $\text{TiO}_2$  deposited on patterned Si test pieces as measured by ellipsometry.

### 3.12.5 Coating Performance

A commonly used technique for determining the reflectivity of a coated laser facet is based on the Hakki-Paoli gain spectra analysis [165], and is known as

the Kaminow-Eisenstein method [166]. The single facet coated laser is biased at the threshold current of the same uncoated laser, then a comparison of the spectra can be made. From basic laser theory, the spectra consist of the the gain curve of the medium modulated by the FP fringes. We can define the modulation index,  $m$ , as:

$$m = \frac{I_{max} - I_{min}}{I_{max} + I_{min}}, \quad (3.23)$$

where  $I_{max}$  and  $I_{min}$  are the maximum and minimum intensities of the spectrum respectively. However, it is also known that [166]:

$$m = \frac{2|a|}{1 + |a|^2}, \quad (3.24)$$

and

$$r_2 = |a|^2 r_1, \quad (3.25)$$

where  $a$  is the round trip amplification factor, therefore the reflectivity of the coated facet,  $r_2$ , can be now calculated. Note, at threshold  $a \simeq 1$ .

Fig. 3.44 shows the output spectrum of a fabricated 1 mm long single-mode FP ridge waveguide uncoated laser diode biased at 29 mA, i.e. at threshold. From this spectrum, a modulation depth of  $m=0.9958$  is obtained. Note for an ideal laser,  $m=1$ .

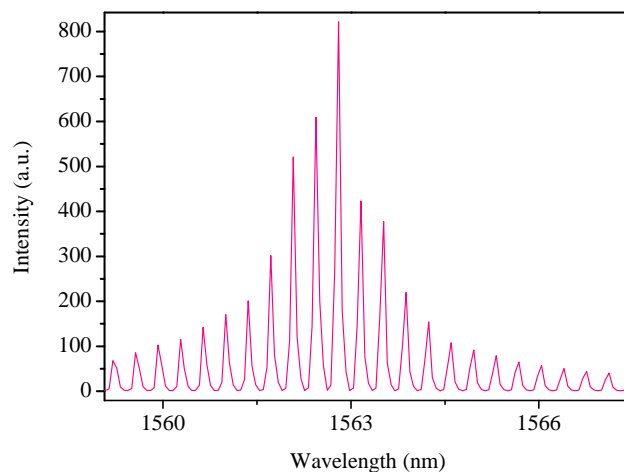


FIGURE 3.44: Output spectrum of the uncoated laser diode at room temperature biased at 29 mA. Here,  $m=0.9958$ .

After coating one facet of the device with the parameters detailed previously, the same laser spectrum was measured again, also biased at 29 mA. Fig. 3.45 shows a plot of the spectrum obtained, where the modulation depth has decreased to  $m=0.2174$ . One can now use equations 3.24 and 3.25 to determine the reflectivity of the coated facet, which works out to be  $r_2=0.33\%$ . It was therefore deduced that the designed coatings are capable of achieving a facet reflectivity sufficient for the devices in this research work, i.e. around  $r=10^{-3}$ .

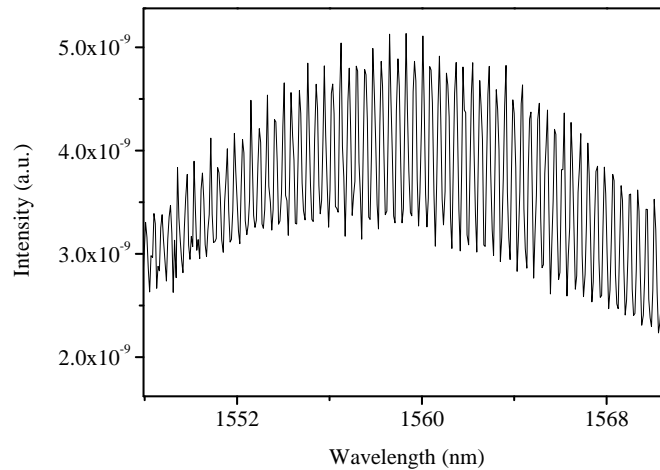


FIGURE 3.45: Output spectra of the coated laser diode at room temperature biased at 29 mA. Here  $m=0.2174$ .

### 3.13 Chapter Summary

In this chapter, the fabrication technology and basic material characterisation results were presented. The chapter began by introducing the active/passive integration platform used in this work: sputtering induced QWI. Wavelength shifts of  $>100$  nm were obtained at an anneal temperature of  $675$  °C. The technique of selected intermixing in selected areas was also presented, wherein varying degrees of wavelength shift are achievable across a chip using a single anneal step. This ability is vital in the realisation of monolithically integrated photonic circuits where several band-gap sections are required.

The key steps used in the fabrication process were then discussed, focusing on the processes where vast development activities were undertaken. A successful reactive ion etching process, based on  $\text{CH}_4/\text{H}_2/\text{O}_2$ , was developed for etching waveguides in

the AlGaInAs material. The process also makes use of the the normally undesirable oxidation of aluminium containing layers to great effect in the realisation of a dry etch stop layer for in situ etch depth and uniformity control.

Subsequent chapter sections focused on basic characterisation of the MQW material, as well as the fabrication of simple devices, allowing for confirmation of the quality of both the material itself and the fabrications processes. Using the intermixing technique described above, passive waveguides were fabricated and measured to determine the waveguide propagation losses, which were found to be around  $4.25 \text{ cm}^{-1}$  at 1550 nm for the TE polarisation state. Gain guided and ridge waveguide laser analysis resulted in a threshold current density of an infinitely long device of  $J_{\infty}=260.5 \text{ Acm}^{-2}$ , and a characteristic temperature value of  $T_0=94 \text{ K}$ , respectively, demonstrating that the material is of good quality. The effect of intermixing in the proximity to laser devices was also assessed, where it was found that both optical and electrical properties begin to deteriorate when located within  $60 \mu\text{m}$  from any intermixing sections. The relaxation oscillation frequency of the material was also ascertained, allowing for a carrier lifetime value of  $\tau_s=273 \pm 16 \text{ ps}$ , to be deduced.

Next, the experimental characterisation of the carrier induced electro-optic effects was presented, where it was found that, as expected from theory, maximum values of  $\Delta n$  occur just above the band-gap energy of the material. Similar work was undertaken for devices with SISA, where equivalent trends were found, only blue shifted in wavelength. In order to reduce any undesired reflections from device facets, a double-layer antireflection process, based on sputtered  $\text{TiO}_2/\text{SiO}_2$  thin films, was developed, resulting in a reduction in facet reflectivity from 27.45% to 0.33%.

# Chapter 4

## Mode-Locked Ring Laser Results

### 4.1 Introduction

This chapter gives a detailed overview of the characterisation of the fabricated semiconductor mode-locked ring lasers. It begins by presenting the power splitting ratio measurements made on the evanescent field couplers, followed then by the ring laser results, both under continuous wave and mode-locked operation.

### 4.2 Evanescent Field Coupler Measurements

The operation of the outcoupling element is paramount to the performance of the ring laser and must be confirmed prior to their inclusion in the device. In order to reduce any effects of undesirable alignment and coupling losses during measurements,  $300\ \mu\text{m}$  long,  $800\ \text{nm}$  gap width couplers were fabricated with  $150\ \mu\text{m}$  long integrated contacted sections on each input/output arm such that they may be employed as both sources of amplified spontaneous emission and integrated photodiodes, as detailed in Fig. 4.1. A current source was used for carrier injection to produce spontaneous emission from one contact, that was then split by the coupler and collected by the integrated photodiodes using a pico-ammeter and micro probes. I-V curves were taken for all four contacts to ensure their resistances were similar. It is assumed that the couplers are relatively robust against small variations in wavelength, therefore they may be assessed accurately in this

manner. The results of the characterisation, when each contact is forward biased with 10 mA in turn, are detailed in Table 4.1

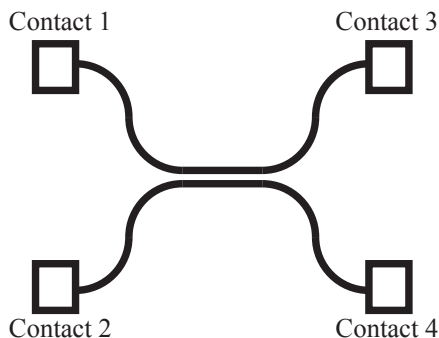


FIGURE 4.1: Schematic of an evanescent field coupler used for splitting ratio characterisation.

TABLE 4.1: Measured evanescent field coupler splitting ratio results

Contact with 10 mA	Contact 1	Contact 2	Contact 3	Contact 4
Contact 1	-	-	2.331 $\mu\text{A}$	2.478 $\mu\text{A}$
Contact 2	-	-	2.469 $\mu\text{A}$	2.330 $\mu\text{A}$
Contact 3	2.479 $\mu\text{A}$	2.329 $\mu\text{A}$	-	-
Contact 4	2.330 $\mu\text{A}$	2.480 $\mu\text{A}$	-	-

The results show a nominal 50% splitting ratio as designed, therefore the couplers were deemed suitable for employment in the ring lasers.

### 4.3 Ring Laser Results

In this section the measurement results from the ring lasers are detailed and discussed. Optical power versus injected current and absorber bias voltage characterisation for both propagation directions was performed in order to investigate the directional properties of the devices. Simultaneous optical, RF and autocorrelation traces were recorded for each device configuration as a function of biasing, allowing for the determination of the mode-locking parameter space and quality. Two devices were measured, one with 1% long absorbers and one with 2.5% long absorbing sections. This allowed for a comparison between absorber lengths and also single versus dual SA configurations, in terms of mode-locking region and performance. In the case when only a single absorber was reverse biased, the other was forward biased at the same current density as the rest of the gain section. The

electrical isolation resistance between the gain and absorber sections was measured to be around  $1.6\text{ k}\Omega$ , even with the highly doped cap intact. A SEM micrograph of a fabricated device, with the layout of the ohmic contacts made to the structure, is shown in Fig. 4.2. This particular device has dual 2.5% SAs.

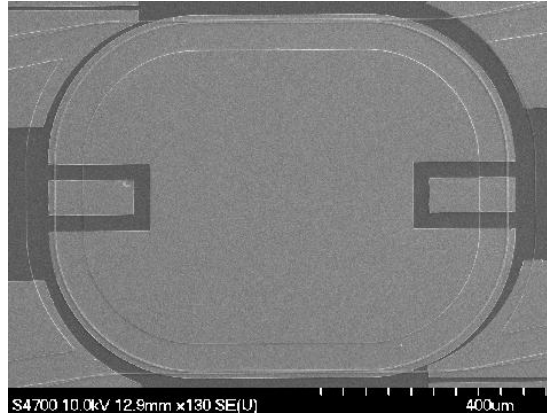


FIGURE 4.2: SEM image of a fabricated 36 GHz mode-locked ring laser with dual couplers and dual 2.5% absorbers.

### 4.3.1 Optical Power

Optical power versus injected current (L-I) plots were taken via lensed optical fibres for both propagation directions as a function of absorber voltage, with the results of the dual biased 1% SA configuration, when biased at 0 and 3.0 V, being shown in Fig. 4.3. For the the L-I curves at 0 V, it can be seen that the device exhibits a switching behaviour between the clockwise (CW) and counter clockwise (CCW) propagating modes, indicating a clear bistability. This behaviour is consistent with that found in [167], and the theory of Sargent, which states that bidirectional ring lasing will not occur, even in the absence of spatial hole burning. Unidirectional lasing is the most likely regime of operation [168].

However, the application of a reverse bias voltage on the SAs modifies the L-I curves and their unidirectional properties. In the case where the SA is reverse biased at -3.0 V, the threshold current increases from around 120 mA to 155 mA. The output power in both directions then rises equally until around 275 mA, i.e. bidirectional behaviour. As the current is increased further, the CW power increases and the CCW decreases, possibly indicating some quasi-unidirectional behaviour. Above 300 mA, both directions have similar powers, showing that the laser is again emitting bidirectional. This behaviour is consistent with the theory of CPM in

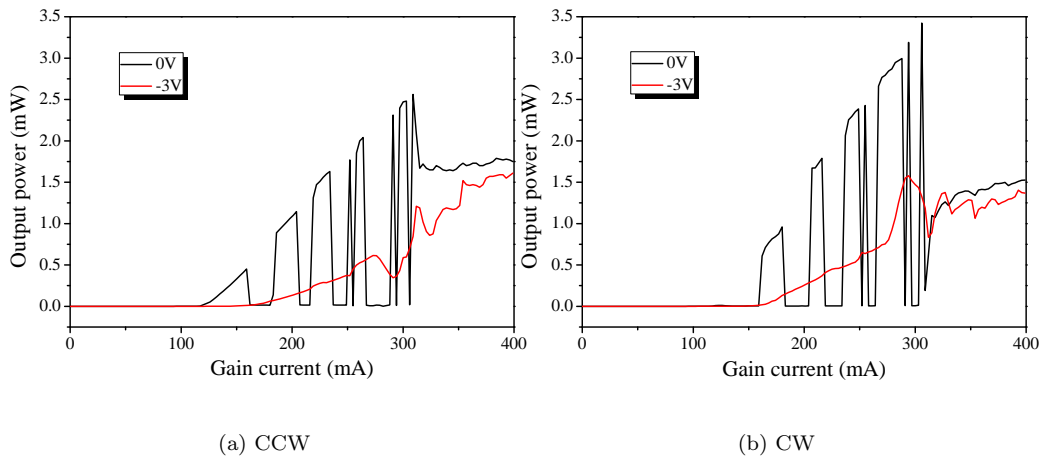


FIGURE 4.3: Measured L-I characteristics for both directions when  $-3.0\text{ V}$  is applied to both 1% long saturable absorbers.

ring lasers, i.e. that the minimum in threshold gain is achieved when the pulses overlap in the absorber because the intracavity loss is sharply reduced for that condition [112].

For full characterisation of the mode-locking parameter space and quality, simultaneous measurements of optical spectra, RF spectra and second harmonic generation (SHG) intensity autocorrelation were performed using the set-up as shown in Fig. 4.4.

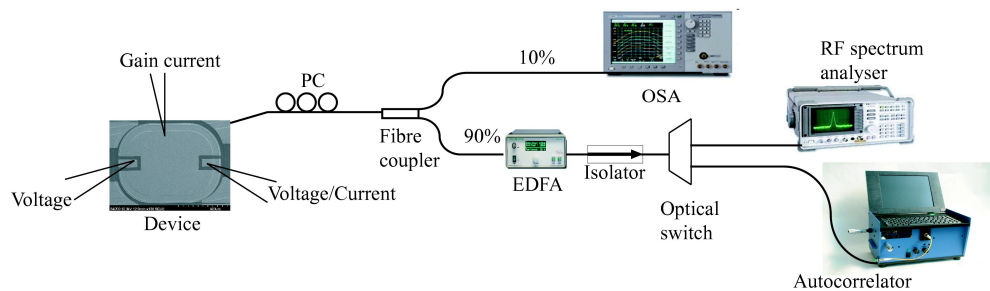


FIGURE 4.4: Characterisation set-up for the mode-locked ring lasers.

The light is coupled out from the device using a single-mode lensed fibre with in line polarisation control (set to TE). The signal is then split using a fused fibre coupler with 10% going to a  $0.07\text{ nm}$  resolution OSA and 90% going through a dispersion compensated EDFA, optical isolator and then optical switch to either the RF analyser or autocorrelator. The pulse durations were obtained in the

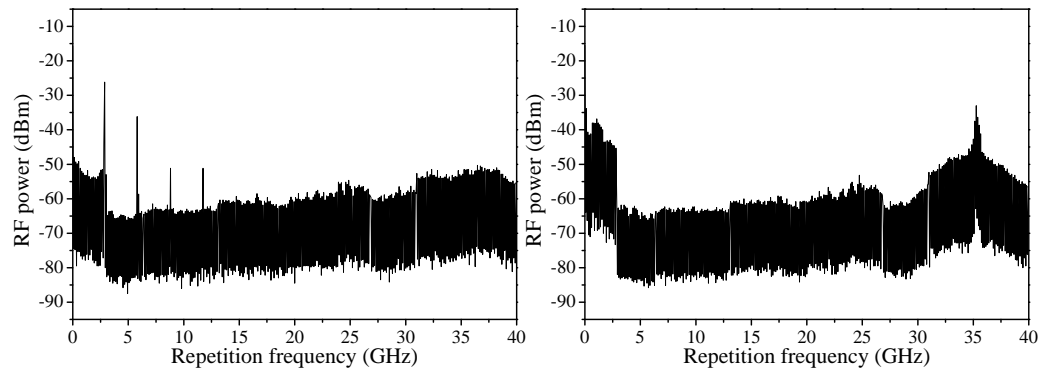
background free autocorrelator by use of a photomultiplier tube recording the the intensity of the signal generated in the SHG crystal. Precise control of the polarisation in the crystal is necessary as any deviations lead to a dramatic drop in the signal and the peak/pedestal ratio.

### 4.3.2 RF Spectra

For each device, both full scale (VBW=10 KHz, RBW=1 MHz, span=40 GHz) and more detailed (VBW=1 KHz, RBW=100 KHz span=150 MHz) RF spectra were recorded for each measurement point. Fig. 4.5 (a)-(d) show examples of full span RF spectra for various regimes of laser operation, from the 1% dual biased SA laser. These are incomplete mode-locking, self pulsation, mode-locking with self pulsation and of course optimal mode-locking.

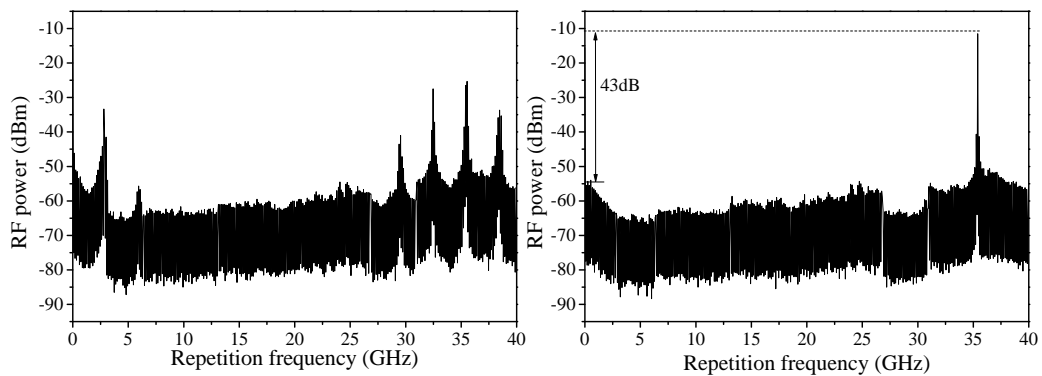
As mentioned previously, optimal mode-locking may usually be identified when the RF spectrum ER >25 dB. Self pulsation is defined as being the instabilities in passively mode-locked devices when the energy of the pulses is unstable, i.e. there is an amplitude modulation of the pulse train at the relaxation oscillation frequency of the laser [21]. This triggering of the undamped relaxation oscillations is an unfortunate side effect of the SA. One must find a compromise between the ratio of the saturation energies in the gain and absorber sections to decrease self pulsation effects, whilst still achieving optimal mode-locking. Fig. 4.5 (a) details the RF spectrum in the self pulsation regime, where the relaxation oscillation frequency peak is at 2.8 GHz, with its harmonics evident. Fig. 4.5 (b) shows the RF spectrum of the device when the mode-locking is incomplete, i.e. the fundamental peak is less than 25 dB above any other components in the spectrum. There is also the presence of some low frequency noise. Fig. 4.5 (c) illustrates the case when the device is mode-locking incompletely along with self pulsation such that there is a beating between the fundamental peak and the relaxation oscillation frequency. Fig. 4.5 (d) depicts the situation where optimal mode-locking is occurring, with the fundamental RF peak at 35.4 GHz, around 43 dB above any other components in the spectrum. Finally, a detailed scan of the optimal mode-locking case, where the RF 3 dB linewidth is 1.4 MHz, is shown in Fig. 4.5 (e).

Once all of the device configurations were characterised in the RF domain, contour maps of the mode-locking performance were made. Fig. 4.6 details the regimes of laser operation observed for the four absorber configurations from the clockwise



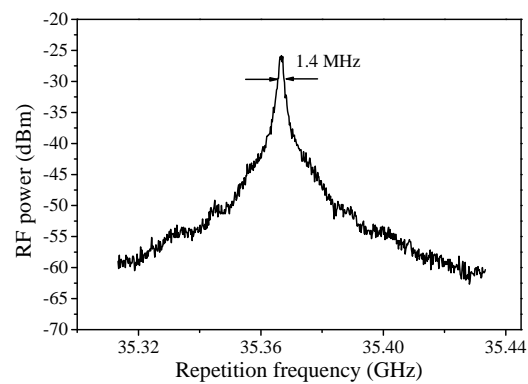
(a) Self pulsation

(b) Incomplete mode-locking.



(c) Mode-locking with self pulsation.

(d) Optimal mode-locking.



(e) Optimal mode-locking, detailed.

FIGURE 4.5: Examples of measured RF spectra for various regimes observed for the 1% dual biased laser.

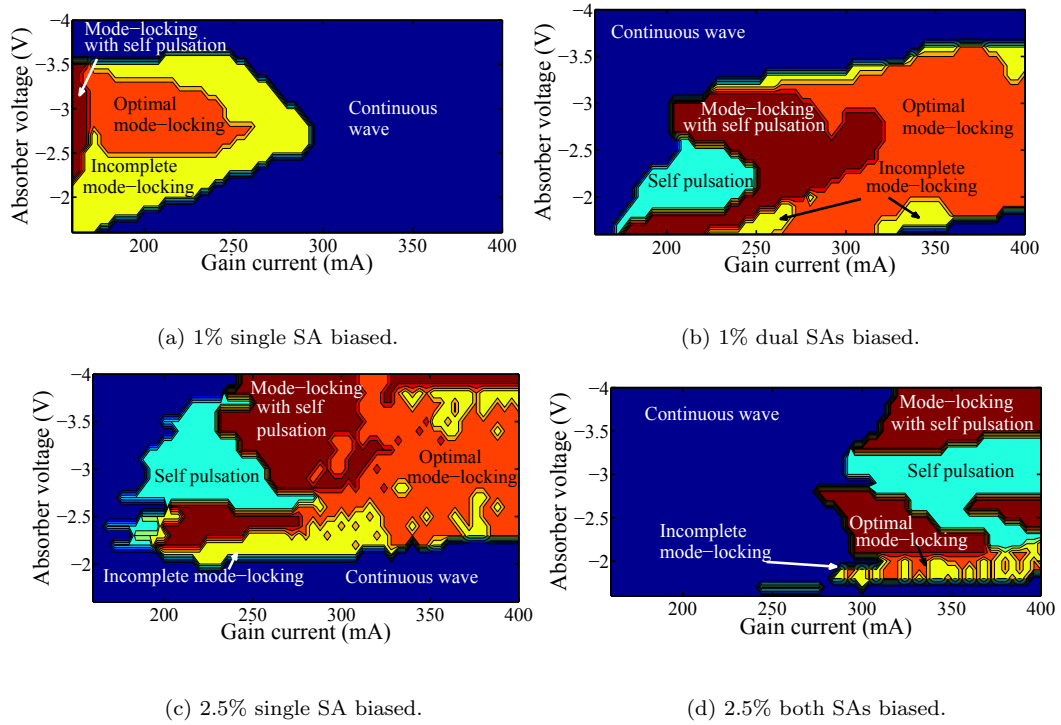


FIGURE 4.6: Regimes of laser operation as a function of gain current and absorber bias for the various configurations.

direction. For the 1% single biased SA, there is a well defined area of mode-locking achieved for a gain current range of around 170 to 250 mA and SA bias voltage range of -2.5 to -3.4 V. There seems to be no evidence of self pulsation for the 1% SA in the measurement region. The dual biased 1% SA map also shows a stable region of mode-locking, even larger than the single biased case. This is most probably due to the predicted advantages of dual absorbers by Yu, as described in Chapter 2. The regions for the dual biased 1% and single biased 2.5% seem quite similar, however, the dual 1% laser does have less, or indeed, no sporadic regions of mode-locking with self pulsation and incomplete mode-locking within the optimal mode-locking area. The device with the dual biased 2.5% SAs shows very small regions of optimal mode-locking and large areas of self pulsation, most likely due to total length of the SA sections being too long, and thus  $E_a^{sat}$  being too large to fulfil the mode-locking condition that  $E_g^{sat} > E_a^{sat}$ . In terms of the widest mode-locking region, it seems that the 1% dual biased case gives the optimum situation. It is also observed that for the 1% absorber device, depending on whether one or both SAs are biased, the full current range may exhibit an optimal mode-locked state for voltages of between -2.5 V to -3.5 V. This is most likely due to the fact that by biasing both absorbers leads to higher losses in the cavity and therefore

shifts the mode-locking regions to higher gain currents.

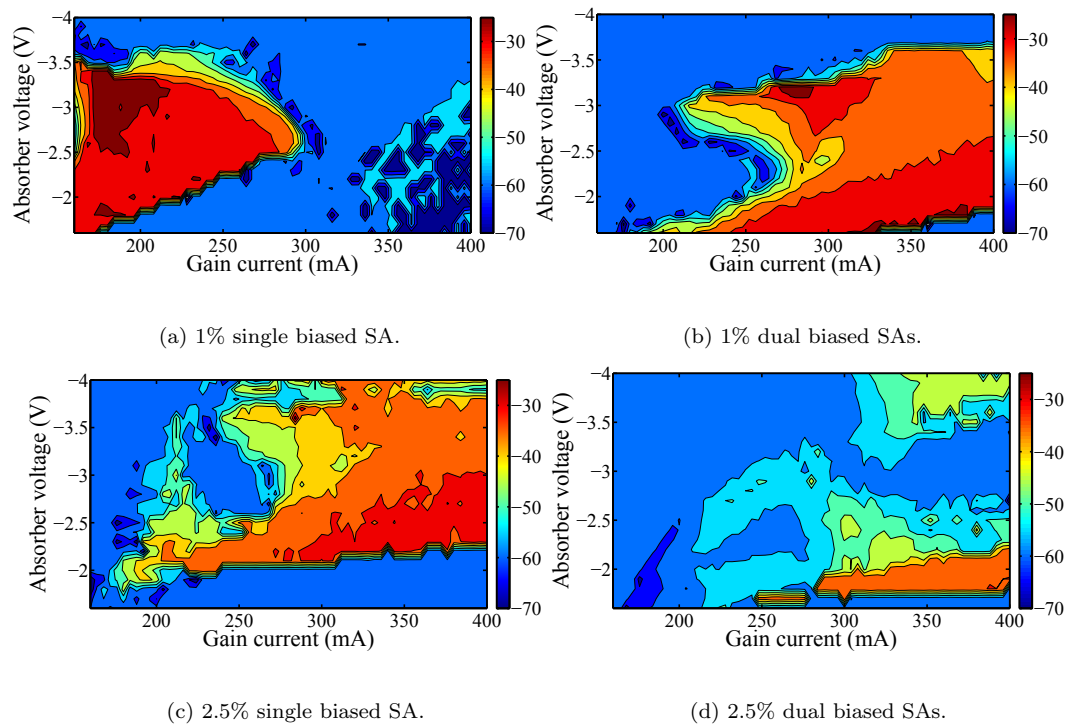


FIGURE 4.7: Contour plots of the peak power of the fundamental RF peak as a function of gain current and reverse bias voltage for the four laser configurations. The colourbar legend shows the peak RF power in dBm.

Fig. 4.7 shows contour plots of the peak RF power as a function of gain current and reverse bias voltage for each device configuration. The 1% single biased situation shows a well defined region of high RF power peaking at around -25 dBm for currents between 168 to 220 mA and voltages of -2.5 to -3.4 V. Both the 1% dual biased and 2.5% single biased cases again show similar regions of high RF power to each other, however, one can clearly see that the dual 1% case exhibits a more consistent area of high RF power. The dual 2.5% case seems to show the least encouraging range of high RF power, as expected from the previous mode-locked region plots. The RF 3 dB linewidths were also plotted in this manner, and are shown in Fig. 4.8. Again, they seem to link well with the defined regions of laser operation from Fig. 4.6, and also the RF power plots. Therefore, in terms of RF performance, it would appear that the single 1% absorber situation is superior. All device configurations here, especially the single and dual 1% long absorber cases, meet with the requirement, as defined by Bandelow and Kaiser, that the RF spectrum ER should  $>25$  dB.

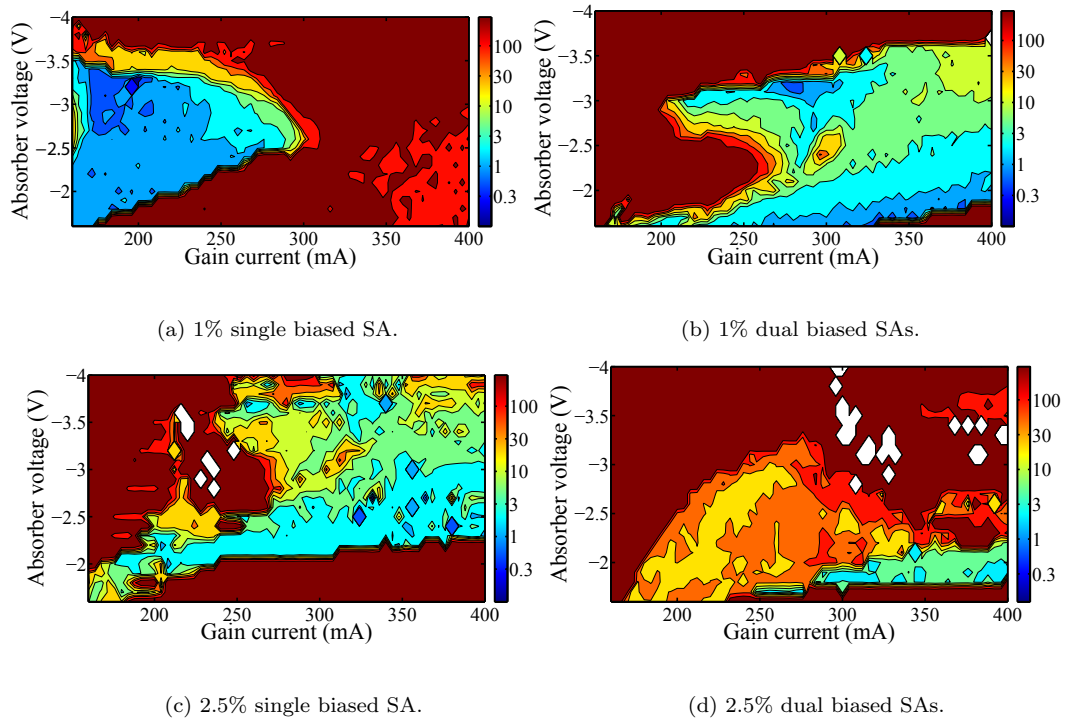


FIGURE 4.8: Contour plots of the 3 dB RF linewidth of the fundamental RF peak as a function of gain current and reverse bias voltage for the four laser configurations. The colourbar legend shows the 3 dB RF width in MHz. The white areas show regions where the RF depth is less than 4 dB.

The repetition rates for the optimal mode-locking range of all devices were also recorded and those of the 1% single biased device are shown in Fig. 4.9. The trends are typical of all devices. There is a clear tuning of the repetition frequency by varying the gain current/absorber bias voltage (around 200 MHz). For a fixed voltage, the frequency decreases as the current is increased. For a fixed current value, the frequency increases as the voltage is increased. These trends agree well with the theory of Arahira [169] and the observations made in [123], where the tuning is led by gain/absorption saturation effects rather than that of refractive index change [93]. Operating with a low unsaturated gain, the repetition frequency of the laser decreases with increasing pulse energy. As the pulse energy increases with gain current, then it follows that indeed the frequency decreases. By increasing the reverse bias voltage, one also decreases the pulse energy and thus increases the repetition rate.

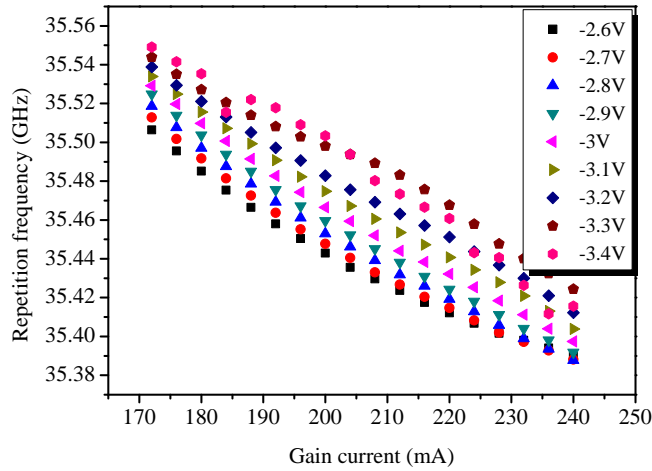


FIGURE 4.9: Repetition rate as a function of gain current and reverse bias voltage for the 1% single biased SA.

### 4.3.3 Optical Spectra

Examples of optical spectra from the 1% dual biased absorber laser, when emitting both single-mode and optimally mode-locked, are shown in Fig. 4.10. For the single-mode case, the operating wavelength is at 1567 nm, with a side mode suppression ratio (SMSR) of >23 dBm. On inspection of the mode-locked trace, one can immediately see the difference between the two spectra in as much as it is now wider and the shape is smooth and symmetric. The emission spectrum is altered dramatically, with a large number of cavity modes now lasing due to passive mode-locking. The peak lasing wavelength here is around 1557 nm with a mode spacing of 0.29 nm, commensurate with the round trip cavity frequency of around 36 GHz.

The FWHM values of the optical spectra as a function of gain current and reverse bias voltage for all laser situations are shown in Fig. 4.11. They follow similar trends, in terms of optical bandwidth, to that of the RF plots and of course the mode-locking maps. The typical FWHM when optimally mode-locked is between 6-8 nm for all lasers. The widest spectra and largest mode-locking region are achieved when both the dual 1% absorbers are biased.

Also plotted is how the peak lasing wavelength changes as a function of bias conditions, as shown in Fig. 4.12. It is known that detuning of the energy band edge between the gain and absorber sections plays a vital role in stable mode-locking [170]. Stable mode-locking is only obtainable when there is spectral alignment of

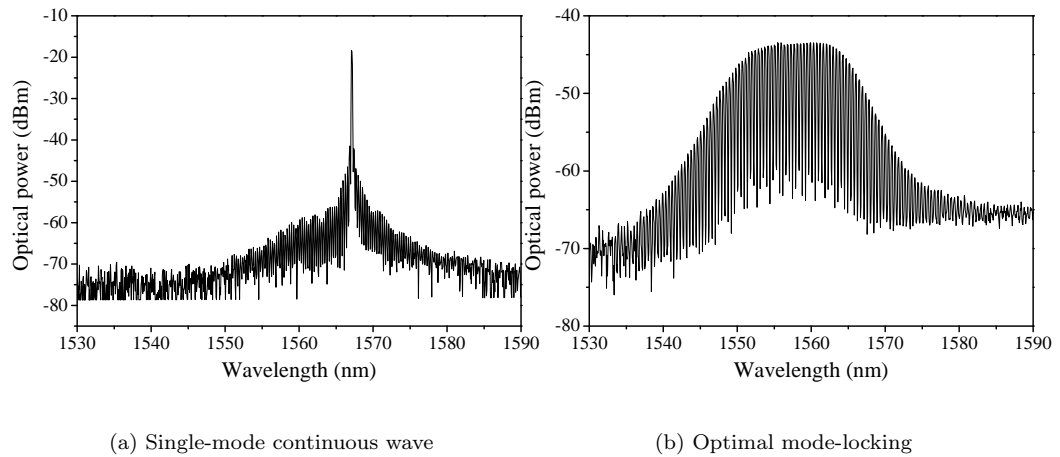


FIGURE 4.10: Examples of optical spectra from the 1% dual absorber laser when operating in the (a) single-mode continuous wave, and (b) optimal mode-locking regimes.

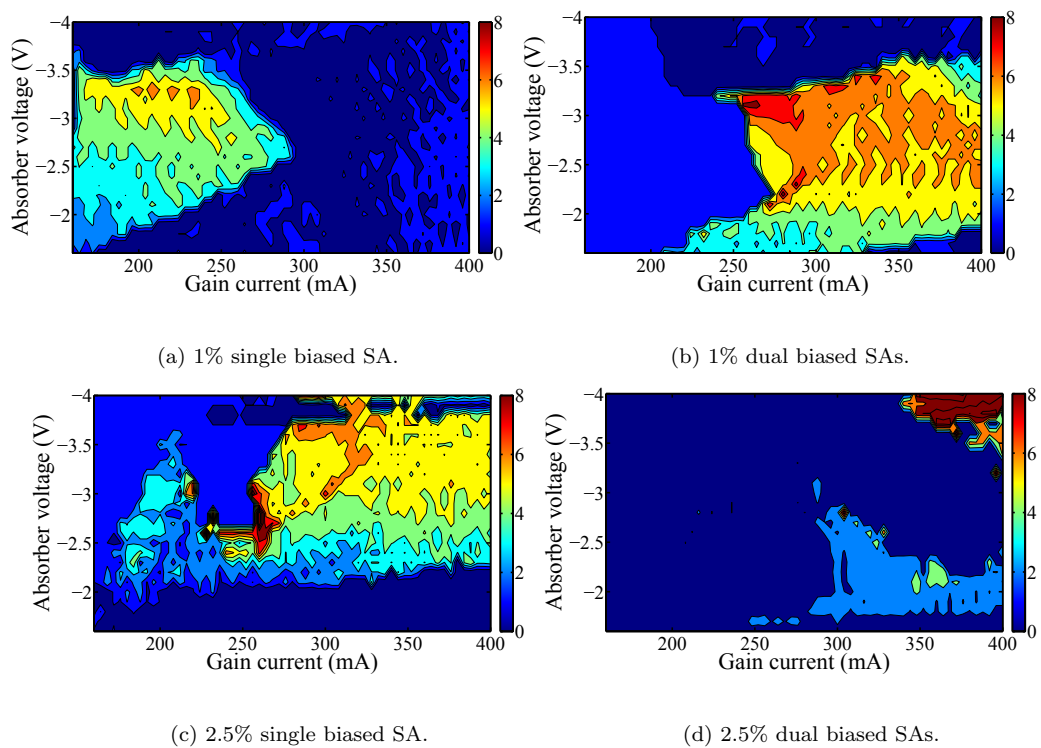


FIGURE 4.11: Optical FWHM as a function of gain current and reverse bias voltage for all devices configurations. The colourbar legend shows the optical FWHM in nm.

the gain and absorption curves. For example, if the band edge of the absorber is sufficiently red shifted with respect to the gain section, then the absorption losses will be high and difficult to saturate. In the opposite case, i.e. when the band edge is blue shifted, the absorption losses will be low and therefore bleached constantly. Only when the gain peak coincides with the absorber band edge should we expect sufficient modulation of the absorption losses, leading to optimal mode-locking. The optimal mode-locking regime for all plots is outlined in black, where it is observed that optimal mode-locking occurs at wavelengths around 1557 nm.

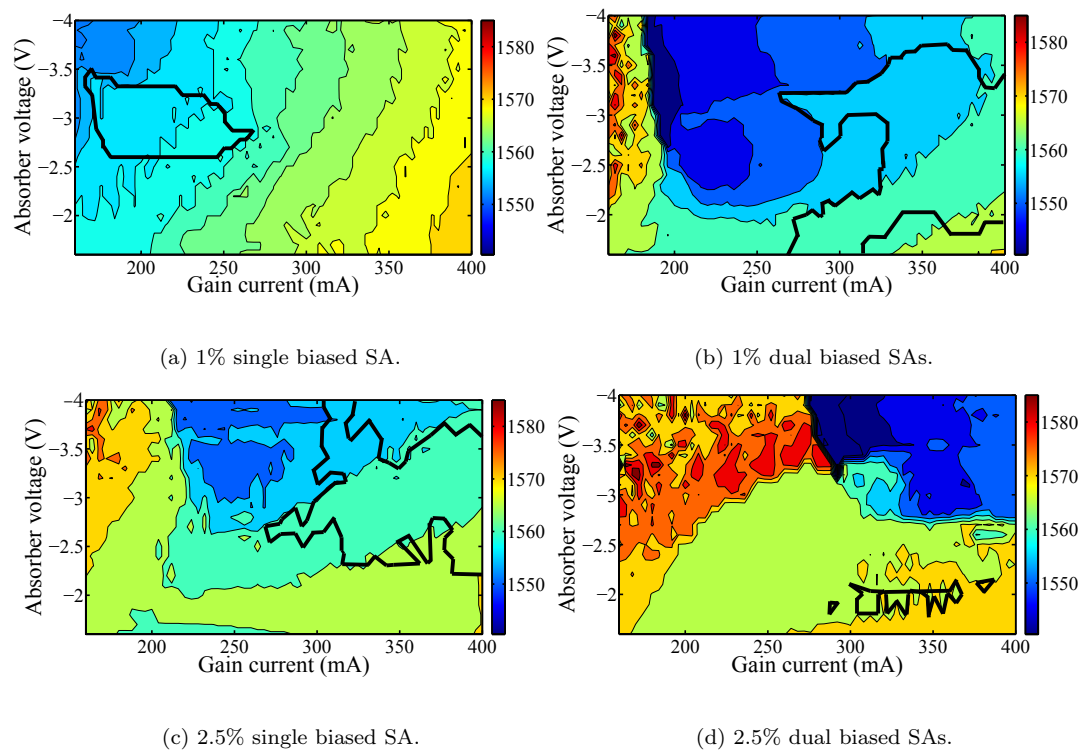


FIGURE 4.12: Peak wavelength function of gain current and reverse bias voltage for all devices configurations. The optimal mode-locking regimes are outlined in black. The colourbar legend shows the peak wavelength in nm

### 4.3.4 Autocorrelation

Background free autocorrelation traces were recorded for each bias point for all absorber configurations, with examples of each regime of operation, from the 1% dual biased SA case, being detailed in Fig. 4.13. The first plot shows the case when the laser is in the self pulsation state such that the pulse is rather wide, and in this case rather noisy. Also, it is apparent that only one pulse is visible in the time window of 160 ps, indicating that the repetition frequency is less than

6.25 GHz, as expected. Fig. 4.13 (b) illustrates the trace when the laser is in the incomplete mode-locking regime where the pulses are emitted at the repetition rate of the cavity round trip. There is also a slight pedestal visible, indicating that the pulses are not of high quality. The third plot is the combination of the self pulsation and incomplete mode-locking case. In this regime of operation the laser output consists of mode-locked pulses with the self pulsation envelope. Finally, there is the situation when the laser is emitting pulses in the optimal mode-locking regime. Compared with the incomplete pulses, one can see that these pulses are higher in intensity, and are also more narrow and well defined with no pedestal evident.

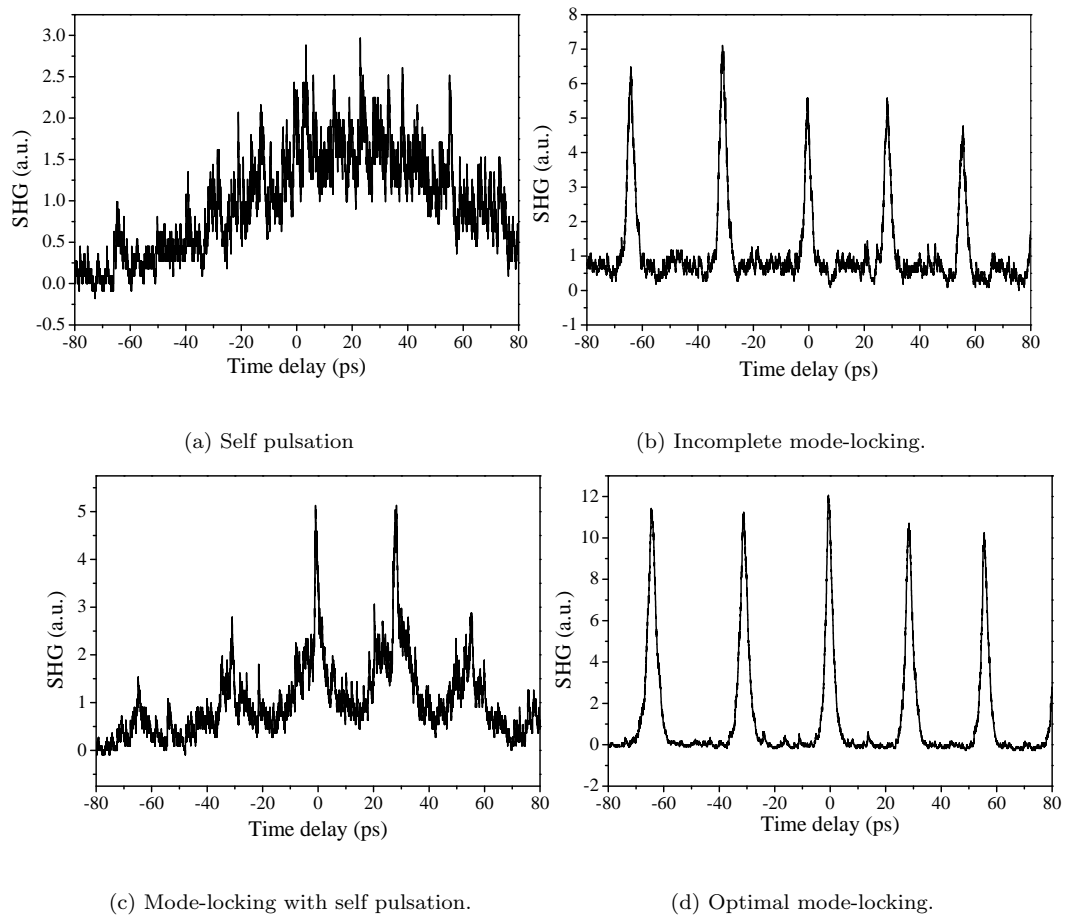


FIGURE 4.13: Examples of measured autocorrelation traces for various laser regimes observed.

In order to determine the approximate pulse width from the autocorrelation width one must determine which fitting is most appropriate. Usually this is  $\text{sech}^2$  for semiconductor lasers, however, it was found that a Lorentzian fitting was best for the pulses emitted from these lasers. As with the RF and optical spectra,

contour maps of the mode-locking pulse widths were generated to clearly see the correlation between pulse width and mode-locking regions. Fig. 4.14 shows the approximate pulse width maps for the four situations. The FWHM values of the Lorentzian fitting to the autocorrelation traces range from 1 to 4 ps.

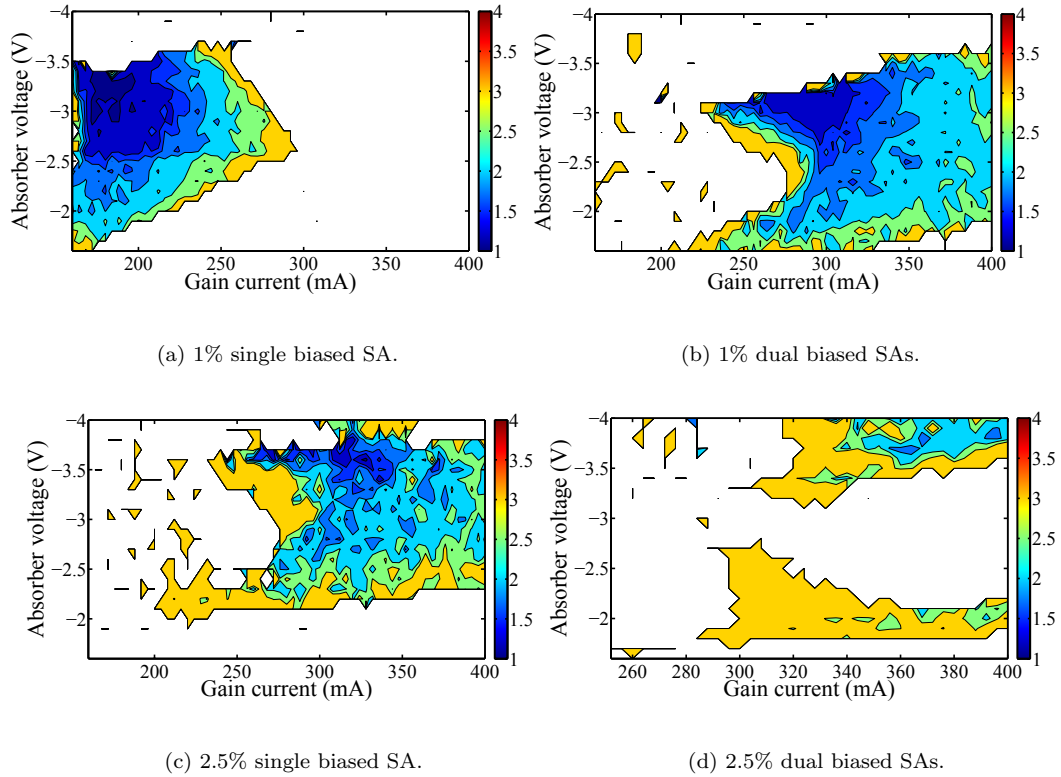


FIGURE 4.14: Lorentzian pulse width as a function of gain current and reverse bias voltage for all devices. The colourbar legend shows the Lorentzian pulse width in ps. The white areas show regions where the pulse width is not measurable, i.e. there is no pulse.

The contour plots show similar trends to those of the RF and optical spectra. Both the 1% single and 1% dual biased situations exhibit large regions of pulse width values of less than 1.6 ps. In terms of absolute narrowest pulse width, the 1% single SA produced pulses of 1.03 ps duration. Fig. 4.15 shows the SHG autocorrelation trace for this case, where the gain section and single absorber were biased at 176 mA and -3.3 V respectively. It has also been shown that in ring lasers, the shortest pulse widths with the highest peak powers are observed when the linewidth enhancement factor ( $\alpha$ -factor) values in the gain and absorber sections are equal [102]. The  $\alpha$ -factor is defined as being a measure of how the real and imaginary parts of the complex refractive index vary with carrier density [34]. As with the RF ER, the device configurations here, apart from the 2.5% dual

biased SA case, meet the requirement defined in Chapter 2 that pulse widths must be  $\leq 1.6$  ps to avoid any inter symbol interference.

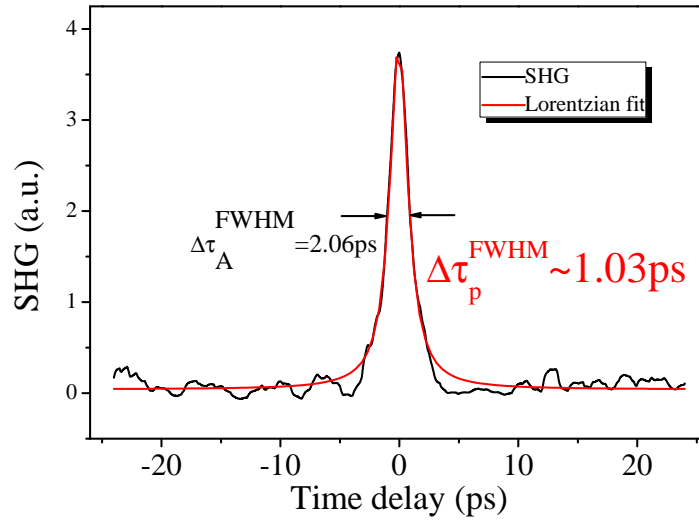


FIGURE 4.15: SHG intensity autocorrelation trace as measured from the 1% single biased SA device with the gain section and single absorber biased at 176 mA and -3.3 V respectively.

The theoretical TBP for a Lorentzian pulse is 0.22, however, for these pulses the typical TBP is around 0.7, indicating the presence of a noticeable chirp in the pulses. Although no temperature dependence measurements were made on these mode-locked devices, FP devices fabricated within the group were found to be mode-locking up to a temperature of 70 °C [171].

### 4.3.5 Optical Harmonic Injection Mode-locking

Well known issues with passively mode-locked lasers are poor timing jitter, due to the lack of a stable reference source, and the inability to synchronise with other components in high speed systems. Optical harmonic injection mode-locking is a technique in which highly stable pulses generated from an actively mode-locked laser (master) are used to lock the pulses from the passively mode-locked device (slave) in order that they may be employed in such high speed applications [109]. The method may be applied to a passively mode-locked laser whose repetition frequency is beyond regular drive electronics speed by using a master laser with a pulse repetition rate corresponding to a subharmonic of the passive mode-locking frequency. The dual 1% single absorber configuration was biased in the optimal mode-locking regime producing pulses at a repetition rate of around 35.5 GHz.

Stabilised optical pulse trains (around 1.6 ps, 3 dBm) from an actively mode-locked fibre laser were coupled through a circulator and then polarisation controller into the CW direction of the ring, as shown in the set-up of Fig. 4.16 .

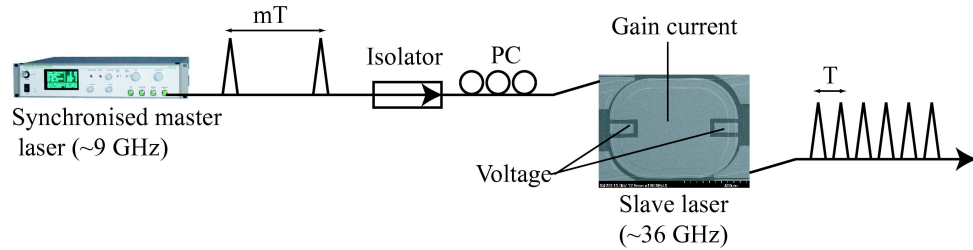


FIGURE 4.16: Characterisation set-up for the harmonic optical injection mode-locking.

The controller was set to match the polarisation of the injection light to the TE polarisation in the slave laser. The repetition rate for the master device was chosen to be a 4<sup>th</sup> subharmonic of the slave mode-locked frequency, i.e. 8.868 GHz. The wavelength of the master laser was slightly detuned to the blue with respect to the center wavelength of the slave laser in order to couple with the modes.

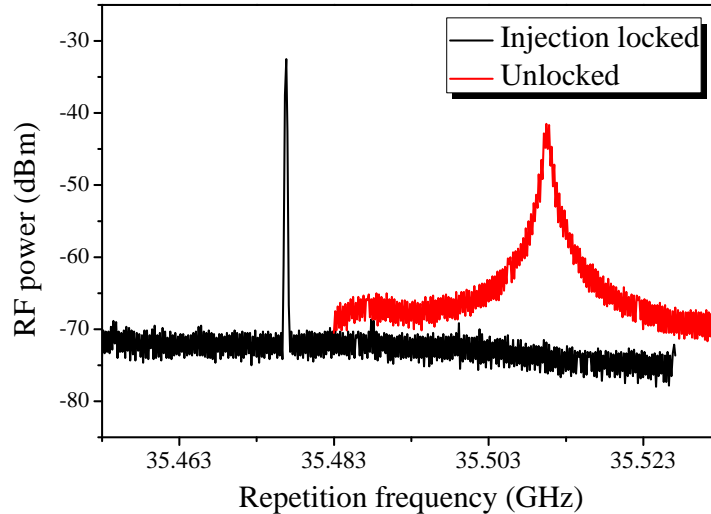


FIGURE 4.17: RF spectra for the optical output of the slave laser with and without optical injection locking. The 3 dB linewidth is 108 kHz with injection and 1.4 MHz without.

Fig. 4.17 shows the RF spectra of the slave laser when in both the unlocked and optically locked states, from the CCW direction. It is observed that when the slave laser locks to the master, the repetition rate of the slave is pulled to the 4<sup>th</sup> harmonic of the master, i.e. a jump of around 34 MHz. Immediately clear from

the plot is the improvement in the 3 dB linewidth, showing a reduction of around 1.4 MHz to 108 kHz, implying a vast improvement in the timing jitter.

The optical spectrum of the locked pulses is shown in Fig. 4.3.5, where it is observed that the part of the spectrum near the wavelength of the master laser increases. However, the main spectrum components are not affected, for example, the mode spacing, indicating that the injected optical pulse train does not significantly influence the pulse characteristics in the wavelength domain. This is because the main effect of optical locking is primarily phase synchronisation [18].

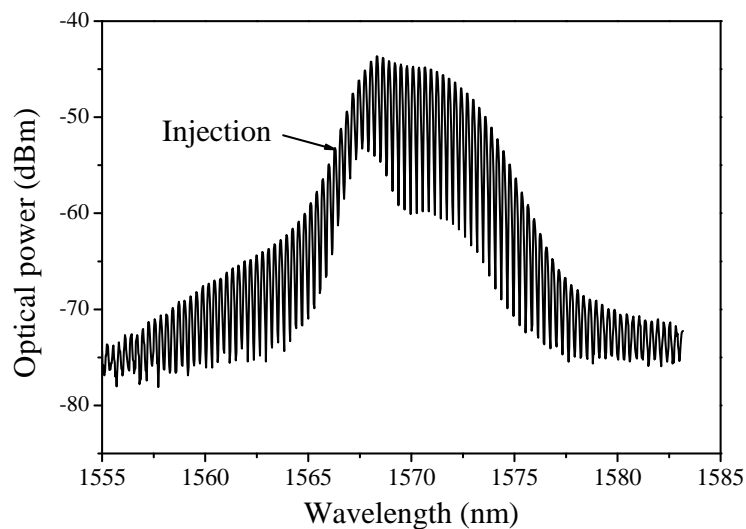


FIGURE 4.18: Optical spectrum for the slave laser with optical injection locking.

The output signal was also detected using a fast optical detector (65 GHz bandwidth) connected to a sampling oscilloscope. When the passive mode-locked devices were unlocked, no traces were observed on the sampling oscilloscope. However, with injection locking, stable pulse trains were observed on the scope. This is because there was synchronisation between the pulses and the reference clock, as the master laser and scope are triggered from the same RF source. Fig. 4.19 (a) shows the optical sampling scope trace, triggered at 8.868 GHz, when the slave laser is unlocked and (b) locked. Such optical injection locking allows for the incorporation of passively mode-locked devices into high speed system type measurements.

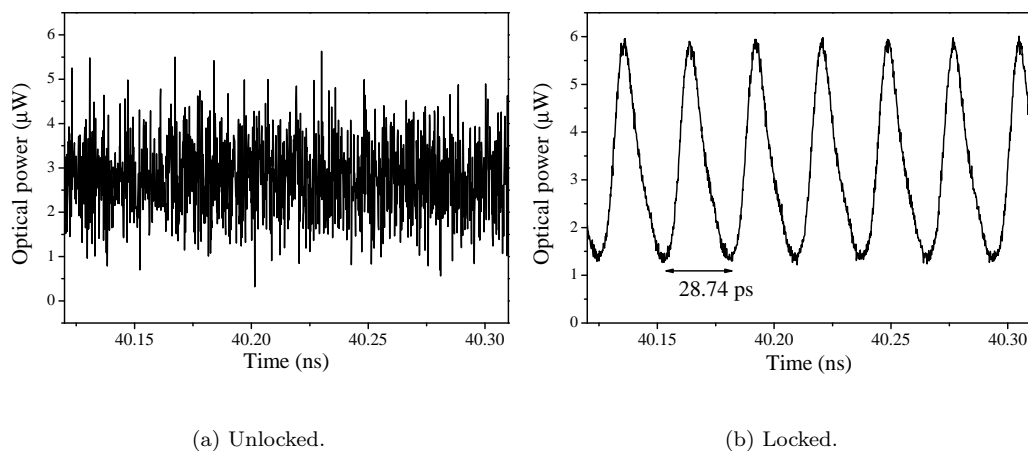


FIGURE 4.19: Optical sampling scope traces from the CCW output of the ring when (a) unlocked and (b) optically locked.

## 4.4 Chapter Summary

Measurements of optical power, optical spectra, RF spectra and intensity auto-correlation allowed for characterisation of the mode-locking parameter space and quality of the various biasing configurations of ring lasers. Several regimes of laser operation were observed, i.e. continuous wave emission, incomplete mode-locking, self pulsation, mode-locking with self pulsation and optimal mode-locking. It was found that the devices emit unidirectional whilst operating continuous wave, switching between the clockwise and counter clockwise propagating modes. However, as the rings enter the mode-locking regime, they typically begin to operate bidirectional, lasing in both directions simultaneously. The largest mode-locking regime and widest optical bandwidths ( $\sim 8$  nm) were obtained using the dual 1% absorber configuration, agreeing well with the predictions that the dual configuration yields a large mode-locking area. However, the highest RF peak powers ( $\sim 28$  dBm), narrowest RF 3 dB widths ( $\sim 0.9$  MHz) and shortest pulse widths ( $\sim 1$  ps) were obtained using the single 1% biased absorber. When the devices are operating in the optimal mode-locking regime, they emit at around 1557 nm, i.e. where there is spectral alignment of the gain and absorption curves. It is concluded that the dual configuration leads to a larger, more stable regime but the total absorber length in this case may be slightly too long. One may predict that the use of the dual SA configuration employing shorter absorbers, for example 0.5%, shall yield the best results, as it is known that the pulse width may be reduced by reducing the total absorber length. However, a balance needs to be found. Finally,

optical harmonic injection mode-locking measurements on the rings resulted in a RF 3 dB linewidth reduction from 1.4 MHz to 108 kHz, implying a vast reduction in timing jitter. This allows for synchronisation between the pulse trains from the rings and other high speed optical equipment.

# Chapter 5

## Mach-Zehnder Interferometer Results

### 5.1 Introduction

In this chapter the measurement results of the MMI couplers and then the symmetric MZI employed as a  $2 \times 2$  optical switch are discussed, highlighting the influence of the electro-optic effects based on applied current injection. Characterisation of the asymmetric MZI devices is then also reported and discussed, concluding with data from the monolithically integrated ring and AMZI.

### 5.2 Multi-Mode Interference Coupler

Fig. 5.1 shows the schematic of the MMI coupler device for splitting ratio measurements. The results of the characterisation, similar to that of the evanescent field couplers, when 10 mA is applied to each contact in turn, are shown in Table 5.1.

TABLE 5.1: Measured MMI splitting ratio results

Contact with 10 mA	Contact 1	Contact 2	Contact 3	Contact 4
Contact 1	-	-	2.571 $\mu$ A	2.571 $\mu$ A
Contact 2	-	-	2.550 $\mu$ A	2.551 $\mu$ A
Contact 3	2.535 $\mu$ A	2.550 $\mu$ A	-	-
Contact 4	2.532 $\mu$ A	2.549 $\mu$ A	-	-

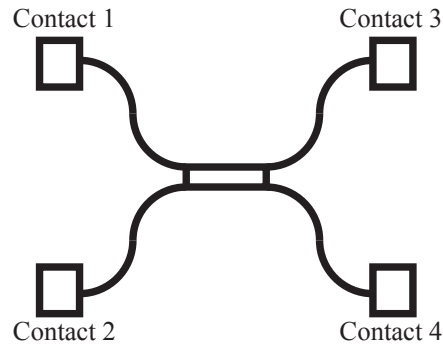


FIGURE 5.1: Schematic of an MMI coupler used for splitting ratio characterisation.

The results demonstrate a  $50 \pm 2\%$  splitting ratio, therefore the MMI couplers are deemed to be operating successfully in terms of power splitting. To assess their actual phase performance, they must be assessed within the MZI devices.

### 5.3 Symmetric Mach-Zehnder Interferometer

Here, the switching characteristics of the symmetric MZI, as shown in the SEM of Fig. 5.2, based on applied current injection are presented. The devices employ  $500 \mu\text{m}$  long phase shifting sections, with the mechanisms contributing to the refractive index change being a combination of band filling, band-gap shrinkage and free carrier absorption.

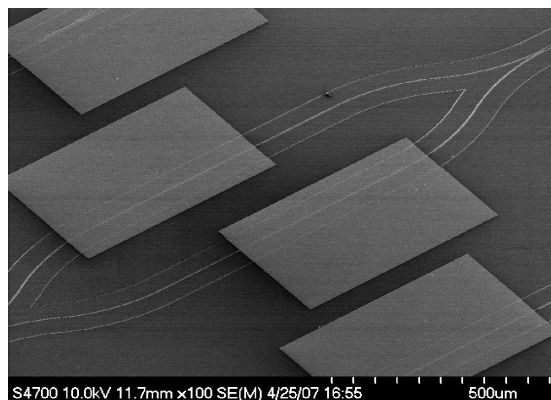


FIGURE 5.2: SEM of a fabricated MZI device.

### 5.3.1 Switching Measurements

The same free space set-up to that used previously for the waveguide loss measurements was employed for static MZI characterisation, with the exception of the inclusion of a Newport current source for carrier injection. The normalised bar and cross output signals, when a 1 mW TE polarised input wavelength of 1575 nm was injected into port 1, are depicted in Fig. 5.3. It is clear that as current is applied to the phase shifting section, the signal switches from cross to bar and vice versa with a maximum ER value of  $>20$  dB attained. A full  $\pi$  phase shift is readily achievable with an injection current of  $I_\pi=5$  mA, comparing well with other devices of this type, as reported in Table 5.2. It is also observed that as the injection current is increased, the ER value decreases due to the power level imbalance between the arms, resulting in a higher crosstalk value.

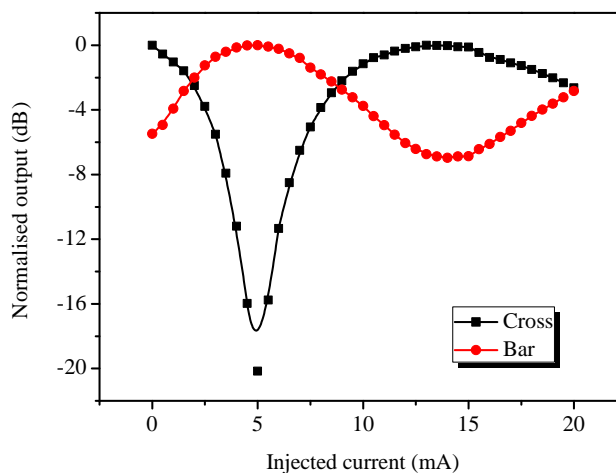


FIGURE 5.3: Measured switching characteristics of a fabricated MZI using a TE polarised input at wavelength of 1575 nm, as a function of applied current injection into one arm.

TABLE 5.2: Summary of performance of previous work on  $2 \times 2$  optical switches

Material	Device length (mm)	Extinction ratio (dB)	$I_\pi$ (mA)	Reference
GaInAsP	1	20.5	90	[172]
GaInAsP	2	$\geq 20$	4	[173]
GaInAsP	1.8	13	100	[174]
AlGaInAs MQW	3.2	21	3	[53]

Similar characterisation was performed for various wavelengths in order to assess the switching efficiency as a function of wavelength, with the results being presented in Fig. 5.4. It is observed, as expected from the electro-optic theory and results, that higher current values are required to achieve switching as the wavelength is detuned from the band-gap, as the highest change in refractive index occurs near the band-gap.

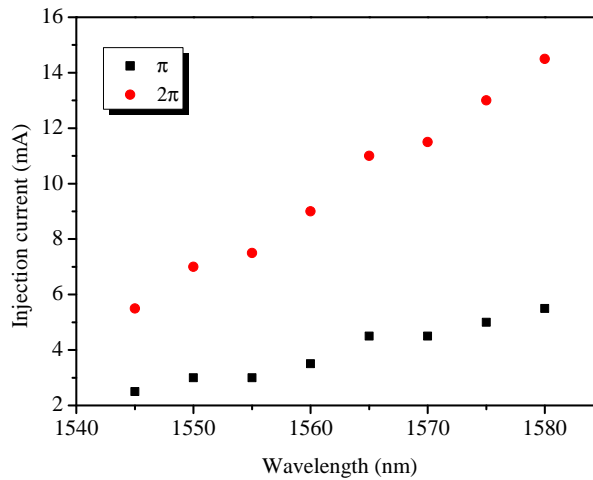


FIGURE 5.4: Switching efficiency of the MZI with applied current injection as a function of input wavelength.

The total fibre to fibre insertion loss was measured to be around 25 dB. This figure comprises passive waveguide propagation losses for both straight and bent sections, coupling losses at the device facets and direct band-gap absorption in the phase shifting sections. It is estimated that the coupling losses are of the order of 10 dB [70], thus the total chip insertion loss is around 15 dB.

## 5.4 Asymmetric Mach-Zehnder Interferometer

In the following sections, the experimental characterisation of the AMZI device employed as both a DWDM demultiplexer and an OCDMA encoder/decoder are presented.

### 5.4.1 AMZI:DWDM

Characterisation of the fabricated AMZI was performed using the same set-up as used for the symmetric MZI measurements. Fig. 5.5 details the normalised bar and cross outputs as a function of input wavelength (0 dBm, TE polarisation state) when the device is employed as a wavelength demultiplexer. A channel spacing of 0.8 nm is observed, confirming the designed  $\Delta L$  value of  $423 \mu\text{m}$  is correct. The ER may be enhanced by reducing any power imbalances in the interferometer arms by means of pre-biasing both phase shifters [54].

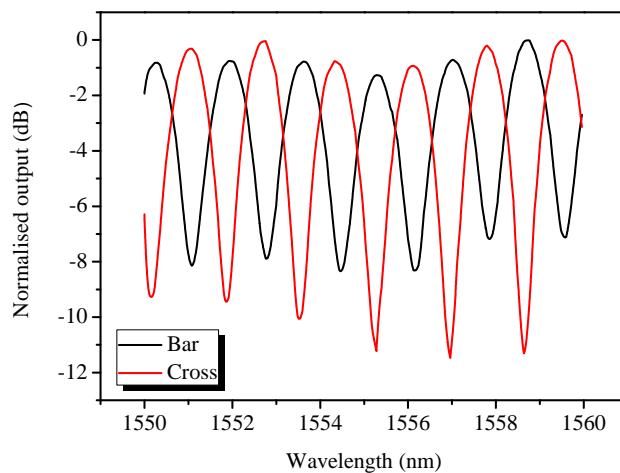


FIGURE 5.5: Measured transfer function of the fabricated AMZI as a function of TE polarised input wavelength.

Any wavelength drift in DWDM systems may lead to demultiplexing errors, thus it is desirable to have the capability to finely tune the wavelength of the demultiplexer. This is achieved here using the integrated phase shifter on the AMZI arm(s). Fig. 5.6 shows the bar output of the device when different levels of current injection are applied to the phase shifter on the lower arm. From the plot, it can be seen that the wavelength tuning is in the order of 0.1 nm/mA. Therefore to achieve a  $\pi$  phase shift one would have to apply around 8 mA, slightly higher than in the MZI case where the phase shifting sections have not been subjected to SISA.

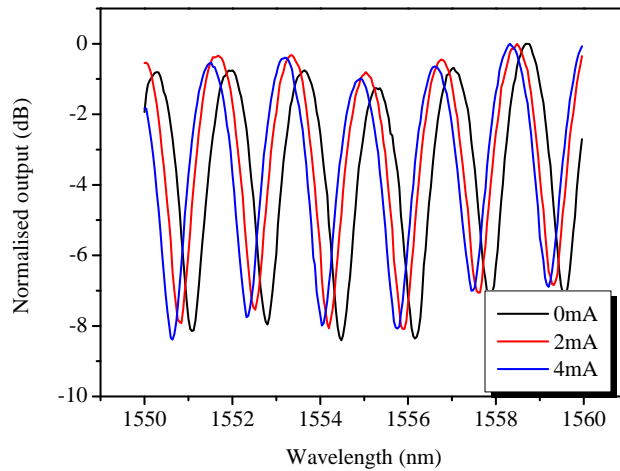


FIGURE 5.6: Measured transfer function of the bar output as a function of injection current in the lower arm.

### 5.4.2 AMZI:OCDMA

In order to demonstrate the monolithically integrated AMZIs ability to function as an OCDMA encoder/decoder, back to back devices were fabricated, as shown schematically in Fig. 5.7, such that simple 2-bit coding measurements could be performed. Here, 1.6 ps pulses from a mode-locked fibre laser were coupled into the device at port  $In_1$  at a repetition rate of 10 GHz. On these devices there was an issue with the intermixing process such that the waveguide losses were not as low as desirable leading to an unacceptable total on chip insertion loss of around 70 dB. For this reason, a dispersion compensated EDFA was used to amplify the pulses prior to entering the device, thus the operation wavelength used was 1555 nm so as to allow sufficient amplification from the gain spectrum of the EDFA.

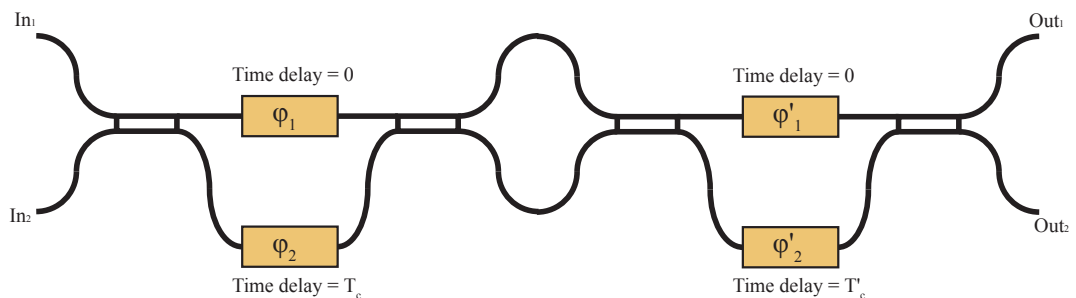


FIGURE 5.7: Schematic illustration of back to back AMZIs for simple coding experiments.

The output signal at port  $\text{Out}_1$  was amplified, filtered and then detected using a fast optical detector (nominally 65 GHz bandwidth) connected to a sampling oscilloscope. It is known that in order to decode the input signal, both the time delay and relative phase shifts of the decoder must be identical to that of the encoder. As the time delays are fixed, then one must vary the phase values in order to confirm matched and unmatched cases. The phase shifters were forward biased in order to obtain the phase combinations as detailed in Table 5.3. These combinations lead to the resultant outputs as displayed in Fig. 5.8.

TABLE 5.3: Summary of phase conditions for OCDMA experiment

Case	$\varphi_1$	$\varphi'_1$	$\varphi_2$	$\varphi'_2$
Matched 1	0	0	0	0
Matched 2	0	0	$\pi$	$\pi$
Unmatched 1	$\pi$	$\pi$	0	$\pi$
Unmatched 2	$\pi$	0	0	0

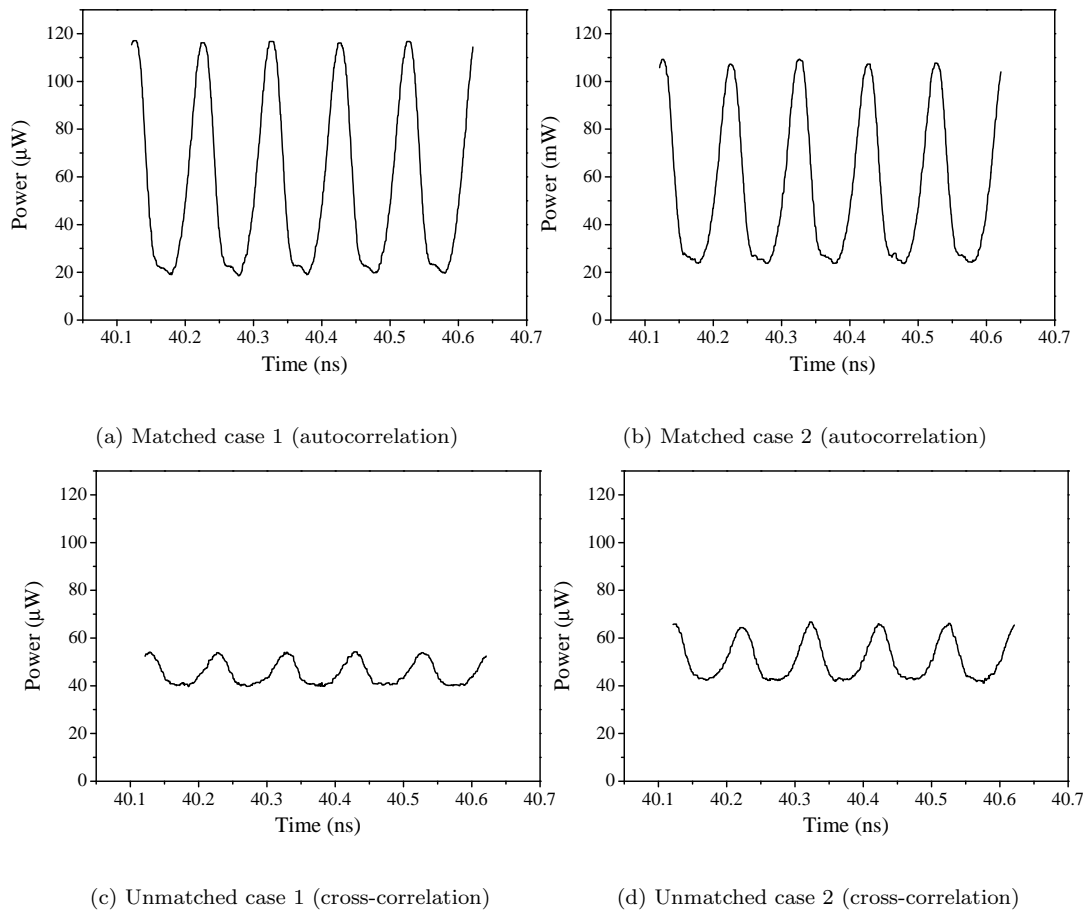


FIGURE 5.8: Output from the back to back AMZIs for a number of phase value combinations detailing both matched and unmatched cases.

Fig. 5.8 (a) and (b) show the cases for matched encoder and decoder pairs, such that the input pulse is reconstructed at the decoder output (autocorrelation). Fig. 5.8 (c) and (d) show the cases for the unmatched case where the input pulse is diminished (cross-correlation). On observation of the unmatched cases, one can see that the pulses are still evident, i.e. the ER is not optimum. This may be due to several factors, for example, the high waveguide losses and/or uneven power splitting in the MMI couplers, which could be overcome by use of tunable MMI coupler as in [175]. However, these results do demonstrate the ability to achieve simple 2-bit coding using a planar lightwave circuit.

## 5.5 Device Integration

As the ring lasers mode-lock bidirectionally, in order to optimise chip space, integrated devices were fabricated using the dual 1% SA rings as this allows two AMZI devices to be integrated with a single ring, as shown in the schematic of the back to back integrated OCDMA transmitter in Fig. 5.9.

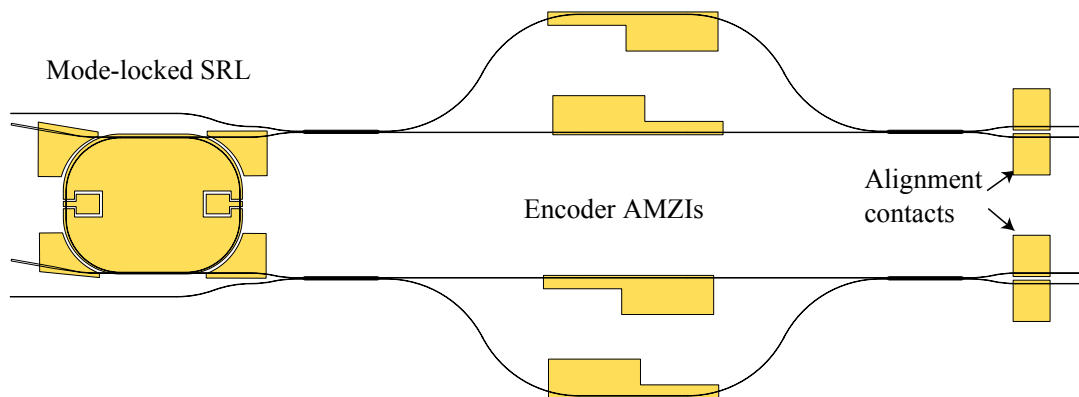


FIGURE 5.9: Schematic of integrated OCDMA transmitter.

### 5.5.1 Integrated Mode-Locked SRL and AMZI

To assess the OCDMA transmitter, chips were fabricated with single AMZIs integrated with a ring laser. The laser was biased in the optimum mode-locking regime. Fig. 5.10 shows the optical spectrum of the pulses, as measured from the

bar output of the AMZI. It is clear, as expected, that the spectrum has been superimposed with the transfer function of the AMZI, as measured in section 5.4.1, with a wavelength spacing of around 1.7 nm. This is encouraging and would imply that the pulses are being split and delayed as desired.

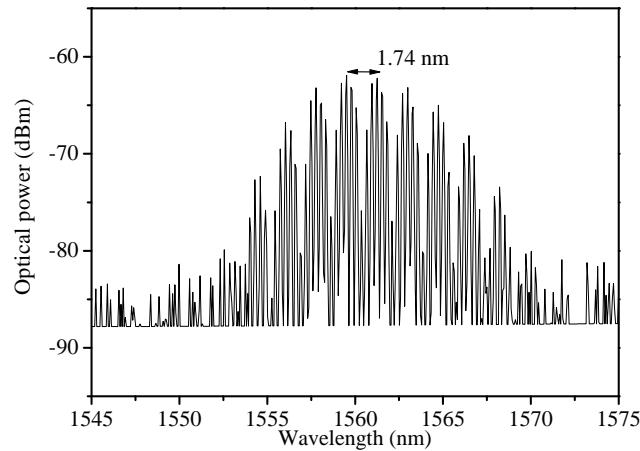


FIGURE 5.10: Optical spectrum from the bar output of the AMZI.

As the passive waveguide losses were not optimum, the output power from the integrated ring after traversing the AMZI was very low (-50 dBm). This power level, even when amplified using an EDFA, was not adequate enough for SHG autocorrelation. Therefore, a linear autocorrelation was performed on the pulses to identify if indeed the pulses were being split and delayed accordingly. It is known that the autocorrelation of a double pulse is as shown in Fig. 5.11.

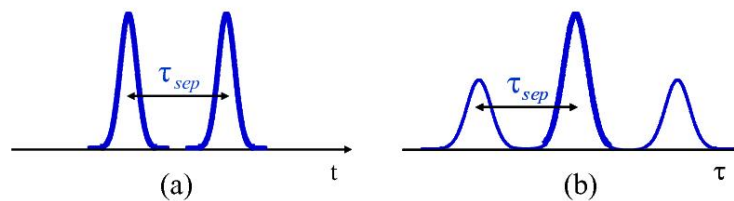


FIGURE 5.11: (a) A double pulse and (b) its autocorrelation.

As the designed time delay of the AMZI is 5 ps, this should also be reflected in the linear autocorrelation, where there should be three pulses separated by 5 ps. Fig. 5.12 shows the measured linear autocorrelation, with a smoothing of the data, where it can be seen that the pulses are indeed separated by around 5 ps, another confirmation of the correct path length difference of the AMZI device. This is a clear demonstration of the monolithic integration of two photonic devices.

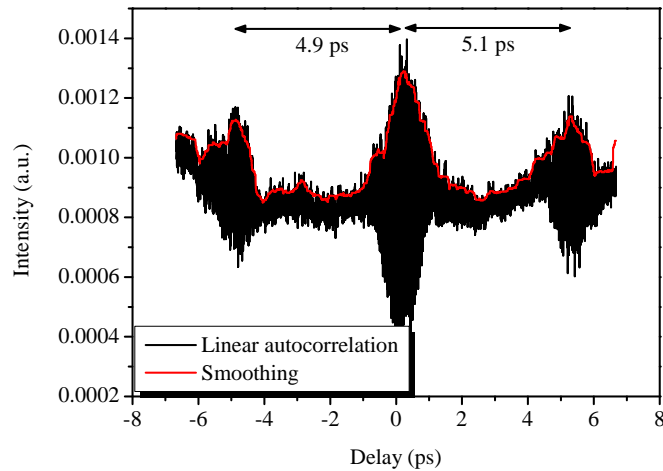


FIGURE 5.12: Measured linear autocorrelation of the double pulse, also with a smoothing of the data.

## 5.6 Chapter Summary

An overview and analysis of the measurement results obtained from the fabricated MZI devices was reported in this chapter. The experimental results of the symmetric MZI device were shown to agree well with the carrier induced electro-optic effect theory, which predicted that wavelength detuning leads to an increase in the chirp parameter, however, at the expense of phase shift efficiency. An input wavelength of 1575 nm resulted in an ER value of  $>20$  dB and a full  $\pi$  phase shift achievable with an injection current of  $I_{\pi}=5$  mA. These values are comparable with contemporary reported devices.

The AMZI was characterised as a simple DWDM demultiplexer with a 0.8 nm channel spacing and ER value of around 10 dB. Wavelength tuning of 0.1 nm/mA was also accomplished, allowing the device to be employed as a wavelength tunable switch. Back to back AMZIs were also characterised using pulses from a mode-locked fibre ring laser, successfully demonstrating some simple 2-bit OCDMA coding. On these devices there was an unresolved issue with QWI such that the passive waveguide losses were not optimum. Also, although not covered in this thesis, several other integrated devices were fabricated where the losses were suitably low, however, the lateral spreading of the intermixing was so large that any nearby ohmic contacts exhibited very high resistances ( $200\ \Omega$ ) and thus could not be assessed properly. It is believed that this lack of reproducibility was due to

insufficient process control on the sputtering machine. This is a matter that has to be addressed in the future.

Finally, the monolithic integration of a ring laser and AMZI showed that the transfer function of the AMZI was being superimposed upon the optical spectrum of the pulses. The pulse splitting and delaying was confirmed via linear autocorrelation (as the power was insufficient for SHG autocorrelation) where the pulse delay was measured to be around 5 ps, as designed. This demonstrator chip shows the potential for photonic integration that could be extended further, for example, by increasing the number of arms on the AMZI in order to increase the number of bits for coding.

# Chapter 6

## Conclusions and Future Work

### 6.1 Conclusions

In this research work, the monolithic integration of mode-locked semiconductor ring lasers and asymmetric MZIs for use in future high speed optical telecommunications systems was investigated. The devices, fabricated on the AlGaInAs multiple quantum-well material system, employed both active and passive sections realised using sputtering induced vacancy disordering QWI. Both symmetric and asymmetric path length MZIs were successfully designed, fabricated and tested in order to understand and evaluate their performance as an electro-optic switch, DWDM demultiplexer and OCDMA encoder/decoder. Mode-locked semiconductor ring lasers were fabricated and fully characterised before then being monolithically integrated along with the asymmetric MZI devices to realise highly functional photonic circuits.

The following sections summarise the major findings and results obtained throughout the course of this research work.

#### 6.1.1 Chapter 1: Introduction

The introductory chapter gave some background on the relevance of this project in terms of optical telecommunications. It briefly discussed the rise of the internet, the role of fibre optics and multiplexing techniques in order to maximise the capacity available and fulfil the ever increasing demand for bandwidth. Optical

network components, for example: light sources, waveguides and couplers, were then summarised leading on to the necessity of monolithically integrated photonic circuits and the motivation behind this research work.

### **6.1.2 Chapter 2: Material and Device Design Considerations**

The so called aluminium quaternary MQW laser material was presented here, highlighting its advantages over the traditional phosphorus quaternary, such as improved gain and temperature performance. A detailed review of the electro-optic properties in III-V QW materials was undertaken and reported, focusing mainly on the carrier induced effects most relevant to this work. The chirp parameter, a figure of merit allowing for the optimal design of electro-optic devices, was established based on minimising losses and maximising phase shift efficiency. Single lateral mode waveguides were designed for use in all devices using a commercially available mode solver package, FimmWave, where the optimum geometry was found to be a  $2\ \mu\text{m}$  wide,  $1920\ \text{nm}$  deep ridge waveguide. Assessment of the bending losses for these waveguides was also conducted using a 3-D BPM analysis, where it was found that negligible losses were incurred for a minimum bend radius of  $200\ \mu\text{m}$ . Monolithically integrated MZIs were then successfully designed comprising  $354\ \mu\text{m}$  long,  $15\ \mu\text{m}$  wide MMI couplers and  $500\ \mu\text{m}$  long active phase shifting sections, adjoined via single-mode passive waveguide interconnects. Next,  $36\ \text{GHz}$  passively mode-locked semiconductor ring lasers were designed in such a way as to allow the comparison between various absorber lengths and also single versus dual absorbers. The chapter concluded by looking at the integration of such mode-locked lasers and MZI devices to realise photonic integrated circuits.

### **6.1.3 Chapter 3: Fabrication Technology and Material Characterisation**

QWI by sputtering induced vacancy disordering was the chosen method of active/passive integration, allowing for band-gap wavelength shifts of  $>100\ \text{nm}$  to be obtained whilst maintaining active sections. Selected intermixing in selected areas was also assessed in order to partially intermix chosen sections using a single

high temperature anneal, allowing for a multiple band-gap process. Key fabrication process development was discussed, focusing mainly on dry etching, where a successful technique based on the  $\text{CH}_4/\text{H}_2/\text{O}_2$  chemistry allowed for the realisation of a dry etch stop layer for accurate and uniform control of waveguide definition. Passive waveguides were fabricated using the aforementioned methods with encouraging propagation losses ( $4.25 \text{ cm}^{-1}$  at 1550 nm TE) being achieved using the FP resonance method. Data obtained from gain guided and ridge waveguide devices fabricated on the laser material shows a threshold current density for an infinitely long device of  $J_\infty=260.5 \text{ Acm}^{-2}$ , and a characteristic temperature value of  $T_0=94 \text{ K}$ , demonstrating high quality laser material. Using the multi-section ridge waveguide laser technique, the carrier induced absorption coefficient spectra were measured. The corresponding refractive index change was then evaluated numerically using the Kramers-Kronig integral, where it was found that the results agree well with the trends observed in the literature. The chapter concluded with the development of AR coatings giving a reduction in facet reflectivity from 27.45% to 0.33%.

#### **6.1.4 Chapter 4: Mode-Locked Ring Laser Results**

Various configurations of mode-locked ring lasers were characterised in terms of optical power, optical spectra, RF spectra and SHG autocorrelation. It was found that the dual SA configuration leads to a large area of stable mode-locking, with the 1% single biased absorber giving the best performance in terms of highest RF peak power ( $\sim 28 \text{ dBm}$ ), narrowest RF 3 dB width ( $\sim 0.9 \text{ MHz}$ ) and shortest pulse width ( $\sim 1 \text{ ps}$ ). It is postulated that optimum results may be obtained by combining shorter absorbers ( $< 1\%$ ) in the dual arrangement. Optical harmonic injection mode-locking measurements on the rings resulted in a RF 3 dB linewidth reduction from 1.4 MHz to 108 kHz, implying a vast reduction in timing jitter. This allows for synchronisation between the pulse trains from the rings and other high speed optical equipment such that system level trials may be conducted.

#### **6.1.5 Chapter 5: Mach-Zehnder Interferometer Results**

Switching of the MZI device using current injection yielded an ER of  $> 20 \text{ dB}$  and a  $\pi$  phase shift current of  $I_\pi=5 \text{ mA}$ , comparable with similar reported devices. AMZI

devices were also measured, demonstrating their operation as a simple DWDM demultiplexer with a 0.8 nm (100 GHz) channel spacing. Wavelength tuning of 0.1 nm/mA was also achieved via carrier injection into one of the phase shifting sections. Back to back AMZIs allowed for the successful demonstration of simple 2-bit OCDMA encoding using pulses from a fibre mode-locked laser. Some issues were encountered, however, due to QWI, with the integrated rings and AMZIs such that passive waveguide losses were very high. Several other fabricated devices (not covered in this thesis) also suffered from lateral intermixing spreading problems such that the contacts were severely compromised. It is thought that these issues were a result of insufficient process control of the sputtering machine. Such inconsistency in the QWI process is detrimental to the realisation of highly functional integrated devices and has to be addressed. Optical spectrum measurements made on the integrated ring and single AMZI showed that the transfer function of the AMZI was being superimposed upon the mode-locking spectrum of the ring. A linear autocorrelation confirmed that the AMZI was indeed splitting and delaying the pulses by 5 ps, as designed. This demonstrates a capability for monolithic integration that could be extended further to realise more complex devices.

## 6.2 Future Work

Suggestions for future work as a follow up to this project are as follows:

- A full investigation into the detrimental effects of quantum-well intermixing. Also, how to improve the process control and thus the reproducibility of the technique.
- Investigation into other forms of active/passive integration, for example, by utilising ion implantation to form passive sections.
- Further optimisation of the mode-locked rings in terms of absorber length, position and number, as well as investigating the effect of the strength of the output coupler on the mode-locking performance.
- Theoretical modeling of mode-locking in ring lasers including a comparison with experimental results. Some initial studies are already underway in the group.

- Extending the complexity of the integrated devices, for example, by integrating a mode-locked ring with a symmetric MZI with offset phase shifters in order to realise an all optical demultiplexer.

# Bibliography

- [1] R. Raghuveer and D. Sohail, *Basics of Code Division Multiple Access (CDMA)*. Washington: SPIE Press, 2005.
- [2] G. Keiser, *Optical Fiber Communications*. Singapore: McGraw Hill, 2000.
- [3] G. P. Agrawal, *Fiber-Optic Communication Systems*. John Wiley and Sons, 1992.
- [4] R. Braunstein, “Radiative transitions in semiconductors,” *Phys. Rev.*, vol. 99, no. 6, pp. 1892–1893, Sep 1955.
- [5] R. N. Hall, G. E. Fenner, J. D. Kingsley, T. J. Soltys, and R. O. Carlson, “Coherent Light Emission From GaAs Junctions,” *Phys. Rev. Lett.*, vol. 9, no. 9, pp. 366–368, Nov 1962.
- [6] M. I. Nathan, W. P. Dumke, G. Burns, J. Frederick H. Dill, and G. Lasher, “Stimulated Emission of Radiation From GaAs p-n Junctions,” *Applied Physics Letters*, vol. 1, no. 3, pp. 62–64, 1962. [Online]. Available: <http://link.aip.org/link/?APL/1/62/1>
- [7] J. Stevenson and R. Dyott, “Optical-fibre waveguide with a single-crystal core,” *Electronics Letters*, vol. 10, no. 22, pp. 449–450, 31 1974.
- [8] [Online]. Available: <http://www.infinera.com/j7/servlet/HomePage>
- [9] R. Ramaswami and K. N. Sivarajan, *Optical Networks, A Practical Perspective*. San Fransisco: Morgan Kaufmann, 2002.
- [10] R. Tucker, G. Eisenstein, and S. Korotky, “Optical time-division multiplexing for very high bit-rate transmission,” *Lightwave Technology, Journal of*, vol. 6, no. 11, pp. 1737–1749, Nov 1988.

- [11] H. Hu, H. Mulvad, M. Galili, E. Palushani, J. Xu, A. Clausen, L. Oxenloewe, and P. Jeppesen, "Polarisation-insensitive 640 gb/s demultiplexing based on four wave mixing in a polarisation-maintaining fibre loop," *Lightwave Technology, Journal of*, vol. PP, no. 99, pp. 1–1, 2010.
- [12] O. DeLange, "Wide-band optical communication systems: Part II Frequency-division multiplexing," *Proceedings of the IEEE*, vol. 58, no. 10, pp. 1683–1690, Oct. 1970.
- [13] [Online]. Available: <http://www.alcatel-lucent.com>
- [14] D. Chen, T. Xia, G. Wellbrock, P. Mamyshev, S. Penticost, G. Grosso, A. Puc, P. Perrier, and H. Fevrier, "New Field Trial Distance Record of 3040 km on Wide Reach WDM With 10 and 40 Gb/s Transmission Including OC-768 Traffic Without Regeneration," *Lightwave Technology, Journal of*, vol. 25, no. 1, pp. 28–37, Jan. 2007.
- [15] P. Prucnal, M. Santoro, and T. Fan, "Spread spectrum fiber-optic local area network using optical processing," *Lightwave Technology, Journal of*, vol. 4, no. 5, pp. 547–554, May 1986.
- [16] A. M. Weiner, J. P. Heritage, and J. A. Salehi, "Encoding and decoding of femtosecond pulses," *Opt. Lett.*, vol. 13, no. 4, p. 300, 1988. [Online]. Available: <http://ol.osa.org/abstract.cfm?URI=ol-13-4-300>
- [17] P. R. Prucnal, *Optical Code Division Multiple Access, Fundamentals and Applications*. Boca Raton: Taylor and Francis, 2006.
- [18] R. Broeke, J. Cao, C. Ji, S.-W. Seo, Y. Du, N. Fontaine, J.-H. Baek, J. Yan, F. Soares, F. Olsson, S. Lourdudoss, A.-V. Pham, M. Shearn, A. Scherer, and S. Yoo, "Optical-CDMA in InP," *Selected Topics in Quantum Electronics, IEEE Journal of*, vol. 13, no. 5, pp. 1497–1507, Sept.-oct. 2007.
- [19] W. Huang, M. Nizam, I. Andonovic, and M. Tur, "Coherent optical CDMA (OCDMA) systems used for high-capacity optical fiber networks-system description, OTDMA comparison, and OCDMA/WDMA networking," *Lightwave Technology, Journal of*, vol. 18, no. 6, pp. 765–778, Jun 2000.
- [20] H. Sotobayashi, W. Chujo, and K. Kitayama, "Highly spectral-efficient optical code-division multiplexing transmission system," *Selected Topics in*

- Quantum Electronics, IEEE Journal of*, vol. 10, no. 2, pp. 250–258, March–April 2004.
- [21] [Online]. Available: <http://www.rp-photonics.com/>
- [22] J. J. Hsieh, J. A. Rossi, and J. P. Donnelly, “Room-temperature cw operation of GaInAsP/InP double-heterostructure diode lasers emitting at 1.1  $\mu\text{m}$ ,” *Applied Physics Letters*, vol. 28, no. 12, pp. 709–711, 1976. [Online]. Available: <http://link.aip.org/link/?APL/28/709/1>
- [23] P. Morton, T. Tanbun-Ek, R. Logan, N. Chand, K. Wecht, A. Sergent, and J. Sciortino, P.F., “Packaged 1.55  $\mu\text{m}$  DFB laser with 25 GHz modulation bandwidth,” *Electronics Letters*, vol. 30, no. 24, pp. 2044–2046, Nov 1994.
- [24] F. Delorme, S. Grosmaire, A. Gloukhian, and A. Ougazzaden, “High power operation of widely tunable 1.55  $\mu\text{m}$  distributed Bragg reflector laser,” *Electronics Letters*, vol. 33, no. 3, pp. 210–211, Jan 1997.
- [25] L. Coldren, “Monolithic tunable diode lasers,” *Selected Topics in Quantum Electronics, IEEE Journal of*, vol. 6, no. 6, pp. 988–999, Nov/Dec 2000.
- [26] S. Yu, T. F. Krauss, and P. J. R. Laybourn, “Mode locking in large monolithic semiconductor ring lasers,” *Optical Engineering*, vol. 37, no. 4, pp. 1164–1168, 1998. [Online]. Available: <http://link.aip.org/link/?JOE/37/1164/1>
- [27] D. Gloge, “Optical waveguide transmission,” *Proceedings of the IEEE*, vol. 58, no. 10, pp. 1513–1522, Oct. 1970.
- [28] E. Skogen, J. Raring, G. Morrison, C. Wang, V. Lal, M. Masanovic, and L. Coldren, “Monolithically integrated active components: a quantum-well intermixing approach,” *Selected Topics in Quantum Electronics, IEEE Journal of*, vol. 11, no. 2, pp. 343–355, March–April 2005.
- [29] D. Welch, F. Kish, S. Melle, R. Nagarajan, M. Kato, C. Joyner, J. Pleumeekers, R. Schneider, J. Back, A. Dentai, V. Dominic, P. Evans, M. Kauffman, D. Lambert, S. Hurtt, A. Mathur, M. Mitchell, M. Missey, S. Murthy, A. Nilsson, R. Salvatore, M. Van Leeuwen, J. Webjorn, M. Ziari, S. Grubb, D. Perkins, M. Reffle, and D. Mehuys, “Large-Scale InP Photonic Integrated Circuits: Enabling Efficient Scaling of Optical Transport Networks,” *Selected*

- Topics in Quantum Electronics, IEEE Journal of*, vol. 13, no. 1, pp. 22–31, Jan.-feb. 2007.
- [30] R. Nagarajan, C. Joyner, J. Schneider, R.P., J. Bostak, T. Butrie, A. Dentai, V. Dominic, P. Evans, M. Kato, M. Kauffman, D. Lambert, S. Mathis, A. Mathur, R. Miles, M. Mitchell, M. Missey, S. Murthy, A. Nilsson, F. Peters, S. Pennypacker, J. Pleumeekers, R. Salvatore, R. Schlenker, R. Taylor, H.-S. Tsai, M. Van Leeuwen, J. Webjorn, M. Ziari, D. Perkins, J. Singh, S. Grubb, M. Reffle, D. Mehuys, F. Kish, and D. Welch, “Large-scale photonic integrated circuits,” *Selected Topics in Quantum Electronics, IEEE Journal of*, vol. 11, no. 1, pp. 50–65, Jan.-Feb. 2005.
- [31] P. Bhattacharya, *Semiconductor optoelectronic devices (2nd ed.)*. Upper Saddle River, NJ, USA: Prentice-Hall, Inc., 1996.
- [32] J. F. M. Filho, “Monolithic Colliding Pulse Mode-Locked Quantum Well Lasers,” Ph.D. dissertation, Department of Electronics and Electrical Engineering—University of Glasgow, 1995.
- [33] S. M. Sze, *Modern Semiconductor Device Physics*. New York: John Wiley and Sons, 1998.
- [34] L. A. Coldren and S. W. Corzine, *Diode Lasers and Photonic Integrated Circuits*. New York: John Wiley and Sons, 1995.
- [35] S. O. Kasap, *Optoelectronics and Photonics—Principles and Practices*. New Jersey: Prentice-Hall Inc., 2001.
- [36] F. K. Reinhart, I. Hayashi, and M. B. Panish, “Mode Reflectivity and Waveguide Properties of Double-Heterostructure Injection Lasers,” *Journal of Applied Physics*, vol. 42, no. 11, pp. 4466–4479, 1971. [Online]. Available: <http://link.aip.org/link/?JAP/42/4466/1>
- [37] K. Magari, M. Okamoto, Y. Suzuki, K. Sato, Y. Noguchi, and O. Mikami, “Polarization-insensitive optical amplifier with tensile-strained-barrier MQW structure,” *Quantum Electronics, IEEE Journal of*, vol. 30, no. 3, pp. 695–702, Mar 1994.
- [38] J. Yong, J. Rorison, and I. White, “1.3  $\mu\text{m}$  quantum-well InGaAsP, AlGaInAs, and InGaAsN laser material gain: a theoretical study,” *Quantum Electronics, IEEE Journal of*, vol. 38, no. 12, pp. 1553–1564, Dec 2002.

- [39] T. Higashi, S. Sweeney, A. Phillips, A. Adams, E. O'Reilly, T. Uchida, and T. Fujii, "Observation of reduced nonradiative current in  $1.3\ \mu\text{m}$  AlGaInAs-InP strained MQW lasers," *Photonics Technology Letters, IEEE*, vol. 11, no. 4, pp. 409–411, Apr 1999.
- [40] A. Kasukawa, R. Bhat, C. Zah, S. Schwarz, D. Hwang, M. Koza, and T. Lee, "Low threshold current density  $1.5\ \mu\text{m}$  GaInAs/AlGaInAs graded-index separate-confinement-heterostructure quantum well laser diodes grown by metal organic chemical vapour deposition," *Electronics Letters*, vol. 27, no. 12, pp. 1063–1065, June 1991.
- [41] D. A. B. Miller, D. S. Chemla, T. C. Damen, A. C. Gossard, W. Wiegmann, T. H. Wood, and C. A. Burrus, "Electric field dependence of optical absorption near the band gap of quantum-well structures," *Phys. Rev. B*, vol. 32, no. 2, pp. 1043–1060, Jul 1985.
- [42] O. Mikami and H. Nakagome, "Waveguided optical switch in InGaAs/InP using free-carrier plasma dispersion," *Electronics Letters*, vol. 20, no. 6, pp. 228–229, 15 1984.
- [43] J. H. Davies, *The Physics of Low-Dimensional Semiconductor—An Introduction*. Cambridge, UK: Cambridge University Press, 1998.
- [44] K. Wakita, I. Kotaka, O. Mitomi, H. Asai, Y. Kawamura, and M. Naganuma, "High-speed InGaAlAs/InAlAs multiple quantum well optical modulators," *Lightwave Technology, Journal of*, vol. 8, no. 7, pp. 1027–1032, Jul 1990.
- [45] S. Nishimura, H. Inoue, H. Sano, and K. Ishida, "Electrooptic effects in an InGaAs/InAlAs multi quantum well structure," *Photonics Technology Letters, IEEE*, vol. 4, no. 10, pp. 1123–1126, Oct 1992.
- [46] B. O. Seraphin and N. Bottka, "Franz-Keldysh Effect of the Refractive Index in Semiconductors," *Phys. Rev.*, vol. 139, no. 2A, pp. A560–A565, Jul 1965.
- [47] M. Chan, P. Kwok, and E. Li, "The effect of carrier-induced change on the optical properties of AlGaAs-GaAs intermixed quantum wells," *Selected Topics in Quantum Electronics, IEEE Journal of*, vol. 4, no. 4, pp. 685–694, Jul/Aug 1998.

- [48] B. Bennett, R. Soref, and J. Del Alamo, "Carrier-induced change in refractive index of InP, GaAs and InGaAsP," *Quantum Electronics, IEEE Journal of*, vol. 26, no. 1, pp. 113–122, Jan 1990.
- [49] J. Zucker, T. Chang, M. Wegener, N. Sauer, K. Jones, and D. Chemla, "Large refractive index changes in tunable-electron-density InGaAs/InAlAs quantum wells," *Photonics Technology Letters, IEEE*, vol. 2, no. 1, pp. 29–31, Jan 1990.
- [50] U. Koren, T. L. Koch, B. I. Miller, and A. Shahar, "InGaAs/InGaAsP distributed feedback quantum well laser with an intracavity phase modulator," *Applied Physics Letters*, vol. 53, no. 22, pp. 2132–2134, 1988. [Online]. Available: <http://link.aip.org/link/?APL/53/2132/1>
- [51] H. Tsang and I. White, "Polarisation dependent optical modulation using the plasma effect in a GaAs-GaAlAs quantum well waveguide," *Optics Communications*, vol. 74, no. 6, pp. 365 – 369, 1990. [Online]. Available: <http://www.sciencedirect.com/science/article/B6TVF-46FR264-10W/2/48169d6415de1c346701d923e2e1a1be>
- [52] S. Fürst, S. Yu, and M. Sorel, "Fast and Digitally Wavelength-Tunable Semiconductor Ring Laser Using a Monolithically Integrated Distributed Bragg Reflector," *Photonics Technology Letters, IEEE*, vol. 20, no. 23, pp. 1926–1928, Dec.1, 2008.
- [53] H. Wong, M. Sorel, A. Bryce, J. Marsh, and J. Arnold, "Monolithically integrated InGaAs-AlGaInAs Mach-Zehnder Interferometer optical switch using quantum-well intermixing," *Photonics Technology Letters, IEEE*, vol. 17, no. 4, pp. 783–785, April 2005.
- [54] H. Wong, W. Tan, A. Bryce, J. Marsh, J. Arnold, A. Krysa, and M. Sorel, "Current injection tunable monolithically integrated InGaAs-InAlGaAs asymmetric Mach-Zehnder interferometer using quantum-well intermixing," *Photonics Technology Letters, IEEE*, vol. 17, no. 8, pp. 1677–1679, Aug. 2005.
- [55] R. Soref, J. McDaniel, D.L., and B. Bennett, "Guided-wave intensity modulators using amplitude-and-phase perturbations," *Lightwave Technology, Journal of*, vol. 6, no. 3, pp. 437–444, Mar 1988.

- [56] S. Fürst, “Monolithic Integration of Semiconductor Ring Lasers,” Ph.D. dissertation, Department of Electronics and Electrical Engineering—University of Glasgow, 2008.
- [57] M. Guden and J. Piprek, “Material parameters of quaternary III - V semiconductors for multilayer mirrors at wavelength,” *Modelling and Simulation in Materials Science and Engineering*, vol. 4, no. 4, pp. 349–357, 1996. [Online]. Available: <http://stacks.iop.org/0965-0393/4/349>
- [58] [Online]. Available: <http://www.luxpop.com/>
- [59] T. Yamamoto and M. Koshiba, “Numerical analysis of curvature loss in optical waveguides by the finite-element method,” *Lightwave Technology, Journal of*, vol. 11, no. 10, pp. 1579–1583, Oct 1993.
- [60] P. Besse, M. Bachmann, H. Melchior, L. Soldano, and M. Smit, “Optical bandwidth and fabrication tolerances of multimode interference couplers,” *Lightwave Technology, Journal of*, vol. 12, no. 6, pp. 1004–1009, Jun 1994.
- [61] O. Bryngdahl, “Image formation using self-imaging techniques,” *J. Opt. Soc. Am.*, vol. 63, no. 4, pp. 416–419, 1973. [Online]. Available: <http://www.opticsinfobase.org/abstract.cfm?URI=josa-63-4-416>
- [62] L. Soldano and E. Pennings, “Optical multi-mode interference devices based on self-imaging: principles and applications,” *Lightwave Technology, Journal of*, vol. 13, no. 4, pp. 615–627, Apr 1995.
- [63] P. Maat, “InP-Based Integrated MZI Switches for Optical Communication,” Ph.D. dissertation, Delft University of Technology, 2001.
- [64] M. Bachmann and P. A. Besse and H. Melchior, “General self-imaging properties in  $n \times n$  multimode interference couplers including phase relations,” *Appl. Opt.*, vol. 33, no. 18, pp. 3905–3911, 1994. [Online]. Available: <http://ao.osa.org/abstract.cfm?URI=ao-33-18-3905>
- [65] E. Pennings, R. van Roijen, M. van Stralen, P. de Waard, R. Koumans, and B. Verbeck, “Reflection properties of multimode interference devices,” *Photonics Technology Letters, IEEE*, vol. 6, no. 6, pp. 715–718, Jun 1994.
- [66] R. Hanfoug, L. Augustin, Y. Barbarin, J. van der Tol, E. Bente, F. Karouta, D. Rogers, S. Cole, Y. Oei, X. Leijtens, and M. Smit, “Reduced reflections

- from multimode interference couplers,” *Electronics Letters*, vol. 42, no. 8, pp. 465–466, April 2006.
- [67] Q. Lai, M. Lanker, W. Hunziker, and H. Melchior, “Tunable wavelength-selection switch and multiplexer/demultiplexer based on asymmetric silicon-on-silicon Mach-Zehnder interferometer,” *Electronics Letters*, vol. 34, no. 3, pp. 266–267, Feb 1998.
- [68] T. Durhuus, C. Joergensen, B. Mikkelsen, R. Pedersen, and K. Stubkjaer, “All optical wavelength conversion by SOA’s in a Mach-Zehnder configuration,” *Photonics Technology Letters, IEEE*, vol. 6, no. 1, pp. 53–55, Jan 1994.
- [69] Y. Chang and M. Marhic, “Fiber-optic ladder networks for inverse decoding coherent CDMA,” *Lightwave Technology, Journal of*, vol. 10, no. 12, pp. 1952–1962, Dec 1992.
- [70] H. Y. Wong, “InGaAs/InAlGaAs Monolithically Integrated Mach-Zehnder Interferometer Devices,” Ph.D. dissertation, Department of Electronics and Electrical Engineering—University of Glasgow, 2005.
- [71] T. Kinsel, “Wide-band optical communication systems: Part i time division multiplexing,” *Proceedings of the IEEE*, vol. 58, no. 10, pp. 1666–1683, Oct. 1970.
- [72] M. Chbat, B. Hong, M. Islam, C. Socolich, and P. Prucnal, “Ultrafast soliton-trapping and gate,” *Lightwave Technology, Journal of*, vol. 10, no. 12, pp. 2011–2016, Dec 1992.
- [73] N. J. Doran and D. Wood, “Nonlinear-optical loop mirror,” *Opt. Lett.*, vol. 13, no. 1, pp. 56–58, 1988. [Online]. Available: <http://ol.osa.org/abstract.cfm?URI=ol-13-1-56>
- [74] K. Blow, N. Doran, and B. Nelson, “Demonstration of the nonlinear fibre loop mirror as an ultrafast all-optical demultiplexer,” *Electronics Letters*, vol. 26, no. 14, pp. 962–964, July 1990.
- [75] J. Sokoloff, P. Prucnal, I. Glesk, and M. Kane, “A terahertz optical asymmetric demultiplexer (TOAD),” *Photonics Technology Letters, IEEE*, vol. 5, no. 7, pp. 787–790, Jul 1993.

- [76] I. Glesk, J. Sokoloff, and P. Prucnal, "Demonstration of all-optical demultiplexing of TDM data at 250 Gbit/s," *Electronics Letters*, vol. 30, no. 4, pp. 339–341, Feb 1994.
- [77] E. Jahn, N. Agrawal, M. Arbert, H.-J. Ehrke, D. Franke, R. Ludwig, W. Pieper, H. Weber, and C. Weinert, "40 Gbit/s all-optical demultiplexing using a monolithically integrated Mach-Zehnder interferometer with semiconductor laser amplifiers," *Electronics Letters*, vol. 31, no. 21, pp. 1857–1858, Oct 1995.
- [78] P. Studenkov, M. Gokhale, W. Lin, I. Glesk, P. Prucnal, and S. Forrest, "Monolithic integration of an all-optical Mach-Zehnder demultiplexer using an asymmetric twin-waveguide structure," *Photonics Technology Letters, IEEE*, vol. 13, no. 6, pp. 600–602, Jun 2001.
- [79] W. Tomlinson and C. Lin, "Optical wavelength-division multiplexer for the 1-1.4  $\mu\text{m}$  spectral region," *Electronics Letters*, vol. 14, no. 11, pp. 345–347, 25 1978.
- [80] C. Brackett, "Dense wavelength division multiplexing networks: principles and applications," *Selected Areas in Communications, IEEE Journal on*, vol. 8, no. 6, pp. 948–964, Aug 1990.
- [81] H. Uetsuka, "AWG technologies for dense WDM applications," *Selected Topics in Quantum Electronics, IEEE Journal of*, vol. 10, no. 2, pp. 393–402, March-April 2004.
- [82] N. Takato, T. Kominato, A. Sugita, K. Jinguji, H. Toba, and M. Kawachi, "Silica-based integrated optic Mach-Zehnder multi/demultiplexer family with channel spacing of 0.01-250 nm," *Selected Areas in Communications, IEEE Journal on*, vol. 8, no. 6, pp. 1120–1127, Aug 1990.
- [83] A. Shaar and P. Davies, "Prime sequences: quasi-optimal sequences for or channel code division multiplexing," *Electronics Letters*, vol. 19, no. 21, pp. 888–890, october 1983.
- [84] D. Sampson and D. Jackson, "Spread-spectrum optical fibre network based on pulsed coherent correlation," *Electronics Letters*, vol. 26, no. 19, pp. 1550–1552, Sept. 1990.

- [85] M. Marhic, "Coherent optical CDMA networks," *Lightwave Technology, Journal of*, vol. 11, no. 5, pp. 854–864, May-Jun 1993.
- [86] B. Huiszoon, L. Augustin, E. Bente, H. de Waardt, G. Khoe, M. Smit, and A. Koonen, "Integrated MachZehnder-Based Spectral Amplitude OCDMA on a Passive Optical Network," *Selected Topics in Quantum Electronics, IEEE Journal of*, vol. 13, no. 5, pp. 1487–1496, Sept.-oct. 2007.
- [87] Sotobayashi, H. and Chujo, W. and Kitayama, K., "1.6-b/s/Hz 6.4-Tb/s QPSK-OCDM/WDM (4 OCDM 40 WDM 40 Gb/s) transmission experiment using optical hard thresholding," *Photonics Technology Letters, IEEE*, vol. 14, no. 4, pp. 555–557, Apr 2002.
- [88] K. Kitayama, W. Sotobayashi, and N. Wada, "Optical Code Division Multiplexing (OCDM) and Its Applications to Photonic Networks," *IEICE Transactions on Fundamentals of Electronics, Communications and Computer Science*, vol. E82-A, no. 12, pp. 2616–2626, Dec 1999.
- [89] S. Park and A. Weiner, "Performance of asynchronous time-spreading and spectrally coded ocdma systems," *Lightwave Technology, Journal of*, vol. 26, no. 16, pp. 2873–2881, Aug.15, 2008.
- [90] K. Fouli and M. Maier, "OCDMA and Optical Coding: Principles, Applications, and Challenges [Topics in Optical Communications]," *Communications Magazine, IEEE*, vol. 45, no. 8, pp. 27–34, August 2007.
- [91] P. Vasil'ev, "High-power high-frequency picosecond pulse generation by passively Q-switched 1.55  $\mu\text{m}$  diode lasers," *Quantum Electronics, IEEE Journal of*, vol. 29, no. 6, pp. 1687–1692, Jun 1993.
- [92] P. P. Vasil'ev, "Ultrashort pulse generation in diode lasers," *Optical and Quantum Electronics*, vol. 24, no. 8, pp. 801–824, Aug 1992.
- [93] R. Kaiser and B. Huttli, "Monolithic 40-GHz Mode-Locked MQW DBR Lasers for High-Speed Optical Communication Systems," *Selected Topics in Quantum Electronics, IEEE Journal of*, vol. 13, no. 1, pp. 125–135, Jan.-feb. 2007.
- [94] L. Jiang, E. P. Ippen, and H. Yokoyama, "Semiconductor mode-locked lasers as pulse sources for high bit rate data transmission," *Journal of Optical and Fiber Communication Reports*, vol. 2, no. 1, pp. 1–31, March 2005.

- [95] P. Ho, L. A. Glasser, E. P. Ippen, and H. A. Haus, "Picosecond pulse generation with a cw GaAlAs laser diode," *Applied Physics Letters*, vol. 33, no. 3, pp. 241–242, 1978.
- [96] J. Bowers, P. Morton, A. Mar, and S. Corzine, "Actively mode-locked semiconductor lasers," *Quantum Electronics, IEEE Journal of*, vol. 25, no. 6, pp. 1426–1439, Jun 1989.
- [97] K. Williams, M. Thompson, and I. White, "Long-wavelength monolithic mode-locked diode lasers," *New Journal of Physics*, vol. 6, no. 179, 2004.
- [98] H. A. Haus, "Theory of mode locking with a fast saturable absorber," *Journal of Applied Physics*, vol. 46, no. 7, pp. 3049–3058, 1975. [Online]. Available: <http://link.aip.org/link/?JAP/46/3049/1>
- [99] H. A. Haus, "Theory of mode locking with a slow saturable absorber," *Quantum Electronics, IEEE Journal of*, vol. 11, no. 9, pp. 736–746, Sep 1975.
- [100] H. A. Haus, "Mode-locking of lasers," *Selected Topics in Quantum Electronics, IEEE Journal of*, vol. 6, no. 6, pp. 1173–1185, Nov/Dec 2000.
- [101] G. New, "Pulse evolution in mode-locked quasi-continuous lasers," *Quantum Electronics, IEEE Journal of*, vol. 10, no. 2, pp. 115–124, Feb 1974.
- [102] A. G. Vladimirov and D. Turaev, "Model for passive mode-locking in semiconductor lasers," *Phys. Rev. A*, vol. 72, no. 3, p. 033808, Sep 2005.
- [103] G. Agrawal and N. Olsson, "Self-phase modulation and spectral broadening of optical pulses in semiconductor laser amplifiers," *Quantum Electronics, IEEE Journal of*, vol. 25, no. 11, pp. 2297–2306, Nov 1989.
- [104] A. Kurobe, H. Furuyama, S. Naritsuka, N. Sugiyama, Y. Kokubun, and M. Nakamura, "Effects of well number, cavity length, and facet reflectivity on the reduction of threshold current of GaAs/AlGaAs multiquantum well lasers," *Quantum Electronics, IEEE Journal of*, vol. 24, no. 4, pp. 635–640, Apr 1988.
- [105] P. Ilroy, A. Kurobe, and Y. Uematsu, "Analysis and application of theoretical gain curves to the design of multi-quantum-well lasers," *Quantum Electronics, IEEE Journal of*, vol. 21, no. 12, pp. 1958–1963, Dec 1985.

- [106] T. Hakkarainen, E.-M. Pavelescu, K. Arstila, V. D. S. Dhaka, T. Hakulinen, R. Herda, J. Konttinen, N. Tkachenko, H. Lemmetyinen, J. Keinonen, and M. Pessa, “Optical properties of ion irradiated and annealed InGaAs/GaAs quantum wells and semiconductor saturable absorber mirrors,” *Journal of Physics D: Applied Physics*, vol. 38, no. 7, p. 985, 2005. [Online]. Available: <http://stacks.iop.org/0022-3727/38/i=7/a=004>
- [107] T. Hoshida, H.-F. Liu, M. Tsuchiya, Y. Ogawa, and T. Kamiya, “Subharmonic hybrid mode-locking of a monolithic semiconductor laser,” *Selected Topics in Quantum Electronics, IEEE Journal of*, vol. 2, no. 3, pp. 514–522, Sep 1996.
- [108] T. Ohno, H. Ishii, S. Matsuo, H. Okamoto, Y. Kawaguchi, Y. Kondo, I. Furuta, H. Ito, and Y. Yoshikuni, “Hybrid modelocking of semiconductor ring lasers incorporating passive deep-ridge waveguides,” *Electronics Letters*, vol. 38, no. 16, pp. 884–886, Aug 2002.
- [109] H. Kurita, T. Shimizu, and H. Yokoyama, “Experimental investigations of harmonic synchronization conditions and mechanisms of mode-locked laser diodes induced by optical-pulse injection,” *Selected Topics in Quantum Electronics, IEEE Journal of*, vol. 2, no. 3, pp. 508–513, Sep 1996.
- [110] J. C. Diels and W. Rudolph, *Ultrashort Laser Pulse Phenomena*. New York: Elsevier Inc., 2006.
- [111] C. Xing and E. A. Avrutin, “Multimode spectra and active mode locking potential of quantum dot lasers,” *Journal of Applied Physics*, vol. 97, no. 10, p. 104301, 2005. [Online]. Available: <http://link.aip.org/link/?JAP/97/104301/1>
- [112] R. Koumans and R. Van Roijen, “Theory for passive mode-locking in semiconductor laser structures including the effects of self-phase modulation, dispersion, and pulse collisions,” *Quantum Electronics, IEEE Journal of*, vol. 32, no. 3, pp. 478–492, Mar 1996.
- [113] M. Strain, “Integrated Chirped Bragg Gratings for Dispersion Control,” Ph.D. dissertation, Department of Electronics and Electrical Engineering—University of Glasgow, 2007.

- [114] U. Bandelow, M. Radziunas, A. Vladimirov, B. Huttel, and R. Kaiser, “40 GHz Mode-Locked Semiconductor Lasers: Theory, Simulations and Experiment,” *Optical and Quantum Electronics*, vol. 38, no. 4-6, pp. 495–512, Mar 2006.
- [115] A. S. H. Liao and S. Wang, “Semiconductor injection lasers with a circular resonator,” *Applied Physics Letters*, vol. 36, no. 10, pp. 801–803, 1980. [Online]. Available: <http://link.aip.org/link/?APL/36/801/1>
- [116] M. Sorel, P. J. R. Laybourn, G. Giuliani, and S. Donati, “Unidirectional bistability in semiconductor waveguide ring lasers,” *Applied Physics Letters*, vol. 80, no. 17, pp. 3051–3053, 2002. [Online]. Available: <http://link.aip.org/link/?APL/80/3051/1>
- [117] B. Li, M. Memon, G. Mezosi, G. Yuan, Z. Wang, M. Sorel, and S. Yu, “All-Optical Response of Semiconductor Ring Laser to Dual-Optical Injections,” *Photonics Technology Letters, IEEE*, vol. 20, no. 10, pp. 770–772, May15, 2008.
- [118] T. Krauss, R. De La Rue, and P. Laybourn, “Impact of output coupler configuration on operating characteristics of semiconductor ring lasers,” *Lightwave Technology, Journal of*, vol. 13, no. 7, pp. 1500–1507, Jul 1995.
- [119] R. van Roijen, E. C. M. Pennings, M. J. N. van Stalen, T. van Dongen, B. H. Verbeek, and J. M. M. van der Heijden, “Compact InP-based ring lasers employing multimode interference couplers and combiners,” *Applied Physics Letters*, vol. 64, no. 14, pp. 1753–1755, 1994. [Online]. Available: <http://link.aip.org/link/?APL/64/1753/1>
- [120] J. P. Hohimer and G. A. Vawter, “Passive mode locking of monolithic semiconductor ring lasers at 86 GHz,” *Applied Physics Letters*, vol. 63, no. 12, pp. 1598–1600, 1993. [Online]. Available: <http://link.aip.org/link/?APL/63/1598/1>
- [121] Y. Barbarin, E. Bente, M. Heck, J. den Besten, G. Guidi, Y. Oei, J. Binsma, and M. Smit, “Realization and modeling of a 27-GHz integrated passively mode-locked ring laser,” *Photonics Technology Letters, IEEE*, vol. 17, no. 11, pp. 2277–2279, Nov. 2005.
- [122] Y. Barbarin, E. A. J. M. Bente, M. J. R. Heck, Y. S. Oei, R. Nötzel, and M. K. Smit, “Characterization of a 15 GHz integrated

- bulk InGaAsP passively modelocked ring laser at  $1.53\mu\text{m}$ ,” *Opt. Express*, vol. 14, no. 21, pp. 9716–9727, 2006. [Online]. Available: <http://www.opticsexpress.org/abstract.cfm?URI=oe-14-21-9716>
- [123] Y. Barbarin, “ $1.55\mu\text{m}$  Integrated Modelocked Semiconductor Lasers,” Ph.D. dissertation, COBRA Research Institute–Technical University of Eindhoven, 2007.
- [124] M. Heck, M. Tahvili, S. Anantathanasarn, M. Smit, R. Notzel, and E. Bente, “Observation of dynamics in a 5 GHz passively Mode-locked InAs/InP (100) Quantum Dot Ring Laser at  $1.55\mu\text{m}$ ,” in *Lasers and Electro-Optics 2009 and the European Quantum Electronics Conference. CLEO Europe - EQEC 2009. European Conference on*, 14-19 2009, pp. 1–1.
- [125] J. Javaloyes and S. Balle, “Emission directionality of semiconductor ring lasers: A traveling-wave description,” *Quantum Electronics, IEEE Journal of*, vol. 45, no. 5, pp. 431–438, May 2009.
- [126] J. H. Marsh, “Quantum well intermixing,” *Semicond. Sci. Technol.*, vol. 8, no. 6, p. 11361155, 1993.
- [127] J. Binsma, M. van Geemert, F. Heinrichsdorff, T. van Dongen, R. Broeke, E. Bente, and M. Smit, “MOVPE Waveguide Regrowth in InGaAsP/InP with Extremely Low Butt-Joint Loss,” *IECICE Transactions in Electronics*, vol. E80-C, pp. 675–681, 1997.
- [128] M. Aoki, H. Sano, M. Suzuki, M. Takahashi, K. Uomi, and A. Takai, “Novel structure MQW electroabsorption modulator/DFB-laser integrated device fabricated by selective area MOCVD growth,” *Electronics Letters*, vol. 27, no. 23, pp. 2138–2140, Nov. 1991.
- [129] J. Barton, E. Skogen, M. Masanovic, S. Denbaars, and L. Coldren, “A widely tunable high-speed transmitter using an integrated SGDBR laser-semiconductor optical amplifier and Mach-Zehnder modulator,” *Selected Topics in Quantum Electronics, IEEE Journal of*, vol. 9, no. 5, pp. 1113–1117, Sept.-Oct. 2003.
- [130] P. Studenkov, M. Gokhale, and S. Forrest, “Efficient coupling in integrated twin-waveguide lasers using waveguide tapers,” *Photonics Technology Letters, IEEE*, vol. 11, no. 9, pp. 1096–1098, Sep 1999.

- [131] D. G. Deppe and J. N. Holonyak, "Atom diffusion and impurity-induced layer disordering in quantum well III-V semiconductor heterostructures," *Journal of Applied Physics*, vol. 64, no. 12, pp. R93–R113, 1988. [Online]. Available: <http://link.aip.org/link/?JAP/64/R93/1>
- [132] A. McKee, C. McLean, G. Lullo, A. Bryce, R. De La Rue, J. Marsh, and C. Button, "Monolithic integration in InGaAs-InGaAsP multiple-quantum-well structures using laser intermixing," *Quantum Electronics, IEEE Journal of*, vol. 33, no. 1, pp. 45–55, Jan 1997.
- [133] B. Qiu, A. Bryce, R. de la Rue, and J. Marsh, "Monolithic integration in InGaAs-InGaAsP multiquantum-well structure using laser processing," *Photonics Technology Letters, IEEE*, vol. 10, no. 6, pp. 769–771, Jun 1998.
- [134] O. P. Kowalski, C. J. Hamilton, S. D. McDougall, J. H. Marsh, A. C. Bryce, R. M. D. L. Rue, B. Vogele, C. R. Stanley, C. C. Button, and J. S. Roberts, "A universal damage induced technique for quantum well intermixing," *Applied Physics Letters*, vol. 72, no. 5, pp. 581–583, 1998. [Online]. Available: <http://link.aip.org/link/?APL/72/581/1>
- [135] X. Liu, "Quantum Well Intermixing in 1.55  $\mu\text{m}$  InGaAs/AlInGaAs and InGaAs/InGaAsP Structures and Applications," Ph.D. dissertation, Department of Electronics and Electrical Engineering—University of Glasgow, 2002.
- [136] B. Ooi, S. Ayling, A. Bryce, and J. Marsh, "Fabrication of multiple wavelength lasers in GaAs-AlGaAs structures using a one-step spatially controlled quantum-well intermixing technique," *Photonics Technology Letters, IEEE*, vol. 7, no. 9, pp. 944–946, Sep 1995.
- [137] S. M. Sze, *Semiconductor Devices—Physics and Technology*. New York, MA: John Wiley and Sons, 2002.
- [138] [Online]. Available: <http://www.vistec.eu/website/products.nsf/%28printallids%29/1EF7D0F47A49DBFDC1256A4200530E1D>
- [139] H. Namatsu, T. Yamaguchi, M. Nagase, K. Yamazaki, and K. Kurihara, "Nano-patterning of a hydrogen silsesquioxane resist with reduced linewidth fluctuations," *Microelectron. Eng.*, vol. 41-42, pp. 331–334, 1998.

- [140] G. Mezosi, M. Strain, S. Furst, Z. Wang, S. Yu, and M. Sorel, "Unidirectional Bistability in AlGaInAs Microring and Microdisk Semiconductor Lasers," *Photonics Technology Letters, IEEE*, vol. 21, no. 2, pp. 88–90, Jan.15, 2009.
- [141] R. Williams, *Modern GaAs Processing Methods*. Nirwood, MA: Artech House, 1990.
- [142] T. R. Hayes, M. A. Dreisbach, P. M. Thomas, W. C. Dautremont-Smith, and L. A. Heimbrook, "Reactive ion etching of InP using CH<sub>4</sub>/H<sub>2</sub> mixtures: Mechanisms of etching and anisotropy," *Journal of Vacuum Science and Technology B: Microelectronics and Nanometer Structures*, vol. 7, no. 5, pp. 1130–1140, 1989. [Online]. Available: <http://link.aip.org/link/?JVB/7/1130/1>
- [143] J. E. Schramm, D. I. Babic, E. L. Hu, J. E. Bowers, and J. L. Merz, "Fabrication of high-aspect-ratio InP-based vertical-cavity laser mirrors using CH<sub>4</sub>/H<sub>2</sub>/O<sub>2</sub>/Ar reactive ion etching," *Journal of Vacuum Science and Technology B: Microelectronics and Nanometer Structures*, vol. 15, no. 6, pp. 2031–2036, 1997. [Online]. Available: <http://link.aip.org/link/?JVB/15/2031/1>
- [144] K. Shinoda, K. Nakahara, and H. Uchiyama, "InGaAlAs/InP ridge-waveguide lasers fabricated by highly selective dry etching in CH<sub>4</sub>/H<sub>2</sub>/O<sub>2</sub> plasma," May 2003, pp. 550–553.
- [145] T. C. Shen, G. B. Gao, and H. Morkoc, "Recent developments in ohmic contacts for III-V compound semiconductors," vol. 10, no. 5. AVS, 1992, pp. 2113–2132. [Online]. Available: <http://link.aip.org/link/?JVB/10/2113/1>
- [146] V. Rideout, "A review of the theory and technology for ohmic contacts to group iii-v compound semiconductors," *Solid-State Electronics*, vol. 18, no. 6, pp. 541 – 550, 1975. [Online]. Available: <http://www.sciencedirect.com/science/article/B6TY5-46V5DJS-42/2/5fd3488e89a908adb35b7f889ab96822>
- [147] R. Walker, "Simple and accurate loss measurement technique for semiconductor optical waveguides," *Electronics Letters*, vol. 21, no. 13, pp. 581–583, 20 1985.

- [148] J. Pankove, "Temperature dependence of emission efficiency and lasing threshold in laser diodes," *Quantum Electronics, IEEE Journal of*, vol. 4, no. 4, pp. 119–122, Apr 1968.
- [149] J. D. Thomson, H. D. Summers, P. J. Hulyer, P. M. Smowton, and P. Blood, "Determination of single-pass optical gain and internal loss using a multisection device," *Applied Physics Letters*, vol. 75, no. 17, pp. 2527–2529, 1999. [Online]. Available: <http://link.aip.org/link/?APL/75/2527/1>
- [150] M. Rochat, M. Beck, J. Faist, and U. Oesterle, "Measurement of far-infrared waveguide loss using a multisection single-pass technique," *Applied Physics Letters*, vol. 78, no. 14, pp. 1967–1969, 2001. [Online]. Available: <http://link.aip.org/link/?APL/78/1967/1>
- [151] M. Jain and C. Ironside, "A multi-section technique for the electroabsorption measurements in waveguide semiconductor electroabsorption modulators," *IET Optoelectronics*, vol. 1, no. 4, pp. 163–168, 2007. [Online]. Available: <http://link.aip.org/link/?OPT/1/163/1>
- [152] H. K. Tsang, J. B. D. Soole, H. P. LeBlanc, R. Bhat, M. A. Koza, and I. H. White, "Efficient InGaAsP/InP multiple quantum well waveguide optical phase modulator," *Applied Physics Letters*, vol. 57, no. 22, pp. 2285–2287, 1990. [Online]. Available: <http://link.aip.org/link/?APL/57/2285/1>
- [153] C. McMahon, D. Kane, J. Toomey, and J. Lawrence, "High accuracy measurement of relaxation oscillation frequency in heavily damped quantum well lasers," *Nanoscience and Nanotechnology, 2006. ICONN '06. International Conference on*, pp. 497–500, July 2006.
- [154] T. Yamamoto, K. Sakai, S. Akiba, and Y. Suematsu, "Fast pulse behaviour of InGaAsP/InP double-heterostructure lasers emitting at 1.27  $\mu\text{m}$ ," *Electronics Letters*, vol. 13, no. 5, pp. 142–143, 3 1977.
- [155] T. Houle, J. Yong, C. Marinelli, S. Yu, J. Rorison, I. White, J. White, A. SpringThorpe, and B. Garrett, "Characterization of the temperature sensitivity of gain and recombination mechanisms in 1.3  $\mu\text{m}$  AlGaInAs MQW lasers," *Quantum Electronics, IEEE Journal of*, vol. 41, no. 2, pp. 132–139, Feb. 2005.

- [156] T. Saitoh and T. Mukai, "1.5  $\mu\text{m}$  GaInAsP traveling-wave semiconductor laser amplifier," *Quantum Electronics, IEEE Journal of*, vol. 23, no. 6, pp. 1010–1020, Jun 1987.
- [157] F. R. Pedrotti and L. S. Pedrotti, *Introduction to Optics*. New Jersey: Prentice-Hall International, 1996.
- [158] D. L. Wood and K. Nassau, "Refractive index of cubic zirconia stabilized with yttria," *Appl. Opt.*, vol. 21, no. 16, pp. 2978–2981, 1982. [Online]. Available: <http://ao.osa.org/abstract.cfm?URI=ao-21-16-2978>
- [159] J. R. DeVore, "Refractive indices of rutile and sphalerite," *J. Opt. Soc. Am.*, vol. 41, no. 6, pp. 416–417, 1951. [Online]. Available: <http://www.opticsinfobase.org/abstract.cfm?URI=josa-41-6-416>
- [160] I. H. Maltison, "Interspecimen comparison of the refractive index of fused silica," *J. Opt. Soc. Am.*, vol. 55, no. 10, pp. 1205–1208, 1965. [Online]. Available: <http://www.opticsinfobase.org/abstract.cfm?URI=josa-55-10-1205>
- [161] J. R. Andrews and R. D. Burnham, "High peak power and gateable picosecond optical pulses from a diode array traveling-wave amplifier and a mode-locked diode laser," *Applied Physics Letters*, vol. 49, no. 16, pp. 1004–1006, 1986. [Online]. Available: <http://link.aip.org/link/?APL/49/1004/1>
- [162] J. Lee, T. Tanaka, S. Uchiyama, M. Tsuchiya, and T. Kamiya, "Broadband double-layer antireflection coatings for semiconductor laser amplifiers," *Japanese Journal of Applied Physics*, vol. 36, no. Part 2, No. 1A/B, pp. L52–L54, 1997. [Online]. Available: <http://jjap.ipap.jp/link?JJAP/36/L52/>
- [163] S. H. Jeong, J. K. Kim, B. S. Kim, S. H. Shim, and B. T. Lee, "Characterization of  $\text{SiO}_2$  and  $\text{TiO}_2$  films prepared using rf magnetron sputtering and their application to anti-reflection coating," *Elsevier Journal of Vacuum*, vol. 76, 2004.
- [164] M. A. Lieberman and A. J. Lichtenberg, *Principles of plasma discharges and materials processing*. Wiley, 1994. [Online]. Available: <http://www.worldcat.org/oclc/30896011>

- [165] B. W. Hakki and T. L. Paoli, "Gain spectra in GaAs double - heterostructure injection lasers," *Journal of Applied Physics*, vol. 46, no. 3, pp. 1299–1306, 1975. [Online]. Available: <http://link.aip.org/link/?JAP/46/1299/1>
- [166] I. Kaminow, G. Eisenstein, and L. Stulz, "Measurement of the modal reflectivity of an antireflection coating on a superluminescent diode," *Quantum Electronics, IEEE Journal of*, vol. 19, no. 4, pp. 493–495, Apr 1983.
- [167] M. Sorel, G. Giuliani, A. Scire, R. Miglierina, S. Donati, and P. Laybourn, "Operating regimes of GaAs-AlGaAs semiconductor ring lasers: experiment and model," *Quantum Electronics, IEEE Journal of*, vol. 39, no. 10, pp. 1187–1195, Oct. 2003.
- [168] M. Sargent, "Theory of a multimode quasiequilibrium semiconductor laser," *Phys. Rev. A*, vol. 48, no. 1, pp. 717–726, Jul 1993.
- [169] S. Arahira and Y. Ogawa, "Repetition-frequency tuning of monolithic passively mode-locked semiconductor lasers with integrated extended cavities," *Quantum Electronics, IEEE Journal of*, vol. 33, no. 2, pp. 255–264, Feb 1997.
- [170] D. Kunimatsu, S. Arahira, Y. Kato, and Y. Ogawa, "Passively mode-locked laser diodes with bandgap-wavelength detuned saturable absorbers," *Photonics Technology Letters, IEEE*, vol. 11, no. 11, pp. 1363–1365, Nov 1999.
- [171] L. Hou, P. Stolarz, J. Javaloyes, R. Green, C. Ironside, M. Sorel, and A. Bryce, "Subpicosecond Pulse Generation at Quasi-40-GHz Using a Passively Mode-Locked AlGaInAs InP 1.55  $\mu\text{m}$  Strained Quantum-Well Laser," *Photonics Technology Letters, IEEE*, vol. 21, no. 23, pp. 1731–1733, dec.1, 2009.
- [172] K. Ishida, H. Nakamura, H. Matsumura, T. Kadoi, and H. Inoue, "InGaAsP/InP optical switches using carrier induced refractive index change," *Applied Physics Letters*, vol. 50, no. 3, pp. 141–142, 1987. [Online]. Available: <http://link.aip.org/link/?APL/50/141/1>
- [173] G. Muller, L. Stoll, G. Schulte-Roth, and U. Wolff, "Low current plasma effect optical switch on InP," *Electronics Letters*, vol. 26, no. 2, pp. 115–117, Jan. 1990.

- 
- [174] R. van Roijen, J. van der Heijden, L. Tiemeijer, P. Thijs, T. van Dongen, J. Binsma, and B. Verbeek, "Over 15 dB gain from a monolithically integrated optical switch with an amplifier," *Photonics Technology Letters, IEEE*, vol. 5, no. 5, pp. 529–531, May 1993.
- [175] J. Leuthold and C. Joyner, "Multimode interference couplers with tunable power splitting ratios," *Lightwave Technology, Journal of*, vol. 19, no. 5, pp. 700–707, May 2001.